Loughborough University

This item was submitted to Loughborough University as a PhD thesis by the author and is made available in the Institutional Repository (https://dspace.lboro.ac.uk/) under the following Creative Commons Licence conditions.

creative commons

COMMONS DEED

Attribution-NonCommercial-NoDerivs 2.5

You are free:

- to copy, distribute, display, and perform the work

Under the following conditions:

Attribution. You must attribute the work in the manner specified by the author or licensor.

Noncommercial. You may not use this work for commercial purposes.

No Derivative Works. You may not alter, transform, or build upon this work.

- For any reuse or distribution, you must make clear to others the license terms of this work.
- Any of these conditions can be waived if you get permission from the copyright holder.

Your fair use and other rights are in no way affected by the above.

This is a human-readable summary of the Legal Code (the full license).

Disclaimer

For the full text of this licence, please go to:
http://creativecommons.org/licenses/by-nc-nd/2.5/

Loughborough University

Pilkington Library

Author/Filing Title ..... GIBSON .....

.....

Vol. No. ..... Class Mark ..... T .....

Please note that fines are charged on ALL overdue items.

LOAN COPY

0402152212

Investigation of the Physical Properties of the Ternary Intermetallic Rare-Earth Compounds, RETGe (RE= Sc, Y, La - Lu; T = Ag, Au)

by

B. J. Gibson

Doctoral Thesis

Submitted in partial fulfilment of the requirements
for the award of
Doctor of Philosophy of Loughborough University

December 21, 1998

©by B. J. Gibson 1998

Loughborough University
Pil[illegible] Library
Date Nov 99
Class
Acc No. 040 215 222
M0000797LB

For my parents

Abstract

The previously unknown chemical and physical properties of the ternary rare-earth intermetallic compounds, RETGe (RE=Sc,Y,La-Lu;T=Ag,Au), are investigated using a variety of experimental techniques. The RETGe are found to crystallise in three basic different crystal structure types ($CaIn_2$-, Fe_2P-, and $CeCu_2$- type derivatives).

Magnetic ordering is observed in most RETGe compounds at low temperatures. Nearly all display anti-ferromagnetic ordering. The magnetic structures of several of the heavy RETGe compounds are determined from neutron powder diffraction studies, and are found to be temperature dependent and complex. Curie-Weiss behaviour is generally observed, with the measured magnetic moments corresponding to the RE 3+ oxidation state. Deviations in the case of SmTGe and EuAuGe may be explained in terms of crystal field excitations and the effects of mixed-valency, respectively. Examination of the magnetic ordering temperatures in conjunction with the DeGennes scaling law show little correlation, suggesting that the usual RKKY exchange interaction does not fully describe the magnetic interactions in these compounds.

Special emphasis is placed on the transport properties of the non-magnetic RETGe compounds. The electronic and lattice contributions to the specific heat capacities are calculated, and are also used in the evaluation of magnetic contributions within other compounds. The observed properties (e.g. anomalously high room temperature resistivities) are explained in terms of the calculated band structures, and suggest the classification of the RETGe as semimetals. Low temperature (^3He) susceptibility measurements of ScAgGe reveal a transition to the superconducting state at $T_C \approx 1.1K$.

CeAuGe is unusual in having a ferromagnetic ground state at low temperatures, and its magnetic properties are studied in detail by several methods, including single crystal measurements. The results are compared and contrasted with the results obtained for the isotypic compound, CeAgGe, which is observed to have an anti-ferromagnetic ground state. Inelastic neutron scattering, specific heat capacity, and single crystal susceptibility measurements all reveal the first excited energy doublet to lie around 25meV for both CeAuGe and CeAgGe. Often, Ce based compounds display heavy fermion behaviour at low temperatures, although a search for HF behaviour in CeAuGe and CeAgGe, proves inconclusive.

Contents

1 Introduction **1**

2 Sample Preparation and Characterisation **5**

2.1 High Vacuum Apparatus 5

2.2 Arc Melting Apparatus 7

2.3 Sample Preparation 7

2.3.1 CeAuGe Single Crystal 8

2.4 Sample Characterisation 9

3 Crystal Structures **10**

3.1 $CaIn_2$-type 10

3.2 Fe_2P-type 12

3.3 $CeCu_2$-type 14

4 General Magnetic Properties **18**

4.1 a.c. Susceptometer 18

4.1.1 Experimental Set-Up 18

4.1.2 Principles of Measurement 19

4.1.3 Sample Preparation and Measurement 22

4.2 Specific Heat Capacity 23

4.2.1 Experimental Description 23

4.2.2 Principles of Measurement 24

4.2.3 Sample Preparation 25
4.3 Results 25
4.3.1 High Temperature Susceptibility 25
4.3.2 Magnetic Ordering in RETGe 33
4.4 Discussion 43

5 Transport and Electronic Properties **45**
5.1 Introduction 45
5.2 Electronic Structure Calculations 46
5.2.1 Experimental 46
5.2.2 Results 48
5.3 Resistivity 53
5.3.1 Experimental 53
5.3.2 Results 55
5.4 Specific Heat Capacity 57
5.5 Magnetic Susceptibility 63
5.6 Discussion 67

6 CeAuGe and CeAgGe **69**
6.1 Introduction 69
6.2 Low Temperature Nuclear and Magnetic Structures 73
6.2.1 High Resolution Neutron Diffraction (D2B) 73
6.2.2 High Flux Neutron Diffraction (D20) 78
6.3 Critical Behaviour of the Ferromagnetic Phase Transition in CeAuGe . . . 81
6.3.1 Introduction 81
6.3.2 Experimental 82
6.3.3 Results 82
6.3.4 Discussion 89
6.4 Specific Heat Capacity 93

6.4.1 Experimental 93
6.4.2 Results 93
6.5 Inelastic Neutron Diffraction 98
6.5.1 Experimental 98
6.5.2 Results 98
6.6 CeAuGe Single Crystal Susceptibility 106
6.6.1 Experimental 106
6.6.2 Results 106
6.7 First Pressure Experiments on CeAuGe. 113
6.7.1 Experimental 113
6.7.2 Results 114
6.8 Discussion 118

7 Magnetic Structure Determination **121**
7.1 Introduction 121
7.2 Experimental 122
7.2.1 D1B Instrumentation Characteristics 122
7.2.2 D20 Instrumentation Characteristics 123
7.2.3 Sample Preparation 124
7.2.4 Experimental Setup 124
7.3 Heavy Rare-Earth Gold Germanides 125
7.3.1 Nuclear Structures 125
7.3.2 Magnetic Structures 131
7.3.3 Discussion 139
7.4 Heavy Rare-Earth Silver Germanides 140
7.4.1 Nuclear Structures 140
7.4.2 Magnetic Structures 144
7.4.3 Discussion 146

8 Summary and Conclusions **148**

A Crystallographic Data **154**

A.1 HoAuGe 154

A.2 DyAgGe 155

B Superconductivity in ScAgGe **159**

C Representation Analysis **161**

List of Figures

2.1 Schematic diagram of the high vacuum apparatus. 6
2.2 Schematic diagram of the arc melting apparatus. 7
2.3 Photograph of CeAuGe single crystals under a light microscope. 9

3.1 Crystal structure of CeAuGe. 11
3.2 Crystal structure of DyAgGe. 14
3.3 Unit cell volume as a function of rare-earth atom for REAuGe and REAgGe. 16
3.4 Crystal structures of EuAuGe and EuAgGe. 16

4.1 Schematic diagram of the a.c. susceptometer. 20
4.2 Schematic diagram of the specific heat capacity calorimeter. 24
4.3 Inverse d.c. susceptibilities of selected REAuGe compounds. 30
4.4 Inverse d.c. susceptibilities of selected REAgGe compounds. 31
4.5 Inverse d.c. susceptibilities of SmAuGe and SmAgGe. 32
4.6 DeGennes plots of the REAuGe and REAgGe compounds. 32
4.7 Magnetic susceptibilities of the heavy REAuGe compounds. 34
4.8 Magnetic susceptibilities of the heavy REAgGe compounds. 34
4.9 Magnetic susceptibility of HoAuGe. 37
4.10 Specific heat capacity of HoAuGe. 37
4.11 Magnetic susceptibility of ErAuGe. 39
4.12 Specific heat capacity of ErAuGe. 39
4.13 Magnetic susceptibility of DyAgGe. 41

4.14 Hysteresis curve of DyAgGe. 41
4.15 Specific heat capacity of DyAgGe. 42

5.1 Self consistent energy band structures of ScAuGe, YAuGe, LaAuGe, and LuAuGe. 49
5.2 Self consistent total DOS of ScAuGe, YAuGe, LaAuGe, and LuAuGe. . . . 50
5.3 Self consistent energy band structures of ScAgGe, YAgGe, LaAgGe, and LuAgGe. 51
5.4 Self consistent total DOS of ScAgGe, YAgGe, LaAgGe, and LuAgGe. . . . 52
5.5 Four point contact arrangement used for the resistivity measurements. . . . 54
5.6 Electrical resistivities of the non-magnetic REAuGe and REAgGe compounds. 56
5.7 Specific heat capacities of the non-magnetic REAuGe compounds. 58
5.8 Specific heat capacities of the non-magnetic REAgGe compounds. 58
5.9 Equivalent Debye temperatures of the four non-magnetic REAuGe compounds. 61
5.10 Equivalent Debye temperatures of the four non-magnetic REAgGe compounds. 61
5.11 Magnetic susceptibilities of the non-magnetic REAuGe compounds. 64
5.12 Magnetic susceptibilities of the non-magnetic REAgGe compounds. 64

6.1 Molar susceptibilities of CeAuGe and CeAgGe. 70
6.2 Neutron diffraction patterns of CeAuGe and CeAgGe. 75
6.3 Neutron diffraction difference pattern of CeAuGe. 77
6.4 Neutron diffraction patterns of CeAgGe. 79
6.5 Polarisation curves of CeAuGe. 84
6.6 Modified Arrott plot for isotherms of CeAuGe in the critical regime. 84
6.7 Temperature dependence of the spontaneous polarisation, J_S, and the inverse zero field susceptibility of CeAuGe. 85
6.8 Kouvel-Fisher plots for β and γ. 87
6.9 Plot of $ln(J)$ versus $ln(\mu_0 H)$ at several temperatures around the critical point of CeAuGe. 88
6.10 Scaling plot of CeAuGe. 88

6.11 Temperature dependence of the Kouvel Fisher exponent of CeAuGe. 92
6.12 Specific heat capacity of CeAuGe and CeAgGe. 95
6.13 Magnetic entropy of CeAuGe and CeAgGe. 97
6.14 Energy transfer spectrums of CeAuGe and CeAgGe. 99
6.15 Magnified energy transfer spectrum of CeAuGe and CeAgGe. 102
6.16 Instrumental resolution function of the triple-axis spectrometer, IN3. . . . 103
6.17 Possible energy level schemes of CeAuGe and CeAgGe. 104
6.18 Single crystal magnetic susceptibility of CeAuGe. 107
6.19 Single crystal magnetisation curves of CeAuGe. 108
6.20 Inverse magnetic susceptibility of single crystal CeAuGe fitted to the CEF parameters. 112
6.21 Unit cell parameters of CeAuGe as a function of pressure. 114
6.22 Magnetic susceptibility of CeAuGe under elevated pressures. 116
6.23 Curie temperature of CeAuGe as a function of temperature. 116

7.1 Schematic layout of the neutron diffractometer, D1B. 123
7.2 Vanadium sample holders used for neutron powder diffraction. 125
7.3 Neutron powder diffraction patterns of TbAuGe taken at 15K and 1.5K. . 126
7.4 Neutron powder diffraction patterns of DyAuGe taken at 20K and 1.5K. . 127
7.5 Neutron powder diffraction patterns of HoAuGe taken at 50K and 1.5K. . 128
7.6 Neutron powder diffraction patterns of ErAuGe taken at 15K and 1.5K. . . 129
7.7 Magnetic structure of HoAuGe at $T = 1.5$K. 133
7.8 Schematic representation of the incommensurate magnetic structure found in the REAuGe compounds. 138
7.9 Neutron powder diffraction patterns of HoAuGe taken at several temperatures. 139
7.10 Neutron powder diffraction patterns of DyAgGe taken at 30K and 1.5K. . 142
7.11 Neutron powder diffraction patterns of HoAgGe taken at 20K and 1.5K. . 143
7.12 Magnetic structure of DyAgGe. 147

A.1 Guinier diffraction patterns of HoAuGe. 154

A.2 Guinier diffraction patterns of DyAgGe. 155

B.1 Low temperature magnetic susceptibility of ScAgGe. 160

List of Tables

3.1 Lattice constants of the REAuGe and REAgGe compounds crystallising in the ordered $CaIn_2$-type structure. 13

3.2 Lattice constants of the REAgGe compounds crystallising in the ordered Fe_2P-type structure. 15

4.1 Magnetic data for the S=1/2 REAuGe and REAgGe compounds. 29

5.1 Technical data concerning the band structure calculations of the REAgGe compounds. 47

5.2 Resistivities of the non-magnetic RETGe compounds. 55

5.3 Phonon properties of the non-magnetic REAuGe and REAgGe compounds. 63

5.4 Electronic data of the non-magnetic REAuGe and REAgGe compounds. . 65

6.1 Magnetic data for CeAuGe and CeAgGe. 71

6.2 Neutron refinement results for CeAuGe and CeAgGe. 76

6.3 Critical exponents for CeAuGe as derived from both the different experimental methods and theoretical models. 90

6.4 Measured and calculated critical amplitudes of CeAuGe. 91

6.5 Values for the critical temperature, T_C, of CeAuGe. 92

6.6 Peak profile data of the fits to the inelastic neutron scattering data for CeAuGe and CeAgGe. 101

6.7 Results of the CEF susceptibility fits of CeAuGe. 111

7.1 Lattice constants and atomic coordinates of TbAuGe, DyAuGe, HoAuGe, and ErAuGe. 130
7.2 Results of the magnetic Rietveld refinements of TbAuGe, DyAuGe, HoAuGe, and ErAuGe at $T = 1.5$K. 136
7.3 Results of the magnetic Rietveld refinements of HoAuGe at T=2.9K and 4.9K. 140
7.4 Lattice constants and atomic coordinates of DyAgGe and HoAgGe. 141
7.5 Results of the magnetic structure refinements of DyAgGe and HoAgGe. . . 146

A.1 Crystal data and structure refinement details for HoAuGe and DyAgGe. . 156
A.2 Atomic co-ordinates of HoAuGe. 157
A.3 Interatomic distances and positional parameters of HoAuGe. 157
A.4 Atomic co-ordinates of DyAgGe. 158
A.5 Interatomic distances and positional parameters of DyAgGe. 158

C.1 Character table of the irreducible representations of G_k. 163
C.2 Transformation properties of the spin components of HoAuGe. 164

Chapter 1

Introduction

Intermetallic compounds containing rare-earth elements have been the focus of considerable research ever since the advent of improved techniques in the separation of rare-earth elements. The interest in these compounds arises, firstly, from the increased availability of sufficient quantities of high purity metallic elements, and, more importantly, from the vast array of intriguing physical properties that have been observed in the pure rare-earth metals and their compounds. Apart from the great technological importance of magnetically ordered compounds in applications ranging from hard ferromagnetic materials (e.g. $SmCo_5$ or the more recent Nd-Fe-B phases [1]), to the thin film devices based on RE-transition metal films and multilayers used in recording media, such varied effects as Kondo behaviour, valence fluctuations, heavy fermion behaviour, and superconductivity have been recently discovered. Most of this uncommon behaviour is found to occur predominately in the Ce and Yb intermetallic compounds due to their more unstable nearly empty ($4f^1$), or nearly full ($4f^{13}$), configurations of the $4f$ electron shell.

Much of the current focus of the experimental and theoretical investigations of rare-earth intermetallic compounds involves the magnetic behaviour due to the partially filled $4f$-shell of the rare-earth atom. In most cases the $4f$-electrons are observed to be well localised on the rare-earth atomic sites, which generally gives rise to long range magnetic ordering at low temperatures. In the vast majority of compounds antiferromagnetic ordering is ob-

served, or, less frequently, ferromagnetic ordering. This long range magnetic ordering is phenomenologically well described by the RKKY exchange interaction [2] in which the magnetic coupling between localised magnetic moments is mediated via the polarisation of conduction electrons. Because the 4*f*-electrons do not participate significantly in bonding, the crystal structures are usually the same for all the compounds in a given series of rare-earth intermetallic compounds. This, for example, can facilitate the systematic study of the magnetic properties of different rare-earths under similar crystal electric field (CEF) conditions. The CEF, that is, the electric charges surrounding the rare-earth ion in general lift the degeneracy of the Hund's rule RE groundstate. The splitting of the $2J+1$ degeneracy depends on the magnitude of the electric charges and on the symmetry of their arrangement around the rare-earth ion and in general has to be determined experimentally. The degeneracies allowed from the symmetry can be determined from theoretical considerations [3]. Reviews of the more recently investigated magnetic and electrical properties of the rare-earth intermetallic compounds can be found, for example, in the articles of Grewe and Steglich [4], or of Szytuła and Leciejewicz [5].

In the case of intermetallic compounds containing either Ce or Yb there is a tendency towards the more stable empty or full *f*-shell configuration of La or Lu, respectively. This can induce a strong hybridisation of the *f*-electrons with the conduction electrons leading, e.g. to an enhanced electron effective mass, and an increase of the density of states (DOS) at the Fermi surface (E_F). As a consequence, heavy fermion behaviour, conceivably connected to superconductivity, as was first observed in $CeCu_2Si_2$, [6] or Kondo insulating behaviour, as for example in CeNiSn [7] are occasionally observed. Much of the current research in rare-earth intermetallics is directed towards an understanding of these or related phenomena.

Until recently, the majority of the research has been performed on binary compounds. The expansion of this area to ternary or even quarternary compounds, especially within the last decade, has added another dimension to this field of study. Firstly, the addition of a third (or fourth) element increases the number of crystal structure types formed. In addition, there are now many more compounds crystallising in the same crystal structure

type, whose differing magnetic properties may be contrasted.

One interesting subgroup of the ternary intermetallics contains those compounds having a simple 1:1:1 composition with the general formula RETX, with RE being a rare-earth element (Sc, Y, La-Lu), T a late transition element, and X an element of the *p*-block. Currently well over 1000 intermetallic compounds with the simple 1:1:1 composition are known [8], and which have been observed to crystallise in over 30 different structure types. Crystallographic details of many of these compounds may be found, for example, in the review article by Fornasini and Merlo [9].

In this thesis, the general structural and physical properties of the two series of compounds, REAuGe and REAgGe, are investigated. Preliminary investigations of these compounds have been previously reported in the literature. In particular, the lattice constants of selected compounds, determined from X-Ray powder diffraction results, were first published by Zanicchi et al. in 1983 [10] and Rossi et al. in 1992 [11], and some of the magnetic properties of CeAgGe were reported by Pecharsky et al. in 1991 [12], in which antiferromagnetic ordering at $T_N = 5$K was conjectured. More recently, investigations of these compounds undertaken by Pöttgen and co-workers at the Max-Planck-Institut für Festkörperforschung in Stuttgart have attempted to gain a more complete understanding of the chemical and crystallographic properties of these compounds. These have provided new information about the crystallographic structures of several new phases [13, 14], as well as the basic magnetic properties of CeAuGe [15] which show it to order ferromagnetically at $T_C \approx 10$K. In the course of this work a first investigation of the magnetic and transport properties of the non-magnetic REAuGe (RE=Sc,Y,La,Lu) has been published [16].

The current work is stimulated from the desire to understand more fully these findings, especially the contrasting magnetic behaviour in the isostructural CeAuGe and CeAgGe compounds, and the unusual, almost semi-metallic properties of the REAuGe compounds. In addition, the structural and magnetic properties of the remaining compounds in the series are systematically examined in order to search for new magnetic properties.

This thesis is arranged as follows, with the experimental techniques and theoretical ideas being presented as they arise:

- The methods of sample preparation, including a description of the apparatus are described in chapter 2. The preparation of the CeAuGe single crystals and sample characterisation are also discussed.

- The three different crystallographic structure types in which the REAuGe and REAgGe form are compared and contrasted in chapter 3.

- The basic magnetic properties of the REAuGe and REAgGe germanides, as determined from susceptibility measurements, are examined in chapter 4.

- In chapter 5, the results of band structure calculations, resistivity, magnetic susceptibility, and specific heat capacity measurements performed on the non-magnetic RETGe compounds are discussed.

- The contrasting magnetic properties of the two compounds CeAuGe and CeAgGe are investigated in chapter 6 by means of powder elastic neutron diffraction, inelastic neutron diffraction, critical field analysis, specific heat capacity, and anisotropic magnetic susceptibility measurements.

- The magnetic structures of selected RETGe compounds, as determined by powder neutron diffraction, are examined in chapter 7. These results are discussed in connection with the previous susceptibility and specific heat capacity results.

- Conclusions drawn from this work are presented in chapter 8.

Three appendices are attached. Appendix A lists the full crystallographic information for HoAuGe and DyAgGe, as determined from single crystal X-Ray diffraction. Appendix B details the discovery of superconductivity found in ScAgGe at low temperatures. Finally, Appendix C contains details of the representation analysis method which is useful for the evaluation of the magnetic structures in chapters 6 and 7.

Chapter 2

Sample Preparation and Characterisation

In the first part of this chapter the methods and equipment used for the preparation of the RETX compounds are discussed, including a description of the high vacuum and arc melting apparatus. The second section proceeds to describe the methods of preparation required for the various compounds. The different methods of X-Ray diffraction used to characterise the samples are also mentioned.

2.1 High Vacuum Apparatus

Due to the air and moisture sensitivity of the rare earth metals, and the conditions necessary for the preparation of pure samples, a high vacuum in conjunction with an argon atmosphere is used to handle the starting materials. The vacuum apparatus is shown in fig. 2.1, and is composed of two connected glass tubes, which may be separated from each other and from the auxiliary outlets(2) by a series of valves(1). The lower tube may be connected to either the primary pump(6) or an argon source(10). When pumped by the primary, a pressure of approx. 10^{-3}mbar is reached. The high vacuum is realised within the upper tube, which can be evacuated by a mercury diffusion pump(7), and liquid nitrogen

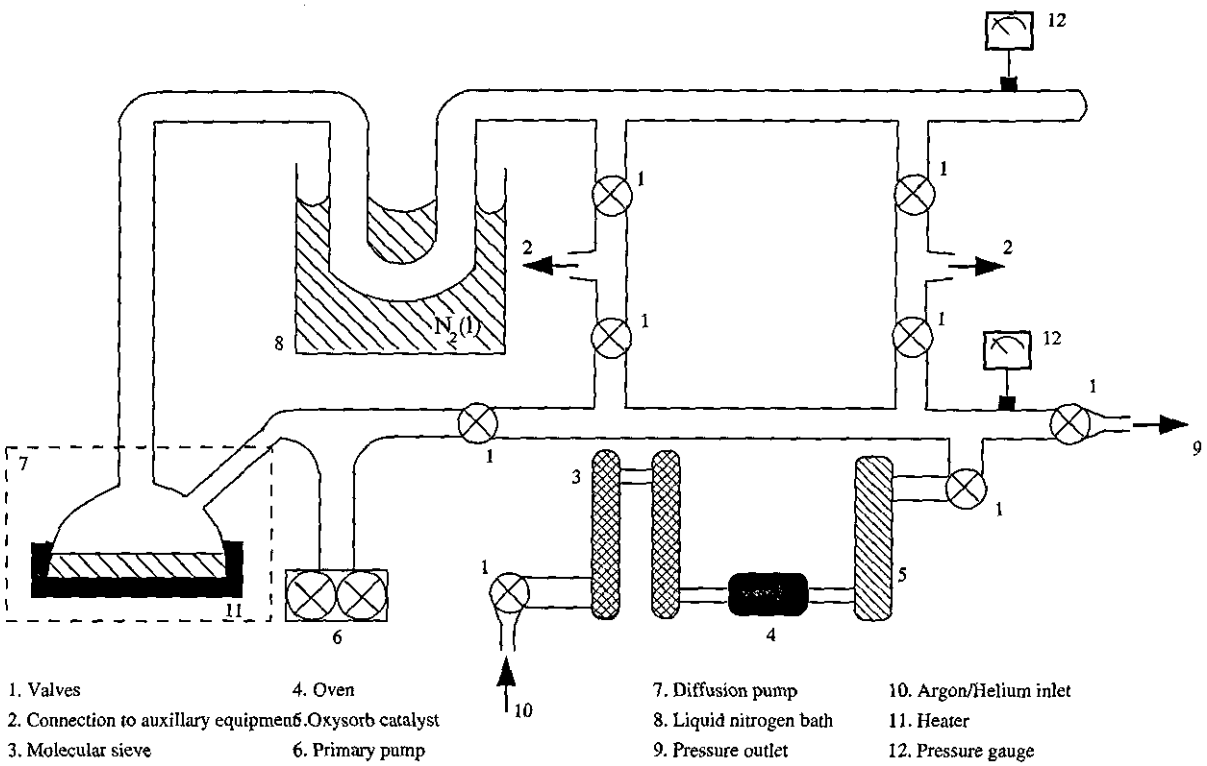

Figure 2.1: Schematic diagram of the high vacuum apparatus.

trap(8), to a pressure of less than 10^{-6}mbar. The pressure in the upper tube is measured by an ionivac gauge, and by a thermovac gauge in the lower tube(12).

Purified argon (99.996%, Messer-Griesheim) is used as an inert atmosphere. There are three stages to the drying process which removes any traces of water, oxygen, or nitrogen. Firstly, the argon is passed over a molecular sieve(3), pore size 300-500pm, which absorbs any remaining moisture. Oxygen and nitrogen are then removed by a titanium sponge(4) heated at 700°C. In a final stage any remaining water or oxygen is removed by a Cr^{3+} oxisorb [18] catalyst(5).

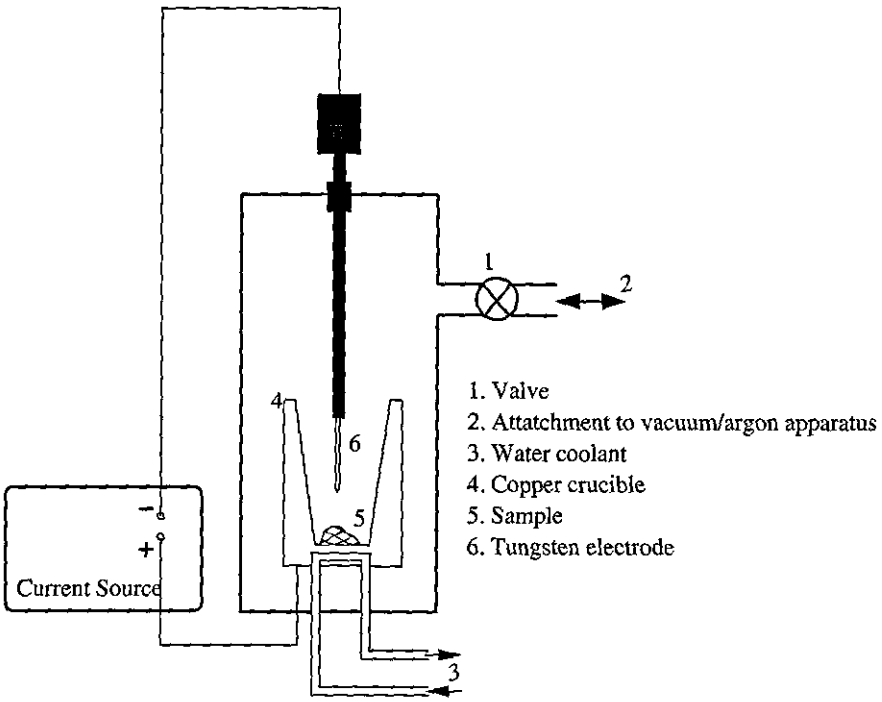

Figure 2.2: Schematic diagram of the arc melting apparatus.

2.2 Arc Melting Apparatus

The arc melting apparatus is shown in fig. 2.2, and is connected to one of the auxiliary outputs of the high vacuum apparatus via the outlet valve(1). The reactants are placed in the copper crucible(4) and the sample space flushed several times with argon to remove any water and oxygen. The reactants are melted together by an electron arc supplied by an E.S.S. 130 TG high current source, and generated between the movable tungsten cathode(6) and the copper crucible acting as the anode(4). A current of 20 - 40 A is necessary for congruent melting.

2.3 Sample Preparation

The ternary intermetallic compounds, RETGe, with the exception of YbAuGe and YbAgGe, are prepared using the arc melting apparatus previously described. Starting materials are dendritic lumps of the rare-earth metals (Johnson Matthey), silver and gold wire (De-

gussa, diam. 2mm), and germanium lumps (5N, Wacker), all with stated purities better than 99.9%. In the first reaction step, small pieces of the dendritic rare-earth metal lumps (approx. 500mg) are melted under a reduced purified argon atmosphere (800mbar) in the arc melting furnace (fig. 2.2). In the second step the silver/gold wire and germanium lumps are reacted together with the rare-earth element in the ideal atomic ratio according to the equation

$$m(T) = \frac{m(RE)}{M(RE)} * M(T) \tag{2.1}$$

where m is the mass of the element(RE-rare-earth, T-gold, silver, germanium), and M is the molar mass of the particular element. The resulting buttons are turned over and remelted three times on each side to ensure homogeneity. The weight losses after several meltings are usually less than 1%. The samples are subsequently sealed in evacuated silica tubes and annealed for several days at 800°C and 970°C for REAuGe and REAgGe, respectively. In the case of YbAuGe and YbAgGe preparation by arc melting is not possible due to the high vapour pressure of Yb. The elements are instead sealed under a high vacuum within tantalum tubes in the ideal atomic ratio according to eqn. 2.1. They are then heated at approx. 1500°C for a period of about 10 days.

2.3.1 CeAuGe Single Crystal

In addition to the polycrystalline samples previously described, several single crystals of CeAuGe, having suitable dimensions for magnetisation measurements and neutron diffraction, have been grown. The crystals are all prepared using the Czochralski method [19] by M. Jankowicz at the Kristall- und Materialentwicklungslabor at Frankfurt University. The two needle shaped crystals shown in figure 2.3 are cut with the needle axis along the a- and c- directions, respectively. The crystals have dimensions of approximately 8mm x 2mm x 2 mm, and mass, $m \approx 60$mg. An in depth description of the preparation and characterisation of the CeAuGe single crystal is provided in the work by M. Jankowicz [20].

Figure 2.3: Photograph of two CeAuGe single crystals under a light microscope. Crystals are cut with the needle axis corresponding to the a-axis (left), and to the c-axis (right).

2.4 Sample Characterisation

The samples are characterised after arc melting and also after the annealing process by taking X-Ray powder patterns (modified Guinier technique [21]), with Cu $K\alpha_1$ radiation and 5N silicon (a = 543.07pm) as internal standard. The indexing of the reflections is assured by intensity calculations [22] using the positional parameters of the refined structures. The lattice constants are obtained using least squares refinements of the Guinier powder data. In all cases these are seen to be in good agreement with previously reported data [10, 11, 12].

In addition, small needle shaped crystals have been isolated for several of the compounds, which have been subsequently analysed by single crystal X-Ray diffraction. A four-circle diffractometer (CAD4) using graphite monochromatized Ag Kα or Mo $K\alpha_1$ radiation and a scintillation counter with pulse height discrimination is used in all cases. Details of the instrumentation characteristics are given in appendix A. The samples are seen to be light grey in colour, stable in air, and are quite brittle.

Chapter 3

Crystal Structures

The rare-earth gold and silver germanides crystallise as ternary ordered derivatives of three distinct structures; $CaIn_2$- , Fe_2P- , and $CeCu_2$-type derivatives. These are examined in this chapter.

3.1 $CaIn_2$-type

All the REAuGe compounds, and also LaAgGe, CeAgGe, and the unannealed preparations of PrAgGe and NdAgGe, crystallise as ternary ordered variants of the hexagonal $CaIn_2$-type structure. Several of these compounds have been previously prepared by Rossi et al.[11], and Pecharsky et al.[12], in which they determined the lattice constants from X-Ray powder diffraction. These are compared in table 3.1 with the lattice constants recently determined from single crystal X-Ray diffraction [13, 16, 23].

The crystal structures are well described with the RE atoms occupying the calcium positions of the $CaIn_2$ structure in which they form trigonal prisms. The gold(silver) and germanium atoms occupy the indium positions in an ordered manner, forming puckered hexagonal sheets. Consecutive layers are rotated by 60° around the c-axis with respect to each other. This produces a stacking sequence along [0 0 1] of $ABAC$, with the RE atom layers denoted by A and the two Au(Ag)Ge layers with B and C. This is displayed in figure

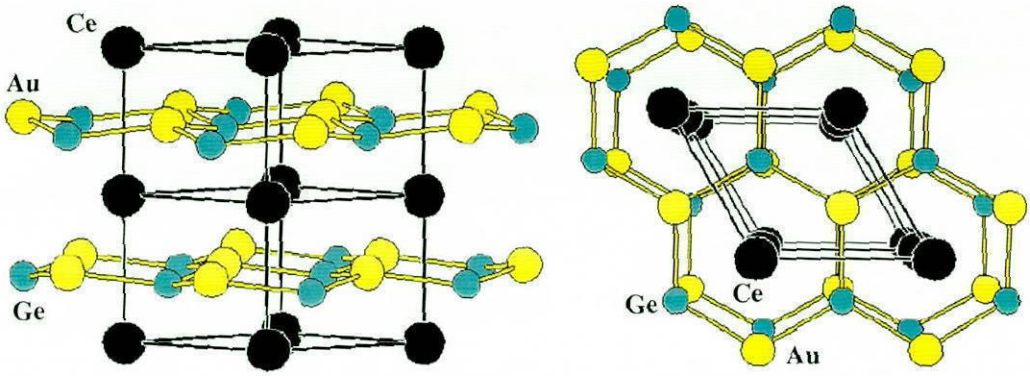

Figure 3.1: (left) Crystal structure of CeAuGe. (right) Perspective view of CeAuGe along [0 0 1]. Large black circles denote Ce atoms, yellow and blue circles denote Au and Ge atoms, respectively.

3.1(a).

From X-Ray powder diffraction there is a question of the distribution of the Au(Ag) and Ge atoms on the indium sites, as both a disordered and ordered arrangement are consistent with the composition, allowing the crystal symmetry to be determined using the space groups $P6_3/mmc$ (no. 194) or $P6_3mc$ (no. 186). Only the lower symmetry space group, $P6_3mc$, allows an ordered arrangement of the Au(Ag)Ge polyanions. This group is found to be correct from a consideration of the structure refinements based on single crystal X-Ray data. The crystallographic data for HoAuGe, as obtained in this work, is presented as an example in appendix A.

The degree of puckering is also found to vary considerably, depending on the type of rare-earth atom [13]. For example, the degree of puckering is almost negligible for LaAuGe and CeAuGe, but becomes increasingly pronounced for the smaller rare-earth atoms, where, in the case of ScAuGe, the Au(Ag)Ge network can be considered three dimensional. Therefore, these compounds may be described as belonging to one of two ternary ordered branches of the $CaIn_2$-type; the LiGaGe branch, where the Ga and Ge atoms form a three dimensional $[GaGe]_n$ network, or the NdPtSb branch, where the $[PtSb]_n$ polyanions form a slightly puckered two dimensional network with only very weak interactions

between layers.

The unit cell volume as a function of rare-earth species is plotted in figure 3.3 for the rare-earth gold germanides. From this a typical lanthanide contraction is evident, corresponding to the rare-earth ions in the 3+ oxidation state as expected. However, a strong positive deviation is observed for YbAuGe, indicating that Yb may be mixed valent between the 3+ and 2+ oxidation states[1].

3.2 Fe_2P-type

The compounds ScAgGe, YAgGe, SmAgGe-LuAgGe, and the annealed samples of PrAgGe and NdAgGe all crystallise as ternary ordered variants of the Fe_2P-type structure, where GdAgGe, DyAgGe, ErAgGe, and YbAgGe, have been previously reported by Zanicchi et al.[10], where they were examined by X-Ray powder diffraction. The lattice constants are shown in table 3.2, together with results of single crystal X-Ray diffraction [14, 24]. These compounds crystallise in the hexagonal system with space group $P\bar{6}2m$ (no. 189).

In the Fe_2P structure the rare-earth atoms are seen to occupy the Fe2 positions, the silver atoms the tetrahedral sites, and the germanium atoms the two trigonal prismatic sites. The projection of the structure on the *ab* plane is shown in figure 3.2(a), where the two different tri-capped trigonal prismatic sites, i.e. $[Ge1Dy_6Ag_3]$ and $[Ge2Dy_6Ag_3]$, are outlined. The dysprosium atoms, with a co-ordination number 17, are surrounded by six Dy, six Ag, and five Ge atoms. The five Ge neighbours form a tetragonal pyramid around the dysprosium atom, whereas the six silver neighbours form elongated trigonal prisms. The silver atoms are tetrahedrally co-ordinated by germanium atoms: two Ge1 at 271.7pm and two Ge2 at 274.6pm. The full crystallographic data for DyAgGe, which was solved as part of this work, is presented in appendix A as an example. Since the rare-earth ions are the largest electropositive component within these compounds, they will have mostly transfered their valence electrons to the [AgGe] polyanion. The compounds may therefore be described

[1]Since the writing of this thesis, three additional phases of YbAuGe have been prepared using different methods of heat treatment. The structures correspond to the different valency states of the Yb ions [26]

Table 3.1: Lattice constants of the REAuGe and REAgGe compounds crystallising in the ordered $CaIn_2$-type structure.

* These structures are refined from single crystal diffractometer data.

Compound	a(pm)	c(pm)	c/a	V(nm^3)	Ref.
ScAuGe*	430.82(2)	684.58(10)	1.589	0.1100	[13]
YAuGe*	441.00(3)	730.86(5)	1.657	0.1231	[16]
YAuGe	440.8(3)	730.7(3)	1.658	0.1230	[11] + This work
LaAuGe*	446.20(5)	816.05(8)	1.829	0.1407	[16]
LaAuGe	446.3(3)	816.9(3)	1.830	0.1409	[11] + This work
CeAuGe*	446.03(7)	793.60(12)	1.779	0.1367	[14]
CeAuGe	446.4(3)	791.0(3)	1.772	0.1365	[11] + This work
PrAuGe	445.7(3)	780.3(3)	1.752	0.1342	[11] + This work
NdAuGe	444.7(3)	770.2(3)	1.732	0.1319	[11] + This work
SmAuGe	443.4(3)	735.3(3)	1.699	0.1284	[11] + This work
GdAuGe	443.2(3)	741.8(3)	1.674	0.1262	[11] + This work
TbAuGe	441.6(3)	733.5(3)	1.661	0.1239	[11] + This work
DyAuGe	441.1(3)	728.7(3)	1.652	0.1228	[11] + This work
HoAuGe*	440.10(5)	723.26(9)	1.643	0.1213	[23]
HoAuGe	440.5(3)	723.9(3)	1.643	0.1216	[11] + This work
ErAuGe	439.7(3)	720.3(3)	1.638	0.1206	[11] + This work
TmAuGe*	439.08(4)	716.59(7)	1.632	0.1196	[13]
YbAuGe	447.5(3)	716.3(3)	1.601	0.1242	[11, 26] + This work
LuAuGe*	437.75(4)	711.38(6)	1.625	0.1181	[16]
LaAgGe	455.87(3)	789.69(6)	1.732	0.1421	[12]
CeAgGe	454.42(2)	771.08(7)	1.697	0.1379	[12]
PrAgGe	451.1(2)	766.1(1)	1.698	0.1350	This work
NdAgGe	451.3(1)	758.8(1)	1.681	0.1338	This work

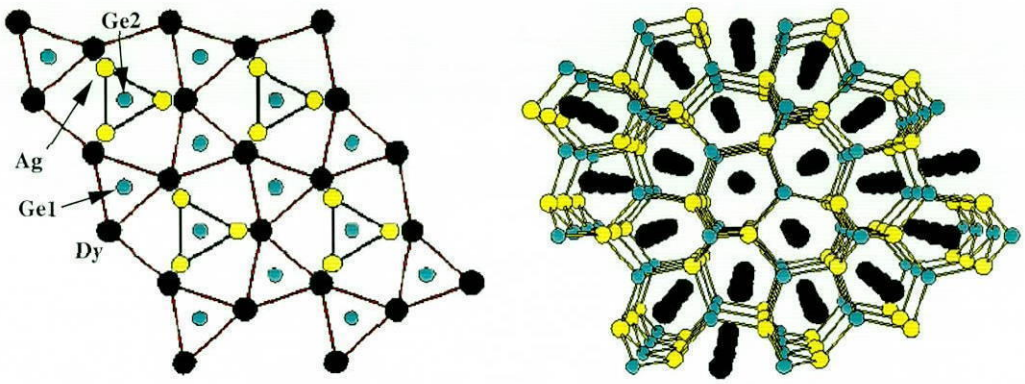

Figure 3.2: (left) Crystal structure of DyAgGe projected onto the *ab* plane. All atoms lie on mirror planes at z=0, and z=1/2, as indicated by the black and red lines, respectively. (right) Perspective view of DyAgGe along [0 0 1]. Black spheres represent the Dy atoms, yellow and blue spheres the Ag and Ge atoms, respectively.

to a first approximation by the formula $Dy^{3+}[AgGe]^{3-}$. The [AgGe] polyanion outlined in figure 3.2(b) forms large open tubes extending along the z-axis in which the rare-earth atoms are enclosed.

Again, a typical lanthanide contraction is clearly observed, as is shown in figure 3.3. YbAgGe deviates strongly from this rule due to the probable preferred divalent nature of Ytterbium.

3.3 $CeCu_2$-type

The two compounds, EuAuGe and EuAgGe, both crystallise as ternary variants of the orthorhombic $CeCu_2$-type structure, where the change in structure type reflects the fact that the Europium ions prefer the 2+ oxidation state. These compounds have been studied extensively by Pöttgen et al. in e.g. [15, 25], and are only mentioned here for completeness. Both EuAuGe and EuAgGe appear to have a similar crystal structure, with them both crystallising as ternary derivatives of the orthorhombic $CeCu_2$ type. However, single crystal X-Ray diffraction shows that the europium coordination in each case is quite different

Table 3.2: Lattice constants of the REAgGe compounds crystallising in the ordered Fe_2P-type structure.

* These structures are refined from single crystal diffractometer data.

Compound	a(pm)	c(pm)	c/a	V(nm^3)	Ref.
ScAgGe*	686.51(3)	402.95(2)	0.587	0.1645	[14]
YAgGe	711.80(6)	419.68(4)	0.589	0.1841	[10]
PrAgGe	724.1(2)	432.4(3)	0.597	0.196	This work
NdAgGe	725.0(1)	430.5(1)	0.594	0.196	This work
SmAgGe	720.05(9)	426.92(7)	0.593	0.917	[10]
GdAgGe*	715.54(6)	423.41(3)	0.591	0.1883	[24] + This work
GdAgGe	716.4	424.1	0.592	0.1885	[10]
TbAgGe*	712.77(7)	421.03(9)	0.591	0.1852	[24]
DyAgGe*	710.67(7)	419.73(5)	0.591	0.1836	[24] + This work
DyAgGe	710.5	419.8	0.591	0.1835	[10]
HoAgGe*	707.83(8)	418.26(6)	0.591	0.1815	[24]
ErAgGe*	706.34(3)	416.87(2)	0.590	0.1801	[24] + This work
ErAgGe	706.3	417.4	0.591	0.1803	[10]
TmAgGe*	704.15(2)	415.70(4)	0.590	0.1785	[24]
YbAgGe*	705.24(11)	413.87(8)	0.587	0.1783	[24] + This work
YbAgGe	705.9	414.7	0.587	0.1790	[10]
LuAgGe*	701.25(9)	413.37	0.589	0.1760	[24]

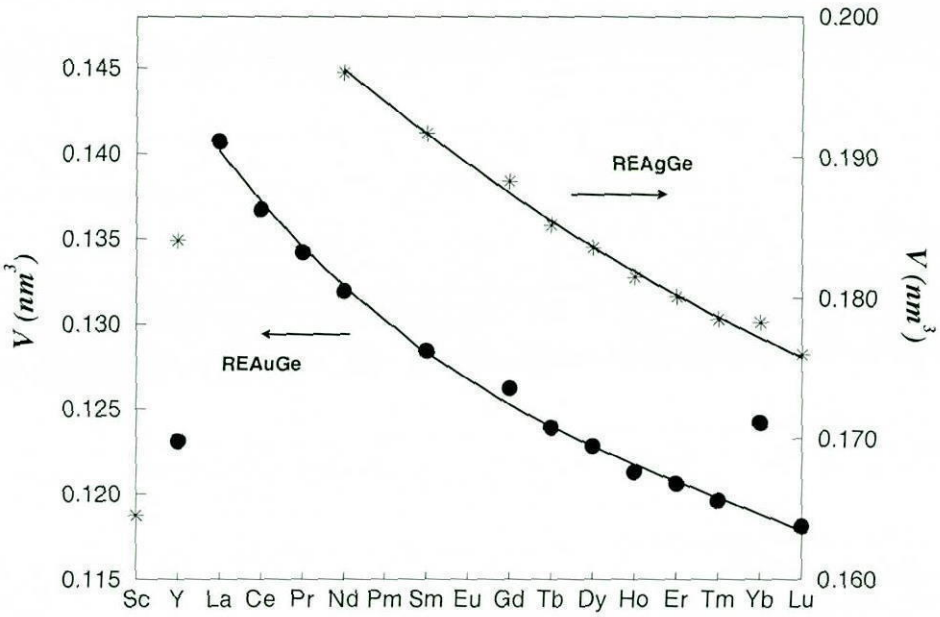

Figure 3.3: Unit cell volume as a function of rare-earth atom for REAuGe (left) and REAgGe (right).

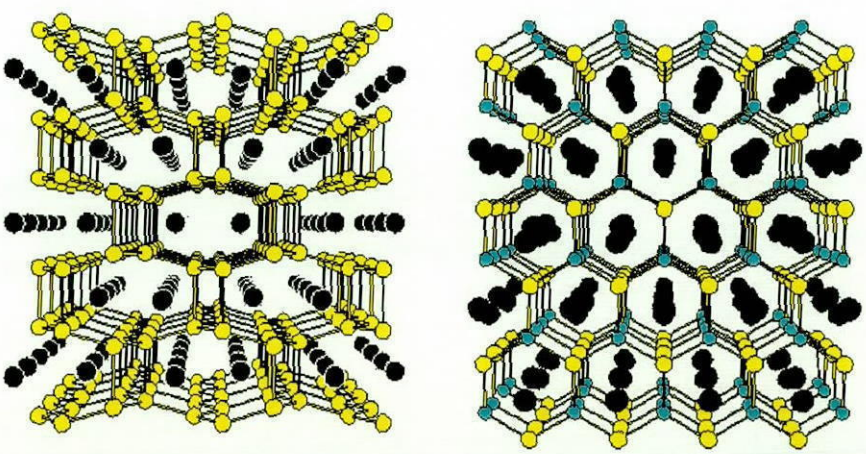

Figure 3.4: Perspective views of (left) EuAgGe, and (right) EuAuGe, along [0 1 0]. The Eu atoms are represented by black circles, Au(Ag) by yellow circles, and Ge by blue circles.

[15, 25]. The europium atoms occupy the Cerium positions in both germanides. In the case of EuAgGe, the silver and germanium atoms are seen to be statistically distributed on the copper sites (fig. 3.4(a)), whereas for EuAuGe, the gold and germanium atoms are ordered (fig. 3.4(b)).

Chapter 4

General Magnetic Properties

In this chapter the general magnetic properties of all the REAuGe and REAgGe compounds are systematically examined in order to investigate the overall trends of the magnetic behaviour within these compounds, and also as a prelude to the more specific investigations of later chapters. The magnetic properties are characterised by both magnetisation and heat capacity measurements. Both a.c. and d.c. susceptometers are used for this purpose, of which the experimental set-up and operation of the a.c. susceptometer is explained in more detail below. The heat capacity is measured on a calorimeter using Nernst's method [34], which is also discussed.

4.1 a.c. Susceptometer

The a.c. susceptometer equipment has been built up specifically as part of this doctoral work. Therefore a fairly detailed description of the instrument characteristics, along with its operation, are given.

4.1.1 Experimental Set-Up

The experimental set-up of the a.c. susceptometer is shown in figure 4.1. A polycrystalline sample ($\approx$100mg) is secured within the sample holder at the end of the sample rod using a

small amount of Appezion vacuum grease. The flexible sample rod may be top loaded into the variable temperature insert (V.T.I.) environment, which is subsequently closed, and flushed with ^{4}He gas. The sample is able to move between the two secondary coils by the action of the stepper motor. Both secondary coils are surrounded by a primary coil, whose input current and frequency are controlled by an Oxford Instruments a.c.s controller. The output of the secondary coils are picked up by an EG & G 5302 lock-in amplifier, and the output recorded on two Hewlett Packard 34401A multimeters, M.M.1 and M.M.2.
The V.T.I is immersed in an Oxford Instruments cryostat, containing a 12T Nb_3Sn superconducting magnet which is controlled by an Oxford Instruments PS-120-10 power source. The temperature at the sample, which may be varied between 1.5K and 300K by the dynamic action of a needle valve and heater, is regulated by an Oxford Instruments ITC-503 temperature controller. All instruments are controlled by a suite of LabView drivers running on a standard Pentium PC, with automatic data collection by a user defined control program.

4.1.2 Principles of Measurement

The technique of a.c susceptibility allows the direct measurement of $\chi_{\text{a.c}} = dM/dH$, including both the in and out of phase components, χ' and χ''. An oscillating magnetic field is produced by a solenoid, serving as a primary in a transformer circuit. The solenoid is driven by an a.c. current source with variable amplitude and frequency. A static field may also be provided, in this case, by an external superconducting magnet. Two oppositely wound sensing coils are positioned within, and concentric to, the primary coil. These may be considered as the secondary coils in the transformer circuit.
If a sample is positioned in the centre of one of the sensing coils, the voltage equilibrium is disturbed. The resultant voltage is proportional to the susceptibility of the sample according to

$$v = \frac{1}{\alpha} V f H \chi \tag{4.1}$$

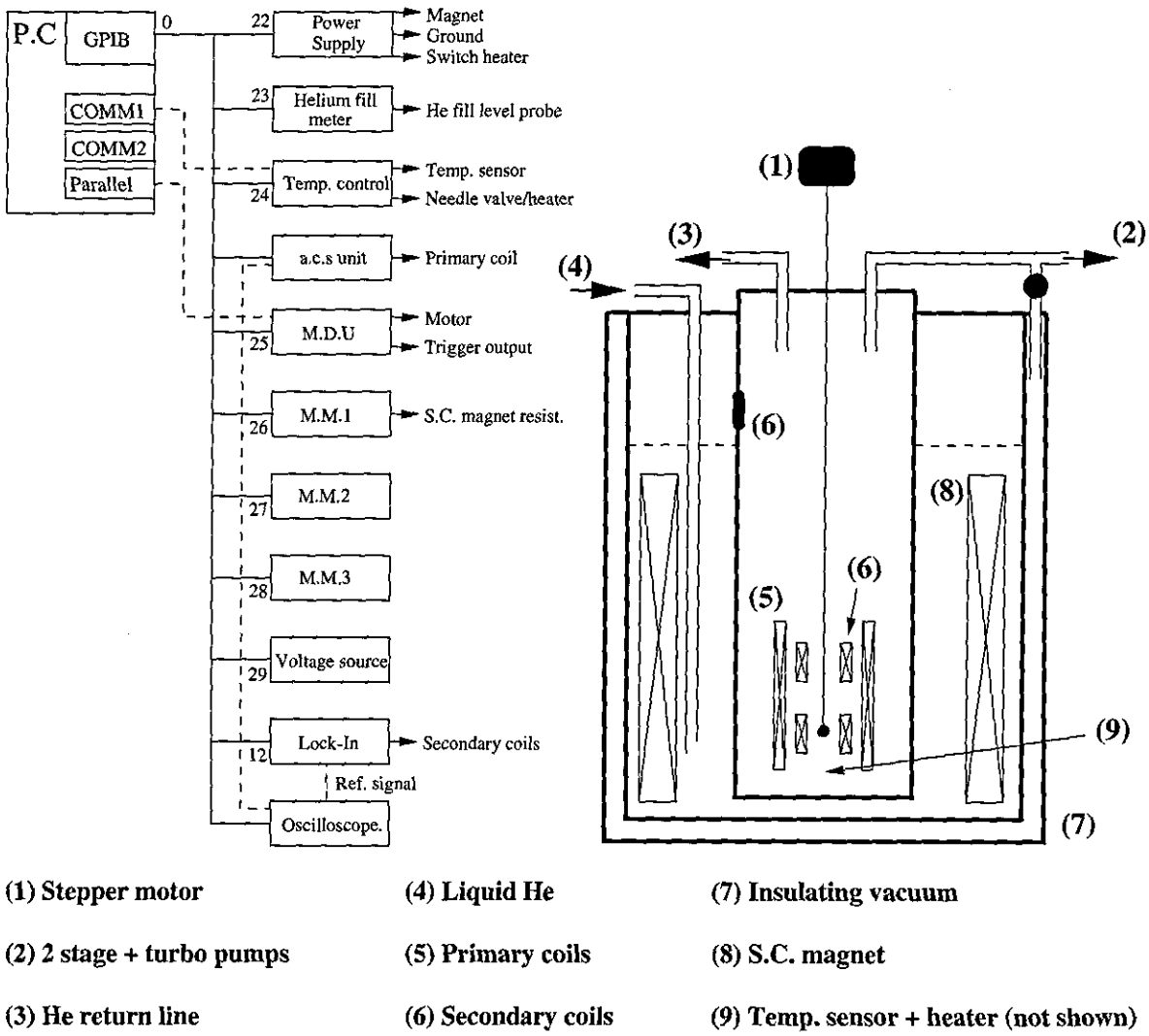

(1) Stepper motor **(4) Liquid He** **(7) Insulating vacuum**

(2) 2 stage + turbo pumps **(5) Primary coils** **(8) S.C. magnet**

(3) He return line **(6) Secondary coils** **(9) Temp. sensor + heater (not shown)**

Figure 4.1: Schematic diagram of the a.c. susceptometer.

where v is the measured R.M.S voltage, α is a calibration co-efficient, V is the sample volume, f is the a.c field frequency, H is the R.M.S magnetic field, and χ is the volume susceptibility of the sample.
From equation 4.1 it is evident that that the susceptibility is dependent upon the sample volume, and the magnetic field strength and frequency.

Sample Movement

The electronic sensitivity of the equipment is far in excess of the precision to which two identical secondary coils can be manufactured. The result is a slight offset voltage, which is evident from the small signal that persists when no sample is present. This offset voltage is compensated by recording the voltage with the sample positioned in each coil. The voltage recorded when the sample is in the upper coil, v_1 is composed of two components, a real signal, v, due to the sample, and an offset voltage, v_0, such that

$$v_1 = v + v_0 \tag{4.2}$$

Equivalently, in the lower coil, where the polarity of the real signal is reversed, the recorded voltage, v_2 is

$$v_2 = -v + v_0 \tag{4.3}$$

where v_0 is the same in both cases. The offset voltage is thus eliminated by subtraction.

Demagnetisation Factor

In the case of large susceptibilities, e.g. in ferromagnets, superconductors, or when very precise measurements are required, demagnetisation effects must be taken into consideration, and equation 4.1 corrected accordingly. This is a strictly geometrical effect, and arises because the internal field of the sample may differ from the external applied field. The corrected internal susceptibility is given by

$$\chi_{int} = \frac{\chi_{ext}}{1 - D\chi_{ext}} \tag{4.4}$$

where D is the demagnetisation factor, and varies according to the shape of the sample [27], but is approximately 1/3 for a sphere, and $\approx 1/2$ for a long cylinder with the applied field perpendicular to the long axis. The polycrystalline samples used are considered to be approximately spherical.

Calibration

There are two methods currently used to calibrate susceptometers; either using a standard reference material where the susceptibility is already known, or through a knowledge of the instrument geometry.

In the first method, a sample with a previously determined susceptibility and volume is measured. The calibration co-efficient can then be determined from equation 4.1. However, there is no 'absolute' standard, and this method is only strictly valid for samples of the same size and shape as the standard. The second method allows the calibration of the susceptometer without requiring a standard material, and is used in this case. This is an approximation based upon considering the sample to be a magnetic dipole. The given expression for the calibration co-efficient in cgs units is [28]

$$\alpha = (10^8/8\pi_2 NL)[L^2 + d^2]^{1/2} \tag{4.5}$$

with N the number of turns on the sensing coil, L the length of the sensing coil in cm, and d the diameter of the sensing coil in cm. This method gives accurate results in the limit of small sample size with respect to the secondary coils.

4.1.3 Sample Preparation and Measurement

The magnetic susceptibilities are measured on small polycrystalline pieces of the alloys (m$\approx$ 100mg) using both the a.c. susceptometer apparatus described above, and a standard

MPMS SQUID d.c. magnetometer [30]. Measurements are made between $\approx$ 2K and 380K in magnetic flux densities between 0.1T and 7T.

All the REAuGe and REAgGe have been measured, although only the magnetically ordered compounds are dealt with in this chapter. The non-magnetic compounds, Sc-, Y-, La-, and LuTGe, are considered separately in chapter 5. In addition, the two Cerium compounds, CeAuGe and CeAgGe, are first considered in chapter 6.

4.2 Specific Heat Capacity

The specific heat capacity measurements are performed using the equipment available in the low temperature group at the Max-Planck-Institut für Festkörperforschung. The specific apparatus used was built up by E. Gmelin and co-workers, and later developed by W. Schnelle, who also performed the measurements. Detailed descriptions of the methods and equipment can be found, e.g. in references [31, 32, 33].

4.2.1 Experimental Description

The apparatus allows measurements to be made within the temperature range, $2K < T < 100K$, and in a magnetic field up to 9T, with the calorimeter being built into a bath cryostat. The calorimeter used is enclosed within a copper can, as is shown in figure 4.2. The can may be evacuated to a high vacuum through the stainless steel tube. The insulating shield, made from gold plated copper, is screwed firmly onto the sample rod. The electrical connections to the sample holder are made from poorly heat conducting manganese wires, and heating wires are wound around the insulating shield. The sample is fixed to a sapphire plate, which, when hung on the thin wires, has minimal thermal contact to the heat bath. A gold resistor, which acts as the sample heater, and a Cernox thermometer, are both attached to the underside of the sapphire plate.

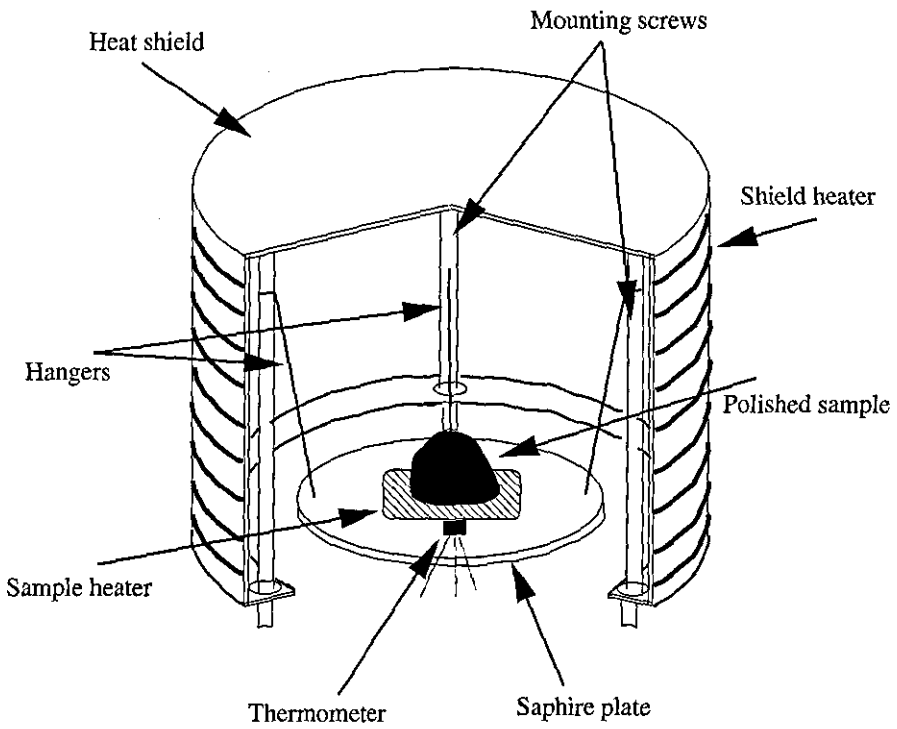

Figure 4.2: Schematic diagram of the specific heat capacity calorimeter.

4.2.2 Principles of Measurement

The measurements are performed using heat pulses, the so called Nernst method [34]. This technique utilises the definition of heat capacity

$$C = \lim_{\Delta T \to 0} \frac{\Delta Q}{\Delta T} \tag{4.6}$$

where ΔQ is the change in energy. The sample is kept under adiabatic conditions within the sample holder by reducing as far as possible the thermal contact with the heat bath. When the sample is in thermal equilibrium with the insulating shield within the time Δt, a constant electric power, $P = I^2R$, is formed from which the amount of heat energy, $\Delta Q = P \cdot \Delta t$, can be determined. The sample subsequently responds with a temperature increase of ΔT. In the ideal case of thermal isolation, the specific heat capacity will be exactly as in equation 4.6.

4.2.3 Sample Preparation

All of the samples, with the exception of YbAuGe and YbAgGe are prepared by taking large polycrystalline blocks of the compounds (1-2g for the non-magnetic compounds, 500mg for the rest), and polishing them on one side to ensure good thermal contact. They are subsequently mounted onto the sapphire sample holder of the calorimeter using a small amount of vacuum grease.

In the case of YbAuGe and YbAgGe, polycrystalline blocks of sufficient size do not form due to the preparation technique (Chapter 2.3). These are instead powdered and sealed in a DURAN glass container under a ^{4}He atmosphere to ensure good thermal contact.

4.3 Results

4.3.1 High Temperature Susceptibility

Plots of inverse magnetic susceptibility vs. temperature are shown in figures 4.3, 4.4, and 4.5 for all of the REAuGe and REAgGe (except CeAuGe and CeAgGe) compounds under consideration in this chapter. For all of the compounds, with the exception of SmAuGe, SmAgGe, YbAuGe, a linear temperature dependence of the inverse susceptibility is observed at high temperatures. Within this regime, the compounds are paramagnetic, and can be described using the well known Curie-Weiss law

$$\chi = \frac{M}{B} = \frac{C}{(T - \theta_P)} + \chi_0 \tag{4.7}$$

where M is the magnetisation in field B, θ_P is the paramagnetic Curie temperature, χ_0 contains temperature independent diamagnetic and Pauli paramagnetic contributions to the magnetic susceptibility and

$$C = \frac{N}{V}\frac{\mu_{eff}^2}{3\mu_0 k_B} \tag{4.8}$$

with

$$\mu_{\text{eff}} = g_{\text{J}}\sqrt{J(J+1)}\mu_{\text{B}} \tag{4.9}$$

The experimental curves are fitted at temperatures above 50K in order to exclude any deviations due to short range magnetic order or CEF effects that may occur close to the ordering temperatures. The results of the fits are listed in table 4.1, from which the following observations are made

- For each compound that follows the Curie-Weiss law, $\mu_{\text{eff}}^{\text{exp}}$ has a value that is in close agreement with $g_{\text{J}}\sqrt{J(J+1)}$ that is expected for the corresponding free RE ion in the 3+ oxidisation state. This is confirmation that the full magnetic moment is localised on the RE atomic sites.

- In all cases, the paramagnetic Curie temperatures, θ_{P}, are very small and negative, which indicates that antiferromagnetic exchange interactions are predominant in these compounds.

The RKKY theory has been found to describe well the magnetic coupling that occurs between isolated magnetic moments where the magnetic coupling between 4*f*-electrons is predominately mediated by conduction electrons. This coupling was originally calculated by Rudermann and Kittel for nuclear moments in a free electron gas. It was later extended to the case of coupling between 4*f* magnetic moments by Kasuya and Yosida, and is now known as the RKKY interaction. The interaction Hamiltonian is written as

$$H_{\text{ex}} = -\frac{1}{2}\sum_{i,j} J_{\text{ex}}(\vec{R}_i - \vec{R}_j)\vec{J}_i\vec{J}_j \tag{4.10}$$

where the sum is over all the rare-earth ions with total angular momentum $\vec{J}_i$. The effective exchange parameter, $J_{\text{ex}}(\vec{R}_i - \vec{R}_j)$, is proportional to the RKKY function, F, as

$$J_{\text{ex}}(\vec{R}_i - \vec{R}_j) = F[2\vec{k}_{\text{F}}(\vec{R}_i - \vec{R}_j)] \tag{4.11}$$

where

$$F(x) = \frac{x\cos x - \sin x}{x^4} \tag{4.12}$$

and where $\vec{k}_F$ is the Fermi wave vector. From the RKKY theory it is expected that the corresponding critical temperature, T_{RKKY}, and the paramagnetic Curie temperature are proportional to the so-called DeGennes factor, $(g_J - 1)^2 J(J+1)$, and related to the exchange parameter as [36]

$$T_{RKKY} = n(E_F) J_{ex}^2 \cdot (g_J - 1)^2 J(J+1) \tag{4.13}$$

where $n(E_F)$ is the density of states of the conduction electrons at the Fermi level, E_F. The DeGennes factors, as scaled to GdAuGe and GdAgGe for the REAuGe and REAgGe series respectively, are presented in figure 4.6. It is observed that there is very little correlation between the ordering temperatures of the REAuGe and REAgGe compounds with the DeGennes scaling law. This is attributed to CEF effects which split the (2J+1) manifolds. As suggested by the low ordering temperatures, magnetic ordering may be expected to predominately occur in the CEF ground-state. The values of the Ce and Sm compounds stand out in particular as having anomalously high ordering temperatures.
The RKKY theory is, however, based upon some very simplified assumptions, such as a spherical Fermi surface, which is usually far from the real situation. Also, the different character of the *s*- and *d*- states are not distinguished within the RKKY theory. Therefore, the theory may only be strictly treated as a phenomenological one and cannot be used for exact quantitative descriptions of the exchange interactions.
SmAuGe and SmAgGe are somewhat exceptional in that they cannot be described using the usual Curie-Weiss law. $1/\chi_{mol}$ vs. T of SmAuGe and SmAgGe is plotted in figure 4.5. Deviations from Curie-Weiss behaviour have been experienced previously in Sm based compounds [35, 37], and are seen to arise from the close proximity of the first excited energy states to the ground state. The energy separation between the ground state multiplet of the Sm^{3+} ion ($^6H_{5/2}$) and the first excited multiplet ($^6H_{7/2}$) is approximately 1400K [38], which is much smaller than found in other RE^{3+} ions. This is still larger than the typical

crystal field splittings ($\approx$ 100K), but the effects of admixtures of excited states into the ground state are still substantial. To describe the effects connected with the redistribution of the population over the excited multiplets, additional terms of [35, 37]

$$\frac{C_i}{(T-\theta_P)}e^{-\Delta_i/T} \tag{4.14}$$

where the C_i are the Curie constants and Δ_i are the corresponding energy separations from the ground state, have to be added to the Curie-Weiss expression of equation 4.7. According to the fits to the inverse susceptibility, shown in figure 4.5 by the full lines, this would in theory lead to a minimum in the susceptibility at higher temperatures ($T \approx 400$K), but measurements at elevated temperatures (350K - 800K) have proven inconclusive due to the degradation of the compounds above $\approx$ 600K. The curves are fitted assuming the first excited state, Δ_i, to lie at 1400K. The calculated values of $\mu_{\mathrm{eff}}^{\mathrm{exp}}$ and θ_{P} are tabulated in table 4.1 and correspond to the Sm^{3+} ion oxidation state for both SmAuGe and SmAgGe. The large deviation of the fits from the experimental curves at low temperatures corresponds to antiferromagnetic ordering effects below T_{N}. In addition, SmAuGe shows a small anomaly at $T \approx 60$K. It is likely that this could correspond to small impurities within the measured sample.

YbAuGe also does not follow the usual Curie-Weiss law. However, in this case, this may be attributed to the mixed valency of the Yb ions, lying between 3+ and 2+, as is suggested by the significant deviation in the unit cell volume from that expected due to the lanthanide contraction (figure 3.3).

In the case of TbAgGe, and the unannealed preparation of PrAgGe, the susceptibility cannot be satisfactorily measured due the the large amounts of until now unidentified magnetic impurity phases in these compounds. The impurities are observed as the large deviations from the Curie-Weiss law at $\approx$ 240K for TbAgGe, shown in figure 4.4(top, open triangles), and at $\approx$ 90K for unannealed NdAgGe, as shown in figure 4.4(bottom, crosses).

Table 4.1: Magnetic data for the S=1/2 REAuGe and REAgGe as derived from susceptibility measurements.

Compound	$T_{C/N}$(K)	$\mu_{eff}^{exp}(\mu_B)$	$g_J\sqrt{J(J+1)}$	θ_P(K)	Ref.
CeAuGe	10.0(2)	2.55(5)	2.54	-5(1)	[15] + this work
PrAuGe	4.1(5)	3.54(5)	3.58	-7(1)	This work
NdAuGe	7.5(5)	3.57(5)	3.62	-8(1)	This work
SmAuGe	17.5(5)	0.98(5)	0.85	-86(2)	This work
EuAuGe	32.9(2)	7.40(5)	0.00	33(1)	[25]
GdAuGe	16.9(5)	7.40(5)	7.94	-20(1)	This work
TbAuGe	7.2(5)	9.44(5)	9.72	-12(1)	This work
DyAuGe	4.2(5)	10.1(2)	10.6	-5(1)	This work
HoAuGe	6.0(3)	10.2(2)	10.6	0(1)	This work
ErAuGe	4.3(2)	9.5(2)	9.58	-4(1)	This work
TmAuGe	< 5.0	7.25(5)	7.56	0(1)	This work
YbAuGe	< 2.5	non-CW	4.54	non-CW	This work
CeAgGe	4.9(2)	2.61(5)	2.54	-9(1)	[12] + this work
PrAgGe-LT	< 2.5	3.5(1)	3.58	-9(2)	This work
PrAgGe-HT	6.2(2)	3.5(1)	3.58	-12(1)	This work
NdAgGe-HT	5.8(2)	3.7(1)	3.62	-15(1)	This work
SmAgGe	25(1)	0.92(5)	0.85	-57(2)	This work
EuAgGe	18(1)	7.7(1)	0.00	-2(1)	[25]
GdAgGe	13.0(2)	7.7(1)	7.94	-23(1)	[24] + this work
TbAgGe	Impurities		9.72	—	
DyAgGe	14.0(2)	10.3(1)	10.6	-11(1)	[24] + this work
HoAgGe	11.2(3)	10.2(1)	10.6	-8(1)	This work
ErAgGe	3.3(1)	9.1(1)	9.58	-1(1)	[24] + this work
TmAgGe	4.1(2)	7.4(1)	7.56	-9(1)	This work
YbAgGe	2.9(5)	4.3(1)	4.54	-54(1)	This work

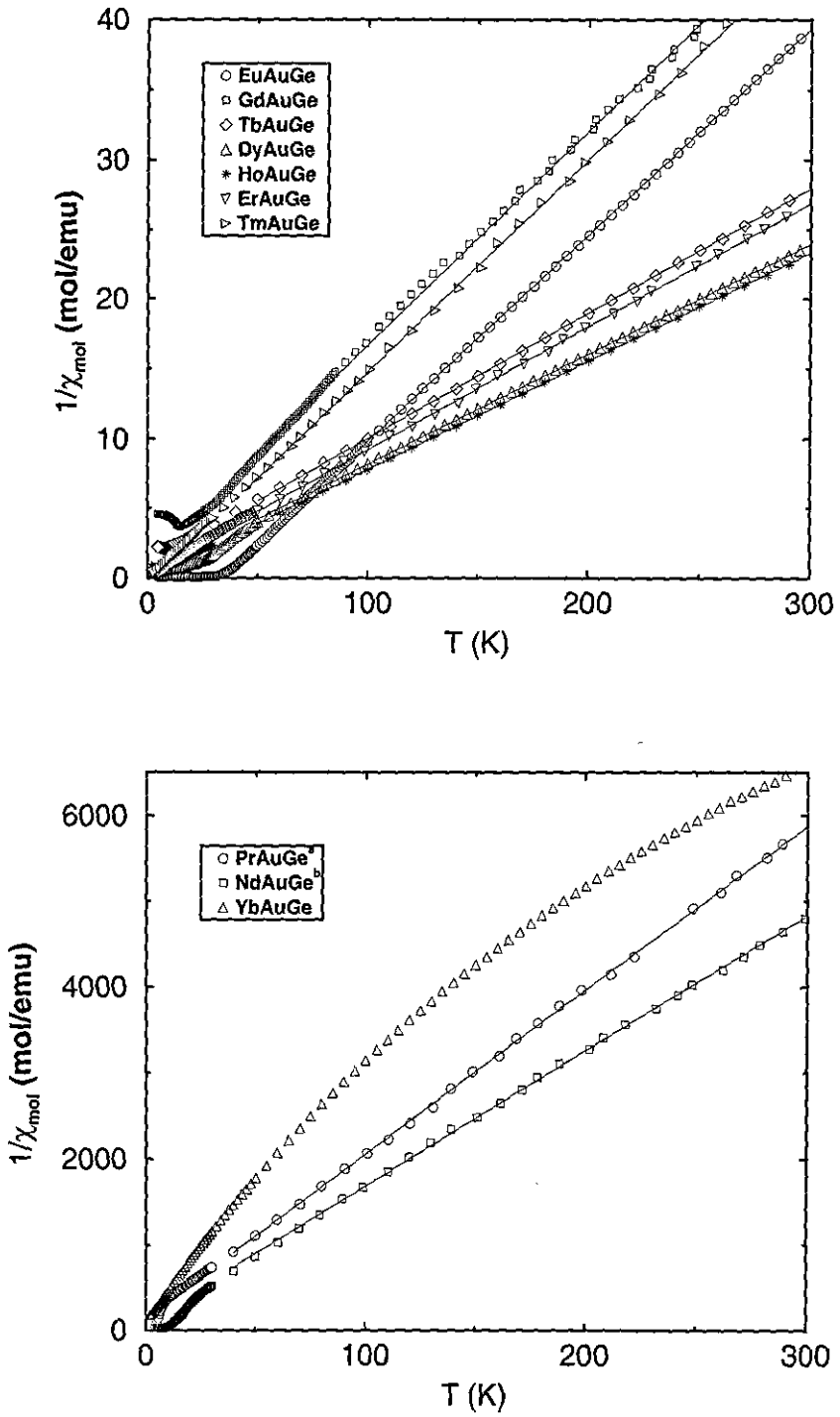

Figure 4.3: Inverse d.c. susceptibilities of selected REAuGe compounds. The solid lines represent fits to the Curie-Weiss law with the parameters listed in table 4.1.
[a,b]Susceptibilities of PrAuGe and NdAuGe (bottom) scaled up by factors of 30 and 25, respectively.

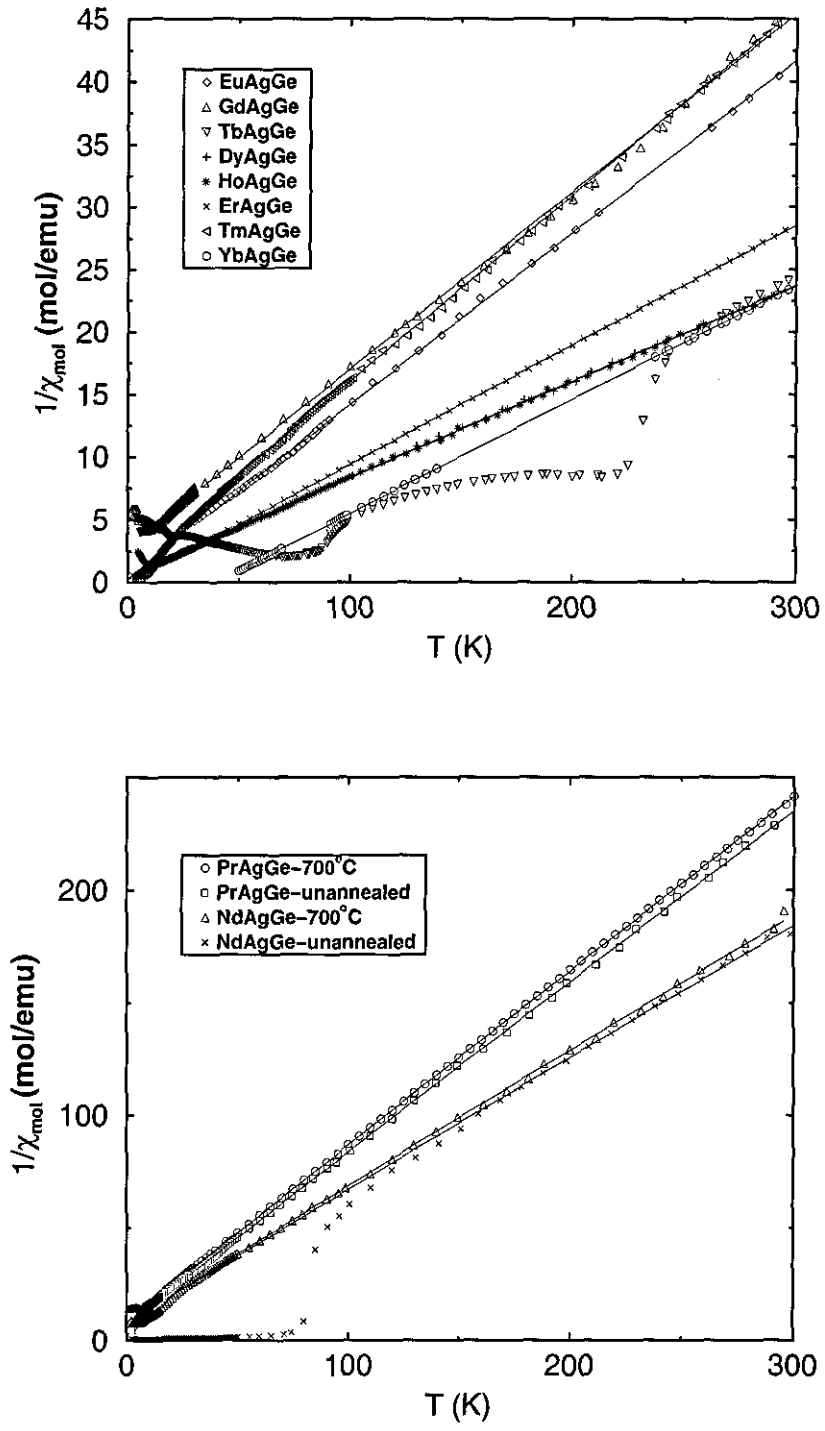

Figure 4.4: Inverse d.c. susceptibilities of selected REAgGe compounds. The solid lines represent fits to the Curie-Weiss law using the parameters listed in table 4.1.

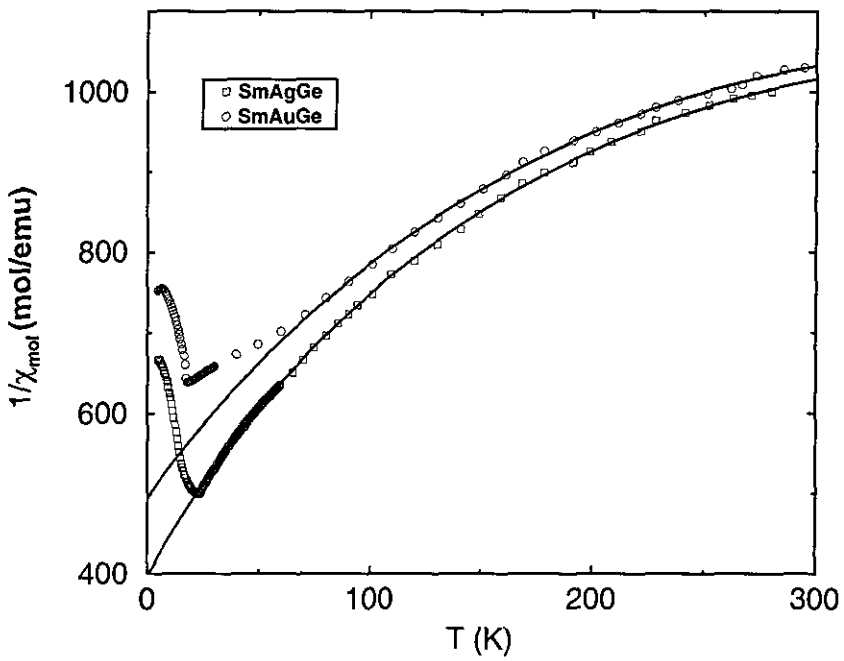

Figure 4.5: Inverse d.c. susceptibilities of SmAuGe and SmAgGe.

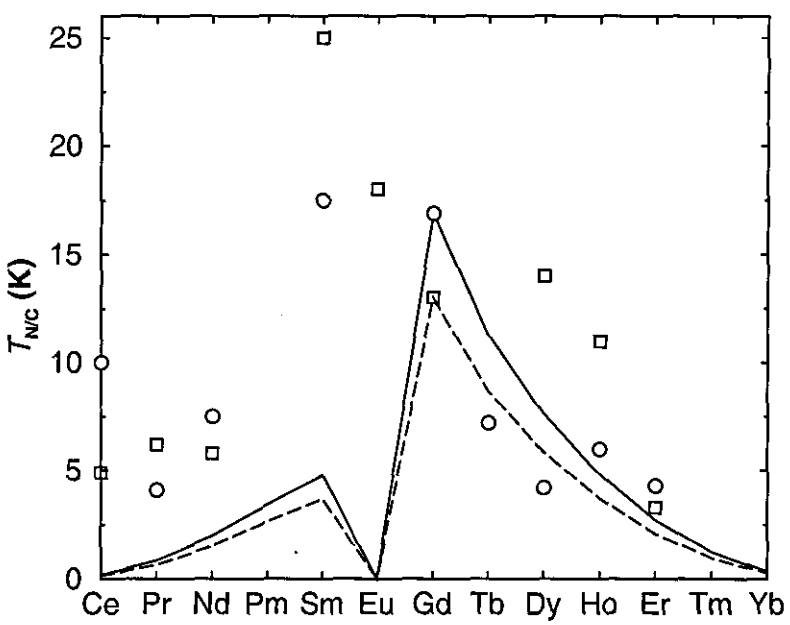

Figure 4.6: DeGennes plots for REAuGe (circles) and REAgGe (squares). The full and dashed lines represent the DeGennes factors scaled up to GdAuGe and GdAgGe, respectively.

4.3.2 Magnetic Ordering in RETGe

Nearly all of the REAuGe and REAgGe compounds display a transition to a magnetically ordered state at low temperatures (T< 20K). The transition temperatures of all the REAuGe and ReAgGe compounds are derived from the susceptibility and specific heat capacity measurements of this chapter, and are listed in column two of table 4.1. Magnetic susceptibility plots of selected compounds are presented in figures 4.7 and 4.8. The compounds in these plots display various kinds of anomalies in their susceptibility and specific heat measurements due to magnetic ordering. The majority of the REAuGe and REAgGe compounds are seen to order antiferromagnetically below the Néel temperature, T_N. This transition is characterised by a peak in the susceptibility, as, e.g., is characteristic of ErAgGe, shown in figure 4.8(open triangles). CeAuGe and DyAgGe are observed to order ferromagnetically below the Curie temperature, T_C. Both of these compounds are examined in greater detail in later sections. YbAuGe and YbAgGe display interesting and contrasting magnetic ground states. YbAuGe, as shown in figure 4.7, remains paramagnetic down to the lowest measured temperature of $T = 1.5$K, whereas a broad peak in χ_{mol} is observed for YbAgGe at $T = 2.9(5)$K (figure 4.8, crosses). The lack of magnetic ordering in YbAuGe may be explained in terms of its (almost) complete divalent nature ($4f^{14}$), as is proposed by the large positive deviation in unit lattice volume from the lanthanide contraction trend shown in figure 3.3. The deviation of YbAgGe in this volume plot (figure 3.3) is not nearly as strong as for YbAuGe, suggesting a mixed-valent state between 3+ and 2+. This is reflected by the magnetic ordering as demonstrated in the χ_{mol} vs. T curve in figure 4.8. The ordering temperature of TbAgGe cannot be determined due to the large magnetic impurity content of the prepared sample.

In addition to the magnetic ordering described above, a few of the REAuGe and ReAgGe compounds display magnetic properties that warrant special consideration, and which are studied individually in the following sections. The compounds are

- *CeAuGe and CeAgGe*

  As previously mentioned in chapter 1, the possibility of heavy fermion behaviour

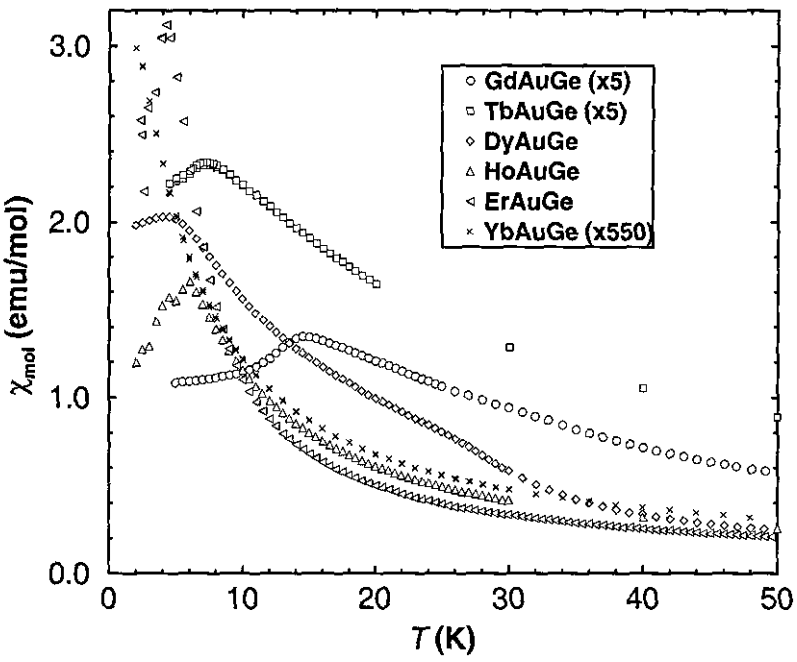

Figure 4.7: Low temperature magnetic susceptibilities of the heavy REAuGe compounds.

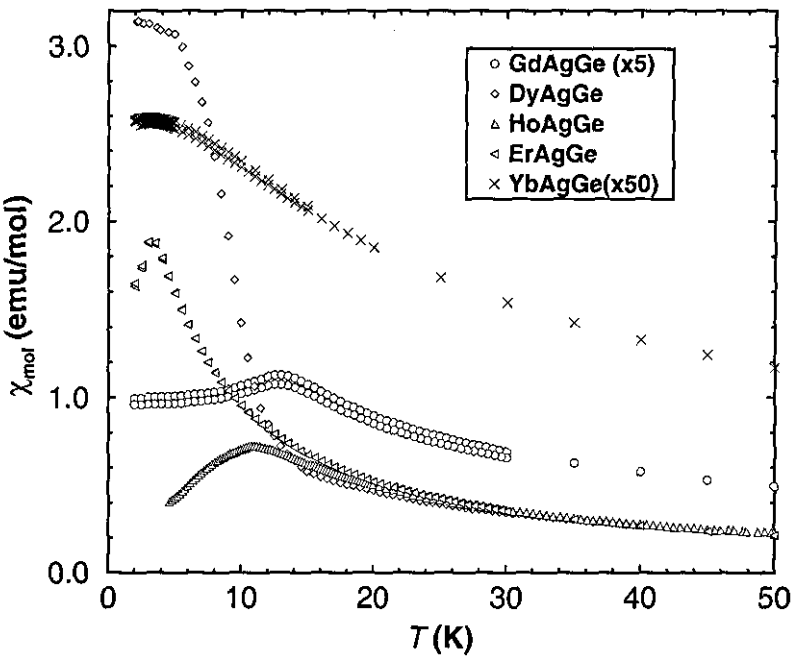

Figure 4.8: Low temperature magnetic susceptibilities of the heavy REAgGe compounds.

makes all Ce containing intermetallic compounds interesting. In particular though, the contrasting magnetic ordering within these two isostructural compounds (CeAuGe - ferromagnetic, CeAgGe - antiferromagnetic) makes them worthy of attention. Chapter 6 is devoted entirely to these compounds, and their susceptibility and specific heat capacities are discussed in detail there.

- *HoAuGe and ErAuGe*

  HoAuGe and ErAuGe display multiple magnetic ordering transitions below T_N. In addition, the heavy RE atoms are ideal candidates for magnetic neutron scattering due to their large magnetic moments, which makes the magnetic scattering cross-section of comparable magnitude to nuclear cross-sections. This enables the magnetic spin arrangement to be determined. The magnetic structures are examined in chapter 7, and require a knowledge of the basic magnetic properties.

- *DyAgGe*

  DyAgGe appears to be ferromagnetic from susceptibility measurements, with several metamagnetic transitions being observed at high fields. However, its magnetic structure as determined from magnetic neutron scattering at $T = 1.5$K is observed to be non-ferromagnetic.

HoAuGe

The magnetic susceptibility of HoAuGe below $T = 50$K is plotted in figure 4.9. A sharp antiferromagnetic phase transition is observed at $T_N = 5.6(2)$K. Below T_N, two additional transitions are observed at $T_1 = 4(1)$K and $T_2 = 2(1)$K. The two transitions, T_1 and T_2, are probably the result of re-ordering ('relaxation') of the Ho magnetic moments. In addition, the magnetic moment as a function of external field, H_{ext}, is displayed in the insert of figure 4.9. It is seen that a metamagnetic transition occurs at $H_{ext} = 0.4$T in the $T = 2$K isotherm. This transition probably corresponds to one of the magnetic structure changes occurring at T_1 or T_2. In the maximum field of $H_{ext} = 7$T, the Ho magnetic ions still have not reached saturation. At $T = 7$T the magnetic moment, m, has a value of

$7.2\mu_B$/Ho atom, which is significantly reduced when compared to the corresponding value of $g_J \cdot J = 10\mu_B$ that is theoretically calculated for Ho^{3+}. This reduced Ho moment may probably be attributed to CEF effects.

The results of the specific heat capacity measurements are shown in figure 4.10, where the measured specific heat capacity is represented by open circles. Transitions in the specific heat capacity are clearly observed at temperatures of $T_N = 5.6(2)$K, $T_1 = 3.5(2)$K, and $T_2 = 2.4(2)$K, which correspond closely to the magnetic transitions observed in the susceptibility measurements. However, the resolution of the c_p measurement is much greater than for χ_{mol}, and T_N, T_1, and T_2, are determined to a greater accuracy. For the peak at T_1 the transition is seen to be composed of a cluster of two or three peaks.

The total specific heat capacity of HoAuGe may be considered to be composed of three contributions

$$c_{p[total]} = c_{p[el]} + c_{p[latt]} + c_{p[m]} \tag{4.15}$$

where $c_{p[el]}$ is the electronic contribution from conduction electrons, $c_{p[latt]}$ is the lattice contribution, and $c_{p[m]}$ is the contribution arising from magnetic effects due to the $4f$ moments on the RE atoms. In order to separate these individual terms, the electronic and lattice contributions are calculated on the basis of the isostructural and non-magnetic compound, LuAuGe, in which the phonon (lattice) and electronic properties should be very close to those of HoAuGe. This contribution is depicted in figure 4.10 by open squares. The specific heat capacity of LuAuGe has been previously calculated by W.Schnelle et al. [16], the results of which are re-examined in chapter 5.

When the lattice and electronic contributions to the specific heat capacity are subtracted from the measured specific heat capacity, only the contribution arising from magnetic effects remains. This is represented by the open triangles in figure 4.10. This curve contains the sharp peaks resulting from magnetic ordering at $T_N = 5.6(2)$K, $T_1 = 3.5(2)$K, and $T_2 = 2.4(2)$K and also a broad 'hump' above T_N centred at $T_{Schottky} \approx 24$K. This is a so-called Schottky anomaly which arises from crystalline electric field (CEF) excitations.

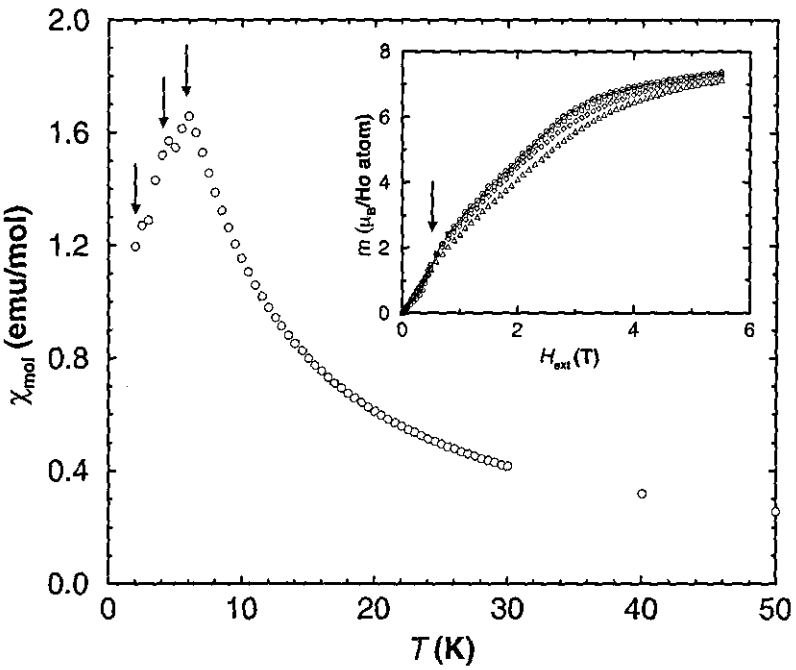

Figure 4.9: Low temperature magnetic susceptibility HoAuGe taken in an external field of $H = 0.1$T. The insert shows Ho magnetic moment as a function of applied field.

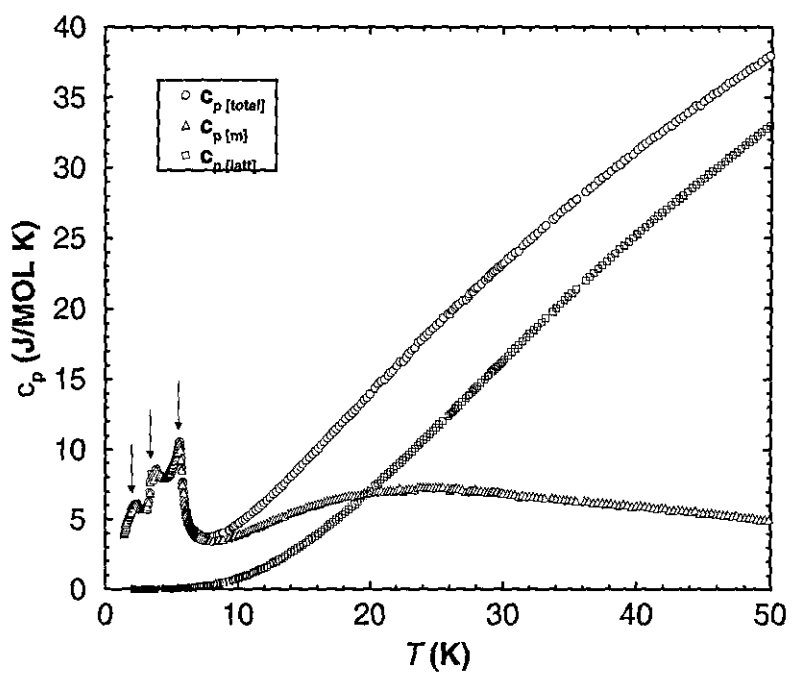

Figure 4.10: Specific heat capacity of HoAuGe. Open circles represent the measured data, while the squares and triangle represent lattice and magnetic contributions, respectively. Magnetic transitions are identified by arrows.

Ho is a non-Kramers ion, and has a ground-state of $^5I_8$, i.e. with integral total angular momentum. According to the Kramers theorem Ho may form a singlet ground-state according to its local C_{3v} site symmetry. Due to CEF action, the ground-state is expected to split into 2J+1=17 individual states.

The Schottky anomaly has a maximum in c_p at $T_{Sch} \approx 24$K, and the first excited states are estimated to lie at an energy approximately 50K above the ground state.

ErAuGe

The magnetic susceptibility of ErAuGe below $T = 50$K is plotted in figure 4.11. A sharp antiferromagnetic phase transition is observed at $T_N = 4.3(2)$K. Below T_N, one additional transition is observed at $T_1 = 3(1)$K, in a similar manner to HoAuGe and also probably correspond to re-orientation of the Er ion spins. The insert of figure 4.11 displays the Er magnetic moment as a function of applied external field at $T = 1.9$K and $T = 100$K. A metamagnetic transition is observed in the 1.9K isotherm at $H_{ext} = 0.1$T. Saturation of the Er magnetic moment is almost reached at $H_{ext} = 7$T, and amounts to a value of $4.9\mu_B$/Er atom, which is about half the value expected for Er of $g_J \cdot J = 9\mu_B$.

The results of specific heat capacity measurements on ErAuGe are shown in figure 4.12. Again, the total specific heat capacity may be split into three components. The electronic and lattice contributions are subtracted using the same method as for HoAuGe, and using the same non-magnetic compound, LuAuGe, as a basis. From the remaining curve (open triangles), composed of only magnetic contributions, sharp maxima are observed at $T_N = 4.3(1)K$ and $T_1 \approx 3$K in correspondence with the susceptibility data.

Above T_N, a very large Schottky anomaly is observed with a maximum at $T_{Sch} \approx 45$K. In contrast to Ho, Er is a Kramers ion, and has a ground-state of $^4I_{15/2}$, i.e. with non-integral total angular momentum, and is expected to form a doublet CEF ground state. Due to CEF excitations, the $J = 15/2$ ground state is expected to split into eight doublet levels, which can be fitted to the Schottky anomaly according to

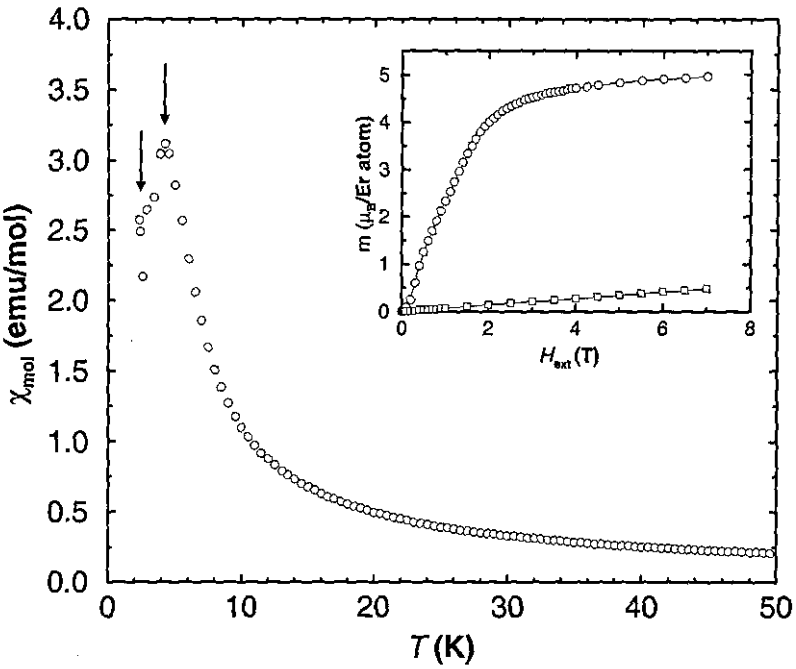

Figure 4.11: Low temperature magnetic susceptibility of ErAuGe taken in an external field of $H = 0.1$T. The insert shows the Er magnetic moment as a function of applied field at $T = 1.9$K(o) and $T = 100$K(□).

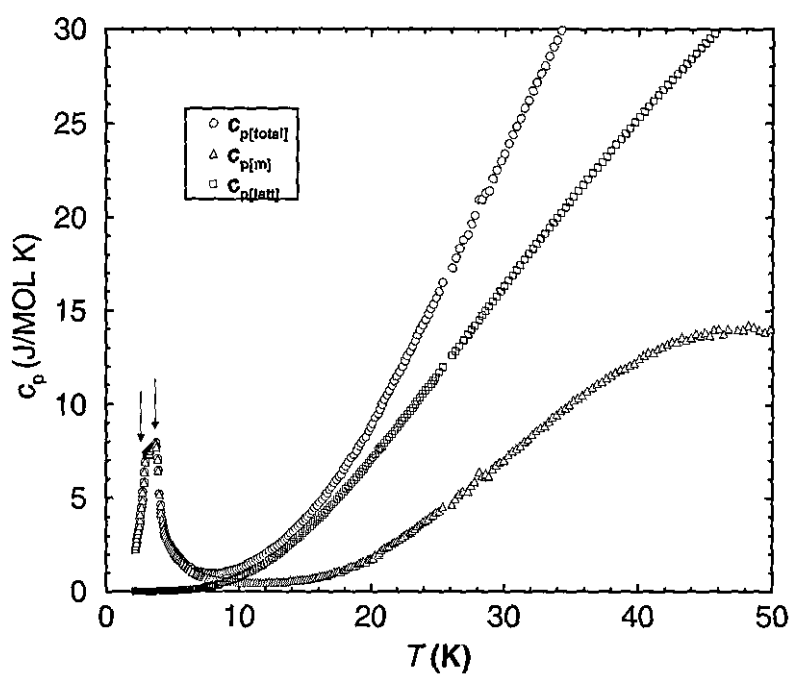

Figure 4.12: Specific heat capacity of ErAuGe. Open circles represent the measured data. Triangles and squares represent the magnetic and lattice contributions, respectively.

$$c_{\mathrm{p,Sch}} = -\frac{d^2(k_{\mathrm{B}}TlnZ)}{dT^2} = \frac{k_{\mathrm{B}}}{T^2}\left[\sum_i \frac{E_i^2 \exp\left(-E_i/k_{\mathrm{B}}T\right)}{Z} - \left(\sum_i \frac{E_i^2 \exp\left(-E_i/k_{\mathrm{B}}T\right)}{Z}\right)^2\right] \tag{4.16}$$

where the E_i are energies and Z is the partition function

$$Z = \sum_i \exp\left(-E_i/k_{\mathrm{B}}T\right) \tag{4.17}$$

From the fit to the Schottky anomaly the excited doublet levels are calculated to lie at approximately; 1 doublet at 0K, 3 doublets at 150K, 3 doublets at 250K, and 1 doublet at 270K.

DyAgGe

The magnetic susceptibility of DyAgGe below $T = 50$K is plotted in figure 4.13. A rather sharp ferromagnetic transition is clearly observed at $T_{\mathrm{C}} = 14.0(2)$K. This is examined further by magnetic field dependent measurements. The hysteresis curve of DyAgGe between $-6\mathrm{T} < H_{\mathrm{ext}} < 6\mathrm{T}$ at a constant temperature of $T = 4.5$K is shown in figure 4.14, and again in the insert of figure 4.13 where the region between $-1\mathrm{T} < H_{\mathrm{ext}} < 1\mathrm{T}$ is magnified for clarity. Several interesting features are observed. Firstly, DyAgGe is confirmed to be ferromagnetic by the remnant magnetic moment that persists as H_{ext} is lowered through 0T. The remnant magnetic moment has a value of $\mu_{\mathrm{exp}} = 0.5(1)\mu_{\mathrm{B}}$/Ho atom. Secondly, two metamagnetic transitions are seen to occur, which are labelled by the arrows in figure 4.14. These occur at fields of $H_{\mathrm{ext},1} \approx 0.55\mathrm{T}$ and $H_{\mathrm{ext},2} \approx 2.6\mathrm{T}$. In an external field of 6T, the Dy moments still have not reached saturation.

The measured specific heat capacity of DyAgGe is presented in figure 4.15 as shown by the open circles. Again, this is composed of magnetic, lattice, and electronic contributions. The lattice and electronic contributions are subtracted using the same method as with HoAuGe and ErAuGe. However, DyAgGe crystallises in a different structure type to HoAuGe and ErAuGe (Fe_2P) and consequently the non-magnetic and isostructural REAgGe compounds are utilised. The molar mass of Dy is approximately half way between La and Lu, so the

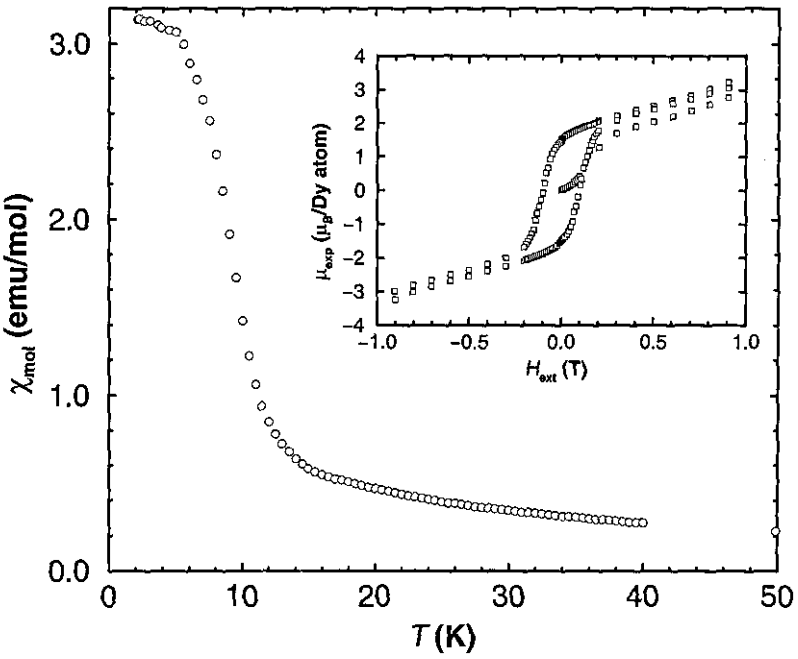

Figure 4.13: Low temperature magnetic susceptibility of DyAgGe taken in an external field of $H = 0.1$T. The insert shows the hysteresis curve of DyAgGe between $-1\text{T} < H_{\text{ext}} < 1\text{T}$.

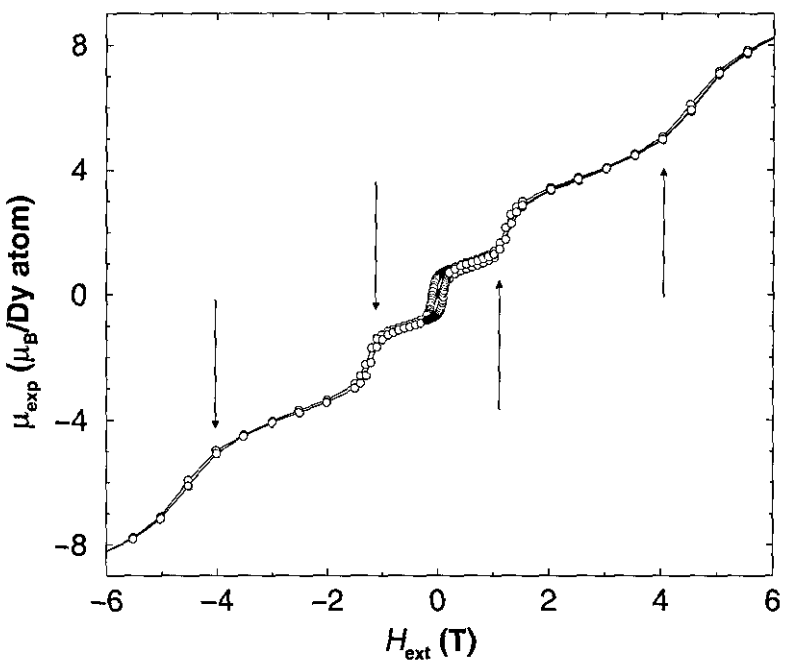

Figure 4.14: Hysteresis curve of DyAgGe.

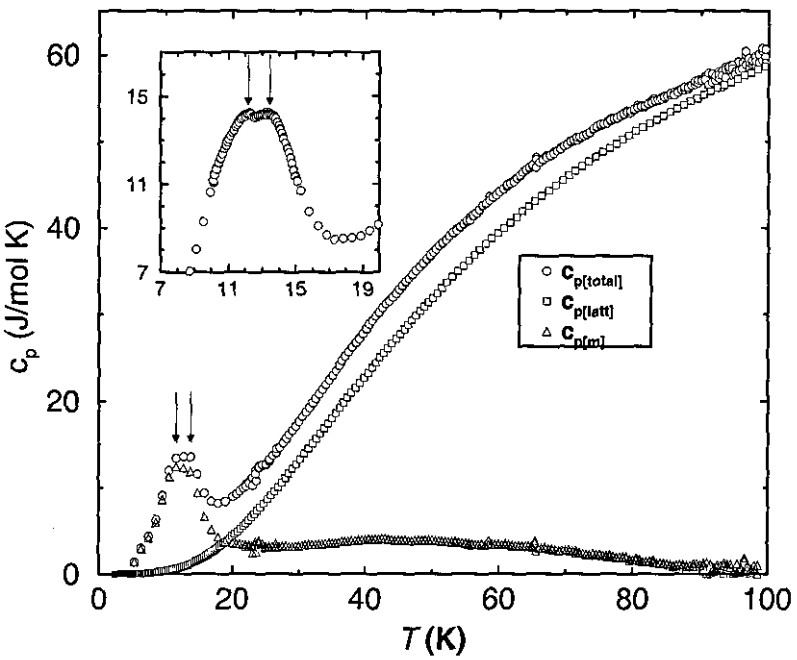

Figure 4.15: Specific heat capacity of DyAgGe. Open circles represent the measured data. Triangles and squares represent the magnetic and lattice contributions, respectively. The insert shows a magnification of the double magnetic ordering peak.

average between the specific heat capacities of LaAgGe and LuAgGe give the best fit. The remaining, purely magnetic, contributions are plotted as open triangles. A peak in the specific heat capacity is observed at $T_C = 14$K corresponding to the ferromagnetic ordering observed in the susceptibility measurements. However, upon closer inspection (figure 4.15, insert) the peak is shown to be split, with one maxima at $T_1 = 13.4(2)$K and another at $T_2 = 12.1(2)$K. As DyAgGe has an antiferromagnetic ground-state at lowest temperatures as determined from neutron scattering experiments (chapter 7), it is proposed that the first peak at T_1 corresponds to the ferromagnetic transition observed in the susceptibility measurements, and that the seconds peak at T_2 corresponds to a transition to an antiferromagnetic ground-state.

Above T_C, a very small, and broad 'hump' is observed centred around $T_{\text{Schottky}} = 42$K.

This Schottky anomaly corresponds to CEF excitations, which in the case of Dy, having a Kramers doublet ground-state, $^6H_{15/2}$, results in a splitting of the doublet ground-state into 2J+1=16 energy levels. Unfortunately, the quality of the data, combined with the large number of possible energy states (number of fitting parameters) make further predictions of the magnitude or splitting of the CEF excitations meaningless.

4.4 Discussion

Although the two series of intermetallic rare-earth compounds, REAuGe and REAgGe, crystallise in two completely different crystal structure types, the general trends in their magnetic properties are observed to be quite similar. All the RETGe compounds which can be prepared as single phase samples, with the exception of YbAuGe, follow the Curie-Weiss law at high temperatures. This is the usual type of behaviour found in rare-earth compounds where the interatomic spacing between rare-earth atoms is large enough to preclude any direct magnetic exchange interactions. The RKKY model describes the magnetic interaction between RE atoms as being 'carried' by the action of polarisation of the conduction electrons. This model, in conjunction with the DeGennes scaling law predicts a fixed relationship between the magnitudes of the ordering temperatures along a series of rare-earth compounds. In general, most series of rare-earth compounds follow this scaling law quite closely as, e.g., in the series RECuAl and RENiAl which are summarised by Javorsky in [39]. However, both REAuGe and REAgGe at best only approximate to this scaling law. One reason why the DeGennes law fails in this case could be due to large CEF effects, from low lying excited levels which can mix easily with the ground state, consequently altering the magnetic ordering. Indeed, in the two compounds that are studied further in this chapter, HoAuGe and ErAuGe, Schottky anomalies arising from excited CEF states are observed in the specific heat capacities, which supports this hypothesis.
A variety of magnetic ordering behaviour is observed in the REAuGe and REAgGe series of compounds. All of the light RETGe (RE=Pr-Sm, T=Ag,Au) compounds display simple antiferromagnetic ordering. CeAuGe and DyAgGe display ferro- or ferri-magnetic

ordering, YbAuGe remains paramagnetic down to lowest temperatures, and several of the heavy RETGe (RE=Tb-Tm, T=Ag,Au) compounds are antiferromagnetic with multiple magnetic transitions below T_N. In addition, several of these compounds also display metamagnetic transitions at various field strengths. It would be extremely interesting to know whether the magnetic transitions in temperature and magnetic field correspond to the same magnetic structure changes.

Chapter 5

Transport and Electronic Properties

5.1 Introduction

In this chapter, several of the transport and electronic properties of both the REAuGe and REAgGe (RE=Sc,Y,La,Lu) non-magnetic compounds are examined. As discussed in chapter 3, these compounds crystallise in two distinct structure types; Sc-, Y-, La-, LuAuGe, and LaAgGe all crystallise with a ternary ordered arrangement of the $CaIn_2$ structure type. Sc-, Y-, and LuAgGe crystallise with a ternary ordered arrangement of the Fe_2P structure type. It is therefore likely that the observed trends in the transport and electronic properties will depend strongly on the structure type.

The transport and electronic properties of the isostructural non-magnetic rare-earth gold germanides, REAuGe (RE=Sc,Y,La,Lu), have been recently examined by Schnelle et al. [16] at the Max-Planck Institut für Festkörperforschung. This study produced several interesting and thought-provoking results. From an analysis of resistivity, susceptibility, and specific heat capacity measurements in conjunction with band structure calculations several unusual physical properties that are borderline between metallic and semimetallic behaviour have been observed.

The results and conclusions reached from the study of the non-magnetic REAuGe are recounted in the following sections, together with an examination of the corresponding trans-

port and electronic properties of the REAgGe compounds. The differences and similarities in the physical properties between the two structure groups are subsequently discussed.

5.2 Electronic Structure Calculations

5.2.1 Experimental

The electronic structures of the four non-magnetic REAuGe compounds are calculated *ab initio* using the self consistent tight-binding LMTO-ASA method [40]. The experimental details for the REAuGe compounds are presented in [16] and are not recounted again here. The electronic structures of the four non-magnetic REAgGe compounds are also calculated *ab initio* by O. Jepsen using the self consistent tight-binding LMTO-ASA method in a similar manner to that described by Schnelle et al. [16]. A local exchange correlation potential is used [42], and all relativistic effects are included except for spin-orbit coupling. Only the relevant technical data used for the calculations are presented here. A full account of the TB-LMTO-ASA method may be found, e.g., in [40, 41].

The technical data for the calculation of the electronic structures of REAgGe (RE=Sc, Y, La, Lu) are listed in table 5.1. The inclusion of a partial wave (s = angular momentum 0, p = angular momentum 1, etc.) in the LMTO basis set is indicated by a l (meaning low), and an included partial wave that has been downfolded, is indicated by an i (meaning intermediate). S is the sphere radius in atomic units. E stands for interstitial spheres which have to be inserted in order to make the sum of the volumes of all of the spheres in the unit cell equal to the unit cell volume. The interstitial spheres are at the $a/3 + 2b/3$ equivalent positions. The sphere radii and the positions of the interstitial spheres are determined by an automatic algorithm developed by Krier et al. [43].

Table 5.1: Technical data concerning the band structure calculations of REAgGe. For LaAgGe, the interstitial site, E1 is in the Wyckoff position 2b with z=-0.2671, E2 is in 6c with x=0.43754 and z=0.2178, and E3 is in 12d with x=0.2297, y=0.2328, and z=0. For ScAgGe, YAgGe, and LuAgGe, the four equivalent interstitial are: E1 in the 3g position with x=-0.3058, -0.3047, and -0.3026, E2 in the 2c position, E3 in the 3f position with x=0.2822, 0.2803, and 0.2784, and E4 in the 3g position with x=0.4815, -0.4809, and -0.4814, respectively.

	s	p	d	f	S(a.u.)		s	p	d	f	S(a.u.)
Sc	l	l	l		3.222	Y	l	l	l	i	3.378
Ag	l	l	l		2.796	Ag	l	l	l		2.984
Ge1	l	l	i		2.906	Ge1	l	l	i		3.021
Ge2	l	l	i		2.993	Ge2	l	l	i		3.045
E1	l	i			1.446	E1	l	i			1.477
E2	l	i			1.220	E2	l	i			1.197
E3	l	i			1.214	E3	l	i			1.273
E4	l	i			1.189	E4	l	i			1.232
La	l	i	l	l	3.670	Lu	l	l	l	l	3.311
Ag	l	l	l		2.812	Ag	l	l	l		2.856
Ge	l	l	i		2.912	Ge1	l	l	i		2.973
E1	l	i	i		1.765	Ge2	l	l	i		3.025
E2	l	i			1.281	E1	l	i			1.472
E3	l	i			1.017	E2	l	i			1.211
						E3	l	i			1.252
						E4	l	i			1.228

5.2.2 Results

REAuGe

The calculated electronic structures of the four non-magnetic REAuGe compounds along selected symmetry lines within the first hexagonal Brillouin zone are shown in figure 5.1. The electronic structures are all observed to be similar, with only LaAuGe showing significant differences.

The corresponding density of states are shown in figure 5.2. Here, the Fermi level is placed at the zero of energy ($E_F = 0$eV). The Ge s-bands are seen to be located around $E = -11$eV, and the Au d-bands are located around $E = -6$eV. However, for LaAuGe, both bands lie approximately 1eV higher in energy at $E = -10$eV(Ge s-bands) and at $E = -5$eV(Au d-bands). Additionally, for LuAuGe, the Lu f-bands are observed to coincide with the Au d-bands. The conduction band extends from about $E = -5$eV up to E_F for all the REAuGe compounds and consists of the Ge p-states. These states are nearly filled, and as a consequence a pseudo-gap appears just below E_F, which has the effect of stabilising the structures. The lowest unoccupied states are observed to belong to the RE d-bands.

The densities of state at E_F are listed for all four of the non-magnetic REAuGe compounds in table 5.4. N_F is much larger for LaAuGe (2.1eV^{-1})[1] than the other REAuGe compounds ($0.4 - 1.4\text{eV}^{-1}$). The higher value for LaAuGe is assumed to be due to the flat band lying on the Fermi level at the L-H symmetry line. This La d-band hybridises strongly with the the flat Ge p-band at $E = -1$eV. Therefore, the two bands subsequently repel each other, and in the case of LaAuGe the repulsion is smaller due to the much larger c/a ratio compared to the other three compounds.

[1] From here onwards it is taken that the DOS at E_F are quoted in units of eV^{-1} per two spin directions per formula unit.

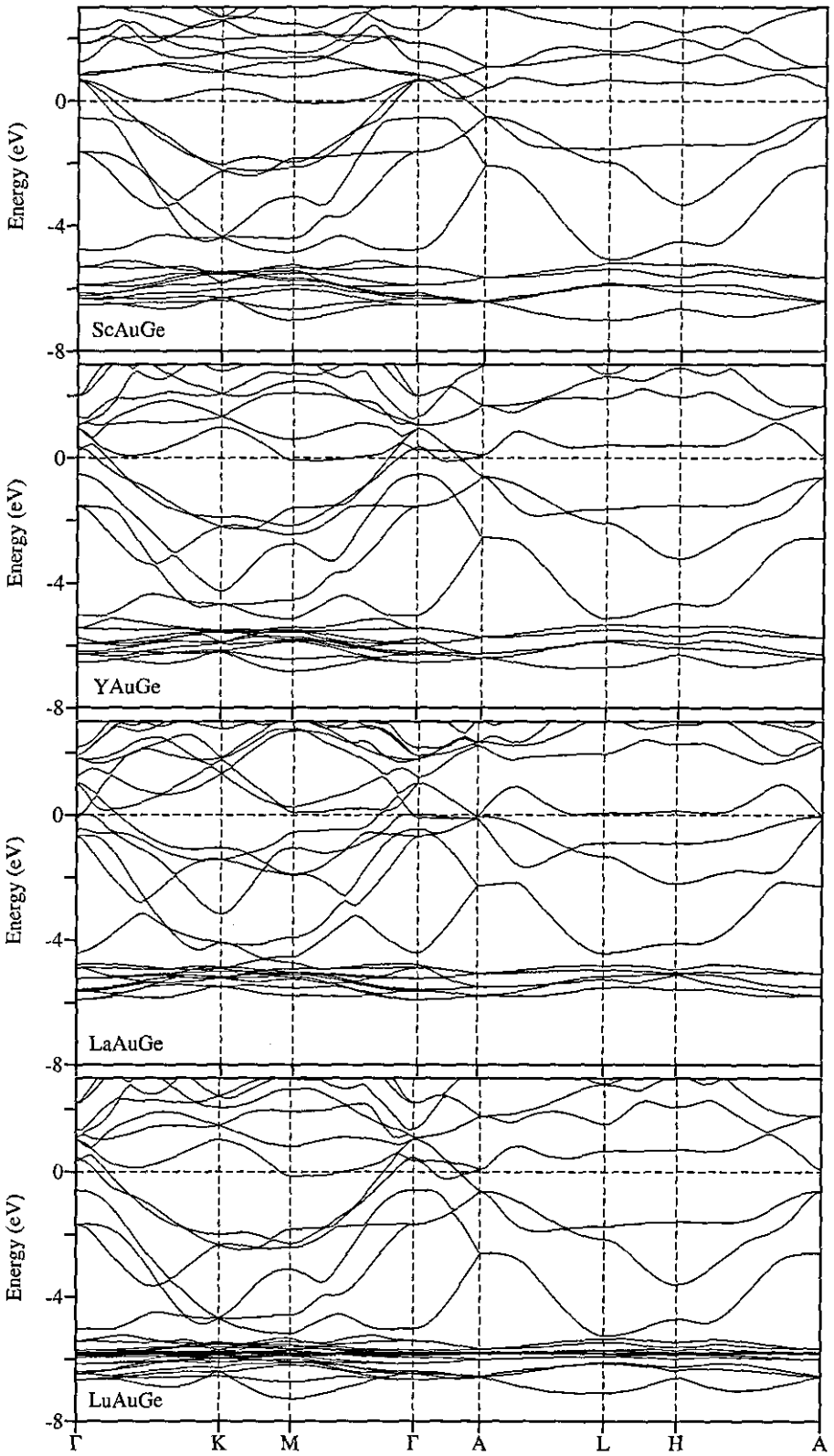

Figure 5.1: The self consistent energy band structures of ScAuGe, YAuGe, LaAuGe, and LuAuGe (top to bottom, respectively, taken from [16]) along several symmetry lines in the hexagonal Brillouin zone. The zero of energy is at the Fermi level.

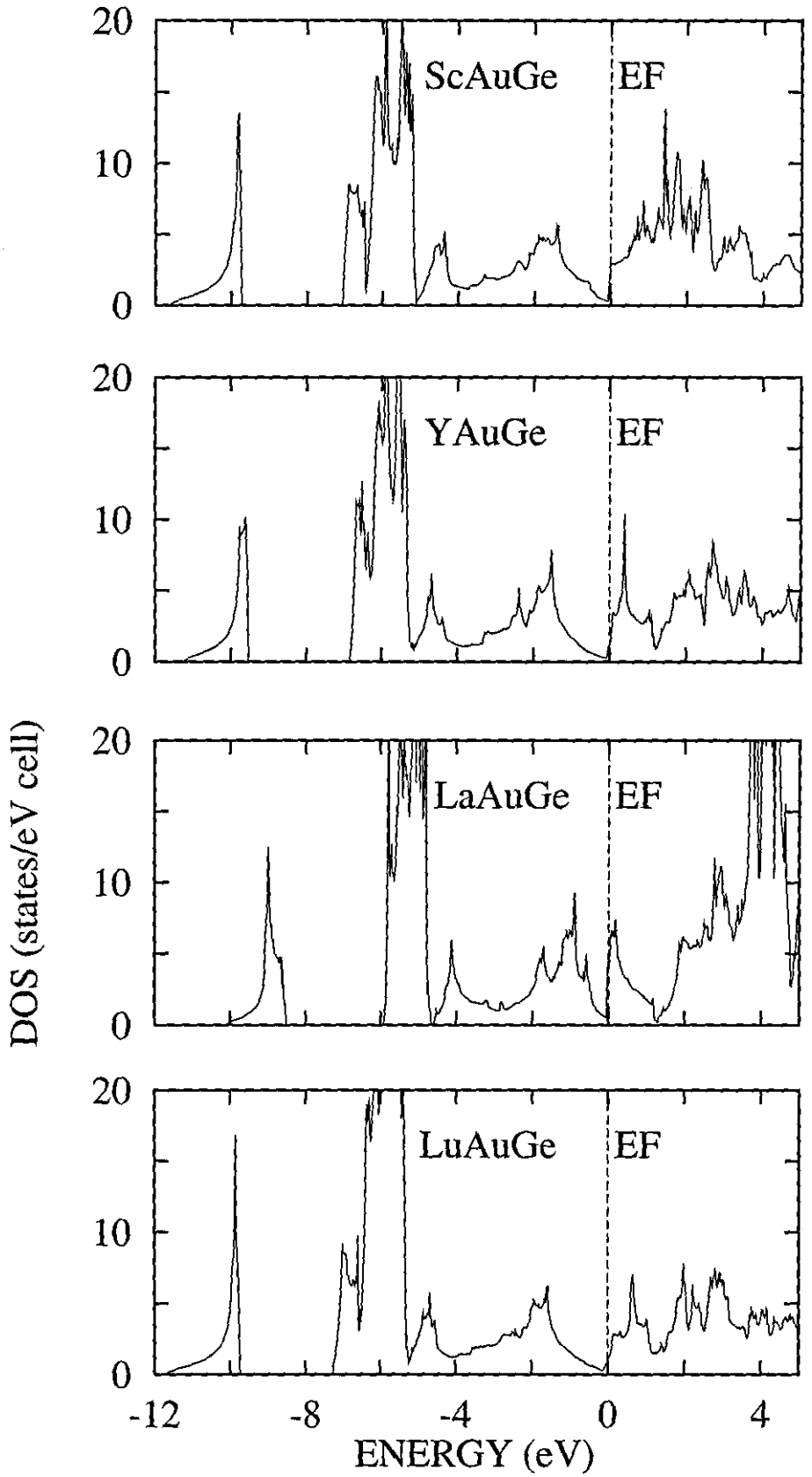

Figure 5.2: The self consistent total DOS of ScAuGe, YAuGe, LaAuGe, and LuAuGe (top to bottom, respectively) taken from [16]. The zero of energy is at the Fermi level.

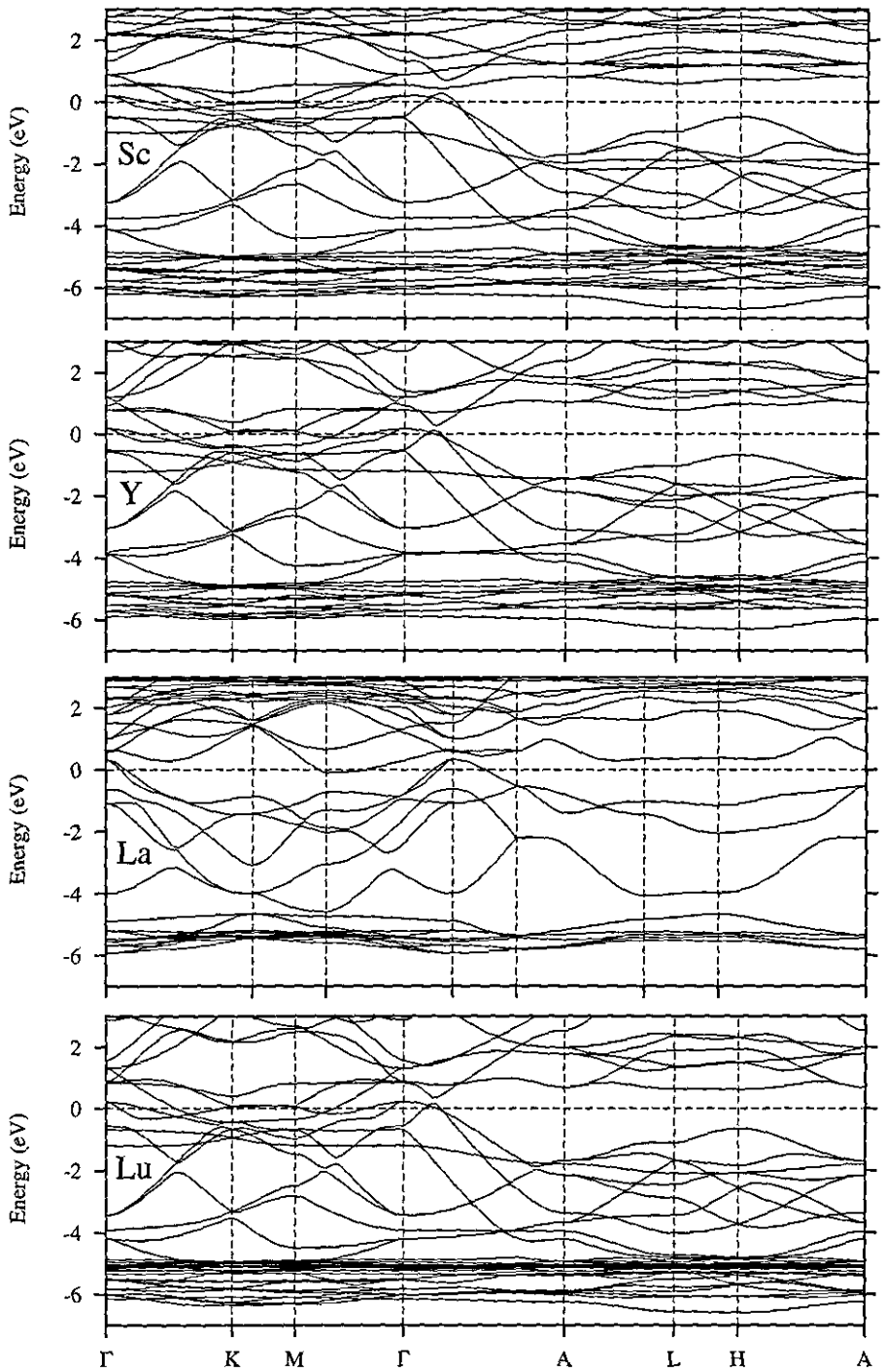

Figure 5.3: The self consistent energy band structures of ScAgGe, YAgGe, LaAgGe, and LuAgGe (top to bottom, respectively) along several symmetry lines in the hexagonal Brillouin zone. The zero of energy is at the Fermi level. Please note the different crystal structure of LaAgGe, resulting in the shifting of the symmetry directions.

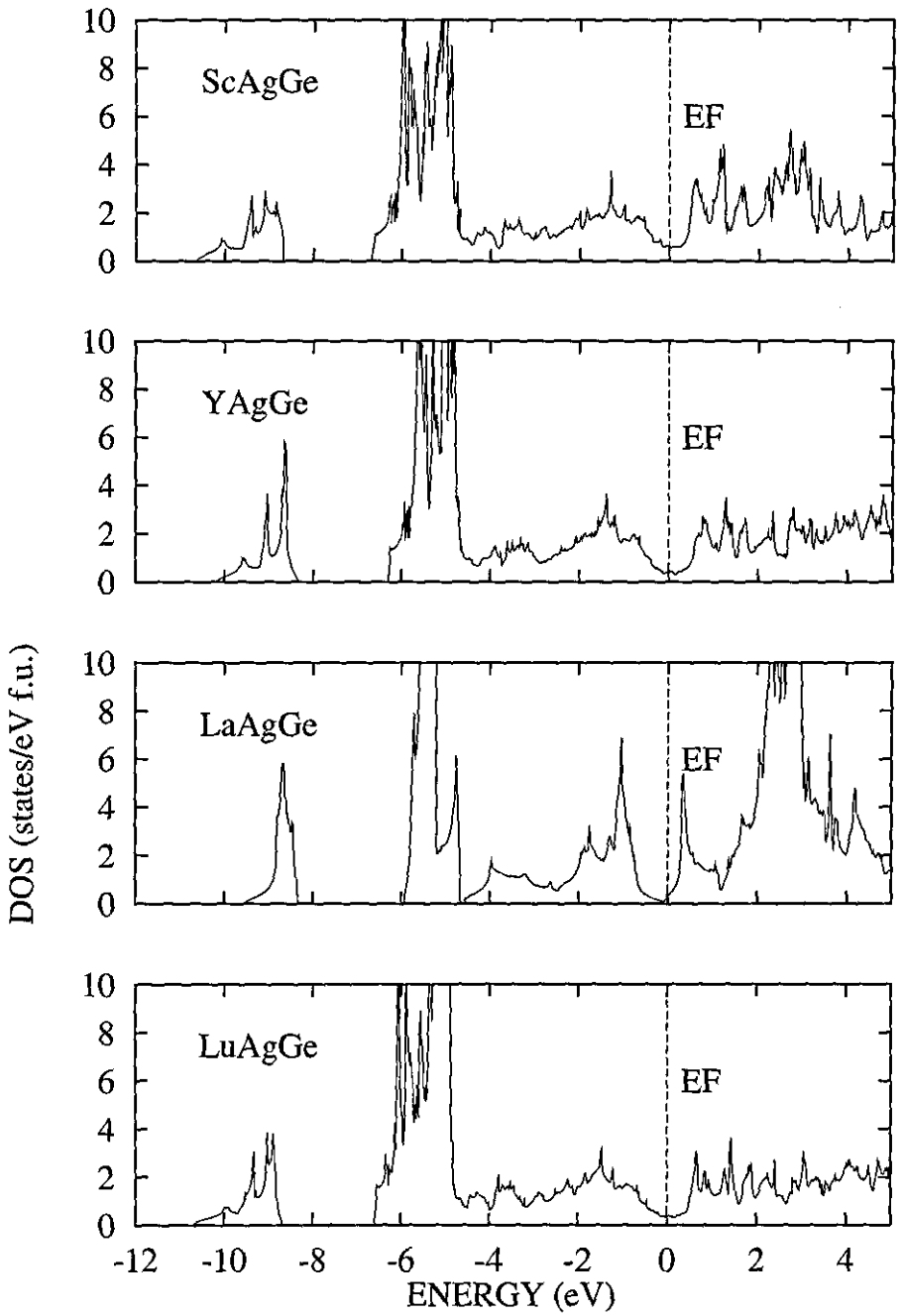

Figure 5.4: The self consistent total DOS of ScAgGe, YAgGe, LaAgGe, and LuAgGe (top to bottom, respectively). The zero of energy is at the Fermi level. The different crystal structure of LaAgGe is noted.

REAgGe

The calculated electronic structures along several lines of high symmetry within the hexagonal Brillouin zone are shown in figure 5.3 for the four compounds, ScAgGe, YAgGe, LaAgGe, and LuAgGe in comparison with the previously examined REAuGe electronic structures. The electronic structures are observed to be very similar for both the REAgGe (figure 5.3) and the REAuGe (figure 5.1) compounds, despite the differences in crystal structures.

The corresponding density of states (DOS) are shown in figure 5.4. The Ge s-bands lie at energies of $E = -11$eV for ScAgGe and LuAgGe, $E = -10$eV for YAgGe, and $E = -9.5$eV for LaAgGe. The Ag d-bands lie at $E = -7$eV for ScAgGe, YAgGe, and LuAgGe, and at $E = -6$eV for LaAgGe. The RE f-bands coincide with the Ag d-bands in all cases, and the conduction band is formed from the Ge p-states extending from $E = -5$eV up to E_F. The first unoccupied states are the RE d-bands. The band structures of the REAuGe and REAgGe are observed to be qualitatively very similar. However, the DOS at E_F is lower in the REAgGe than the REAuGe because the flat bands lie above E_F, and not along E_F as previously observed for the REAuGe compounds.

The DOS at E_F are listed in table 5.4, and range from 0.3eV^{-1} for LaAgGe and LuAgGe to 0.6eV^{-1} for ScAgGe. The flat bands along the L-H symmetry direction are much less pronounced for the REAgGe compounds than for the REAuGe compounds, although a pseudo-gap is still observed at E_F.

5.3 Resistivity

5.3.1 Experimental

The resistivity measurements are performed using a special sample holder and rod insert to the MPMS SQUID cryostat described in chapter 4, which allows electrical connection to the sample. As in the magnetisation measurements, the resistivity can be measured between $2\text{K} < T < 300\text{K}$ and in external magnetic fields up to 7T.

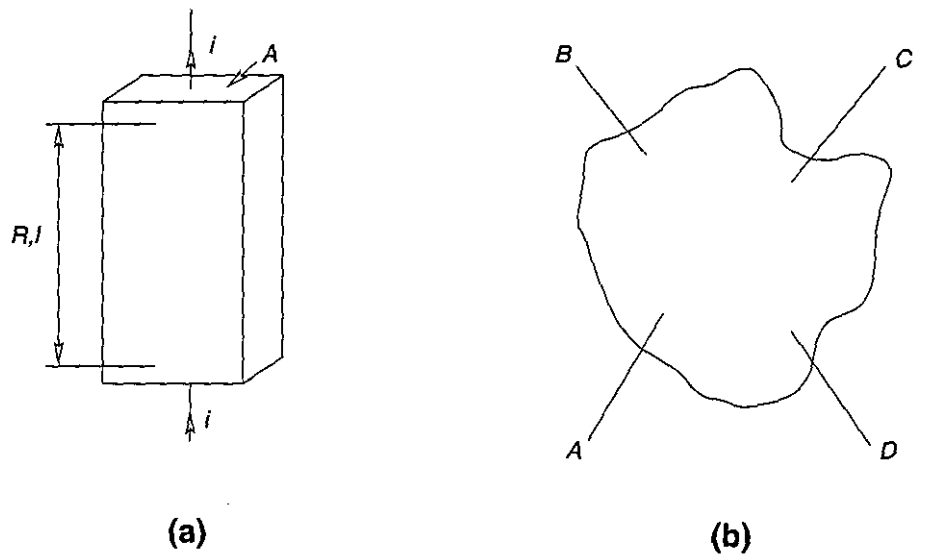

Figure 5.5: Four point contact arrangement used for the resistivity measurements.

Small polycrystalline blocks are cut from the annealed samples using a diamond saw. Typical dimensions of the blocks are 1mm x 2mm x 5mm. Four strands of gold wire are attached to the block to be measured using a silver glue. One strand is attached at each end, and two on the top surface as far apart as possible. A typical contact arrangement is depicted schematically in figure 5.5(a). A current of 10mA - 100mA is passed between the two ends of the block, and the resistance, R, between the two top contact points is measured. The resistivity is given by

$$\rho = \frac{A}{l}R \tag{5.1}$$

where A is the area of the end surfaces, and l is the distance between the two contacts across which the resistance is measured.

Alternatively, for discs which cannot be cut to the correct shape, the resistivity is instead measured using the van der Pauw method [44], in which the four contacts, A, B, C, and D, are placed at four points on the sample surface as shown in figure 5.5(b). In this case the resistivity is given by [44]

Table 5.2: Room temperature resistivities of the non-magnetic RETGe (RE=Sc,Y,La,Lu; T=Ag,Au). The top row values are taken from [16], the bottom row values from this work.

ScAuGe	YAuGe	LaAuGe	LuAuGe	ScAgGe	YAgGe	LaAgGe	LuAgGe
$63\mu\Omega cm$	$337\mu\Omega cm$	$804\mu\Omega cm$	$92\mu\Omega cm$	-	-	-	-
$46\mu\Omega cm$	$180\mu\Omega cm$	$445\mu\Omega cm$	$106\mu\Omega cm$	$48\mu\Omega cm$	$504\mu\Omega cm$	$72\mu\Omega cm$	$160\mu\Omega cm$

$$\rho = \frac{\pi d}{ln(2)} \frac{(R_{AB,CD} + R_{BC,DA})}{2} \cdot f\left(\frac{R_{AB,CD}}{R_{BC,DA}}\right) \tag{5.2}$$

where d is the disc thickness, and $f\left(\frac{R_{AB,CD}}{R_{BC,DA}}\right)$, is a geometric factor which depends only on the ratio $R_{AB,CD}/R_{BC,DA}$ and which is tabulated in [44]. $R_{\alpha,\beta,\gamma,\delta}$ is the resistance between the points, α and β when current is passed between γ and δ.

5.3.2 Results

The electrical resistivities, $\rho(T)$, of ScAuGe, YAuGe, LaAuGe, and LuAuGe are presented in figure 5.6(top). The corresponding $\rho(T)$ for ScAgGe, YAgGe, LaAgGe, and LuAgGe are shown in figure 5.6(bottom).

From figures 5.6(top) and 5.6(bottom) it is seen that the residual resistivities, ρ_0, are quite different for each compound. ρ_0 arises in the most part for polycrystalline samples such as the ones examined here from microcracks in the brittle blocks upon which the measurements are made. However, the especially large value of ρ_0 for YAgGe stands out in particular as it is about an order of magnitude greater than for the other compounds.

For the non-magnetic REAuGe and REAgGe compounds the curvatures of $\rho(T)$ are all metallic-like in appearance. For ScAuGe and LuAuGe a nearly linear dependence of $\rho(T)$ up to room temperature is observed. For all the other compounds there is a tendency towards saturation at higher temperatures.

The room temperature values of the resistivities, $\rho(300\text{K}) - \rho_0$, as derived from this study

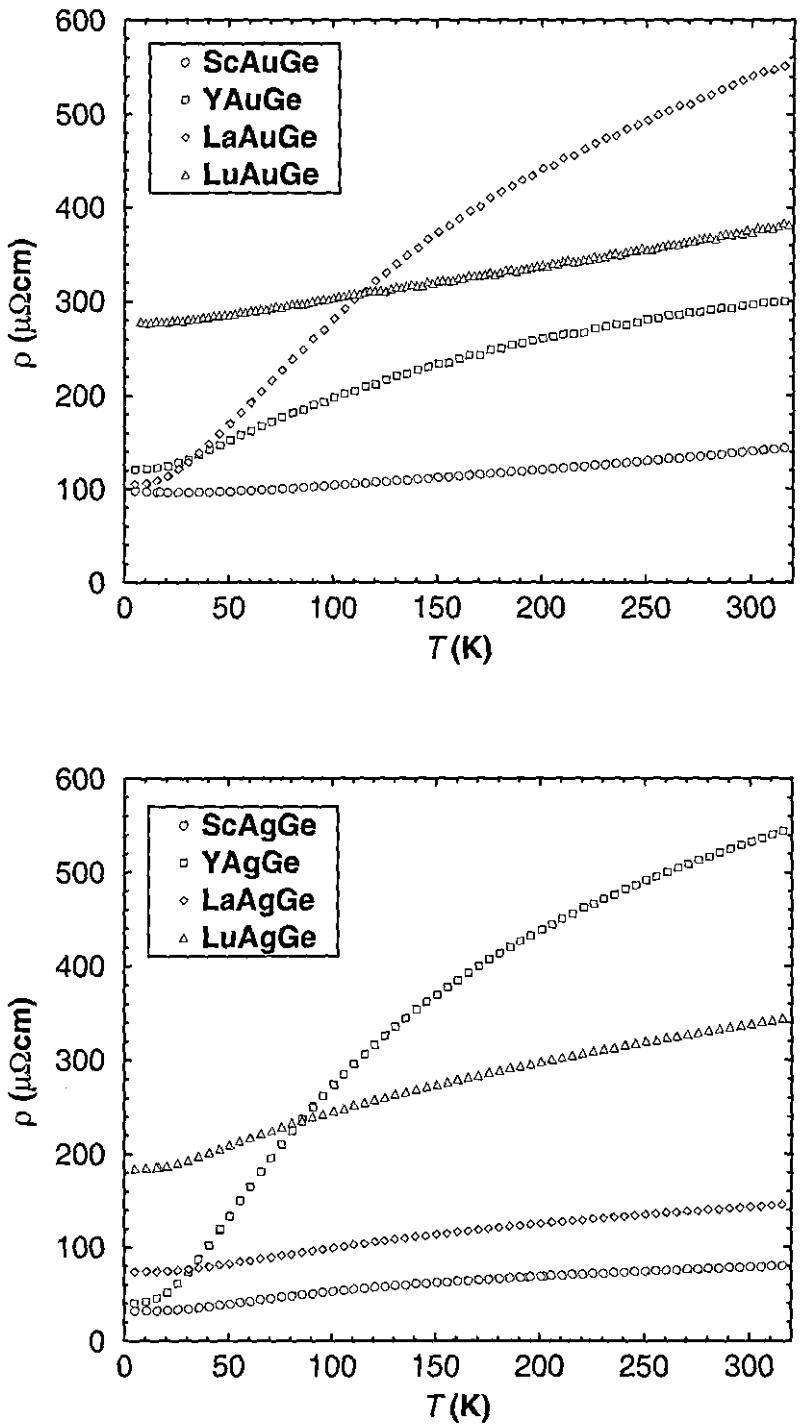

Figure 5.6: Electrical resistivities, $\rho(T)$, of small polycrystalline blocks of (top) REAuGe taken and (bottom) REAgGe. The curves shown are measured in fields of 1T, 3T, and 7T. The YAgGe resistivity is shifted by $-500\mu\Omega$cm for clarity.

are tabulated in table 5.2 together with the values for the non-magnetic REAuGe obtained by Schnelle et al. [16]. Considering first the REAuGe compounds, the values obtained from this study range from 46$\mu\Omega$cm (ScAuGe) to 445$\mu\Omega$cm (LaAuGe). These are significantly lower than obtained by Schnelle et al., but the results are qualitatively similar. In particular, LaAuGe has a value that is much higher than the other REAuGe compounds, which would hint at an additional scattering mechanism being present in the compound, e.g. a narrow band near E_F [45]. When the electronic band structure of LaAuGe is considered (figures 5.1 and 5.2) this is seen to correspond to the scattering of the Ge p-band conduction electrons into a La d-band which is flat close to E_F for a large part of the Brillouin zone.

Similar room temperature values of the resistivity are observed for the non-magnetic REAgGe compounds, ranging from 48$\mu\Omega$cm (ScAgGe) to 504$\mu\Omega$cm (YAgGe). It is interesting to note that in this case YAgGe has an exceptionally large value in comparison to the other isostructural REAgGe (RE=Sc, Lu) compounds although there is no indication from the band structure calculations (figure 5.3) for an additional electron scattering mechanism.

5.4 Specific Heat Capacity

The specific heat capacities of the non-magnetic REAuGe and REAgGe compounds are displayed in figures 5.7 and 5.8, respectively. The inserts contain the plots of c_p/T vs. T^2. The specific heat capacities of non-magnetic compounds may be analysed assuming that the total specific heat capacity is composed of several contributions

$$c_{p[tot]} = c_{p[n]} + c_{p[el]} + c_{p[latt]} \tag{5.3}$$

where $c_{p[n]}$ is the contribution to the specific heat capacity arising from the nuclei, $c_{p[el]}$ is the electronic contribution arising from the action of the conduction electrons, and $c_{p[latt]}$ is the lattice, or phonon, contribution.

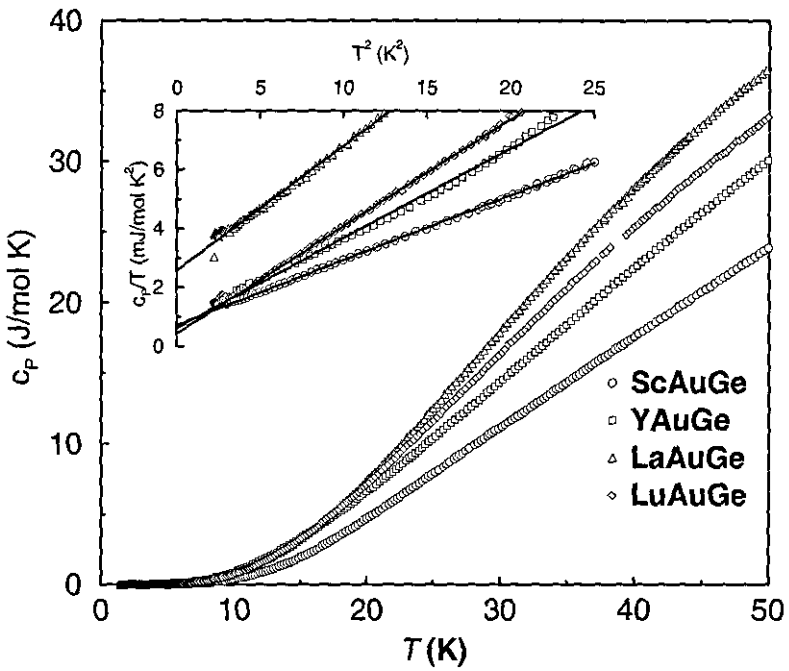

Figure 5.7: The specific heat capacities, $c_P(T)$, of the four REAuGe compounds taken from [16]. A plot of c_P/T vs. T^2 is presented in the insert for $T < 5$K. The straight lines are the least-squares fits extrapolated to $T^2 = 0$.

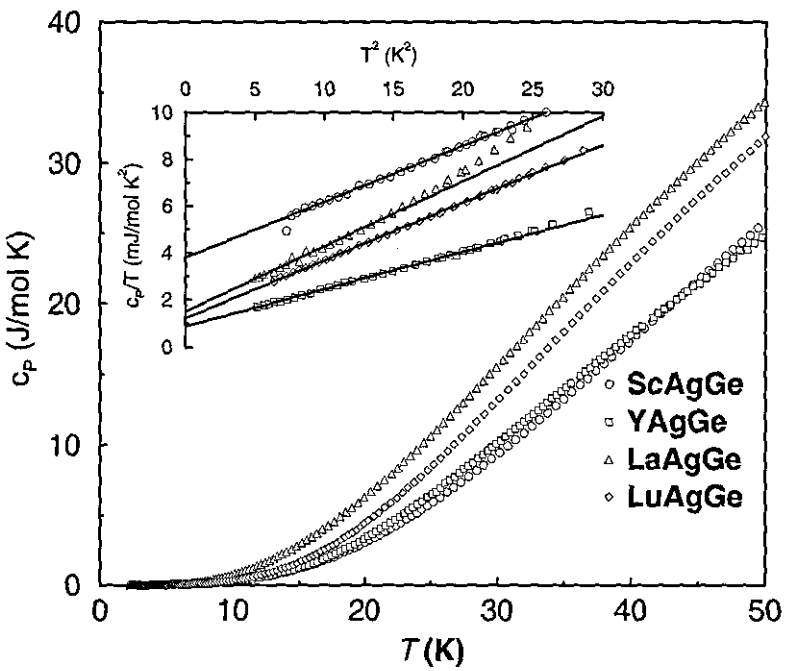

Figure 5.8: The specific heat capacities, $c_P(T)$, of the four REAgGe compounds. A plot of c_P/T vs. T^2 is presented in the insert for $T < 5$K. The straight lines are least-squares fits extrapolated to $T^2 = 0$.

As $c_{p[n]}$ only becomes significant at very low temperatures ($T < 1$K) for the compounds under consideration, it may be neglected completely. The temperature dependence of the remaining electronic and lattice contributions at low temperatures can be approximately described as the sum of the Debye T^3 model and a linear Sommerfeld term [46]

$$c_p = \gamma T + \beta T^3 \tag{5.4}$$

where

$$\gamma = \frac{1}{3}\pi^2 N(E_F) k_B^2 T \tag{5.5}$$

with $n(E_F)$ being the density of states (DOS) at the Fermi level, E_F, and k_B is the Boltzmann constant, and

$$\beta = 1944 \cdot n \left(\frac{1}{\Theta_D(0)} \right)^3 \tag{5.6}$$

where $\Theta_D(0)$ is the Debye temperature which characterises the lattice specific heat at low temperatures and n is the number of atoms in the formula unit.

The electronic contributions, γ, for the REAuGe and REAgGe compounds are obtained from fits to the low temperature specific heat ($T < 5$K). In the inserts of figures 5.7 and 5.8, for the REAuGe and REAgGe compounds respectively, the low temperature part of the specific heat capacity is displayed in a c_p/T vs. T^2 representation. The Sommerfeld coefficient, γ, is calculated from the respective intercepts of the straight line fits to the data. The values of γ for each compound are listed in table 5.4, to be compared with the results of the magnetic susceptibility measurements in the following section.

The initial Debye temperature, $\Theta_D(0)$, is determined using equations 5.5 and 5.6. The plots of c_p/T vs. T^2 shown in the inserts of figures 5.7 and 5.8 for the REAuGe and REAgGe compounds, respectively, can be fitted linearly at low temperatures. $\Theta_D(0)$ is calculated for each compound from the slope. These values are listed in table 5.3.

The initial Debye temperatures, $\Theta_D(0)$, vary from compound to compound and depend strongly upon the low frequency vibrations of the heaviest atoms in the direction of the

weakest bonding. For both types of crystal structures ($CaIn_2$ and Fe_2P) in which the REAuGe and REAgGe compounds crystallise, the weakest bonding direction should be along the c-axis, i.e. between the atomic layers. The largest $\Theta_D(0)$ occurs for ScAuGe in the REAuGe series and corresponds to Sc having the smallest mass. For the REAgGe compounds, YAgGe has the largest $\Theta_D(0)$.

The Debye temperatures, $\Theta_D(T)$, as a function of temperature are plotted in figures 5.9 and 5.10 for the REAuGe and REAgGe compounds, respectively. $\Theta_D(T)$ is calculated by iteratively solving the equation [47]

$$c_p(T) - \gamma T = n \cdot \mathcal{D}\left(\frac{\Theta_D(T)}{T}\right) \tag{5.7}$$

for the lattice specific heat capacity. $\mathcal{D}$ is the Debye function [47], and $n = 3$ for both REAuGe and REAgGe, is the number of atoms per formula unit.

For both the REAuGe and REAgGe compounds, $\Theta_D(T)$ initially decreases strongly from the initial Debye temperature, $\Theta_D(0)$. All of the compounds have a minimum in $\Theta_D(T)$ around 10-20K ($\approx \Theta_D(0)/20$) which is a frequent feature found in $\Theta_D(T)$ plots [47]. At higher temperatures $\Theta_D(T)$ increases steadily. This 'softening' and 'hardening' of $\Theta_D(T)$ is most pronounced for the lighter compounds.

The phonon behaviour of the isostructural REAuGe compounds can be determined in terms of a harmonic oscillator model [16]. In this model the lattice is treated as a harmonic oscillator with mass, M, and spring constant, D. M is representative of the average atomic mass, i.e the molar mass. In this model

$$\Theta_D\left(=\frac{\hbar\omega_D}{k_B}\right) \propto \sqrt{D/M} \tag{5.8}$$

In order to test the applicability of this model, $\Theta_D(0)$ of all the REAuGe compounds are scaled to ScAuGe by $\sqrt{D/M}$. Similarly, this model is now also tested on all of the non-magnetic REAgGe compounds. All of the REAgGe compounds are scaled to ScAgGe, bearing in mind the different structure type of LaAgGe.

In a first case, the spring constant, D, is assumed to be constant for all the compounds

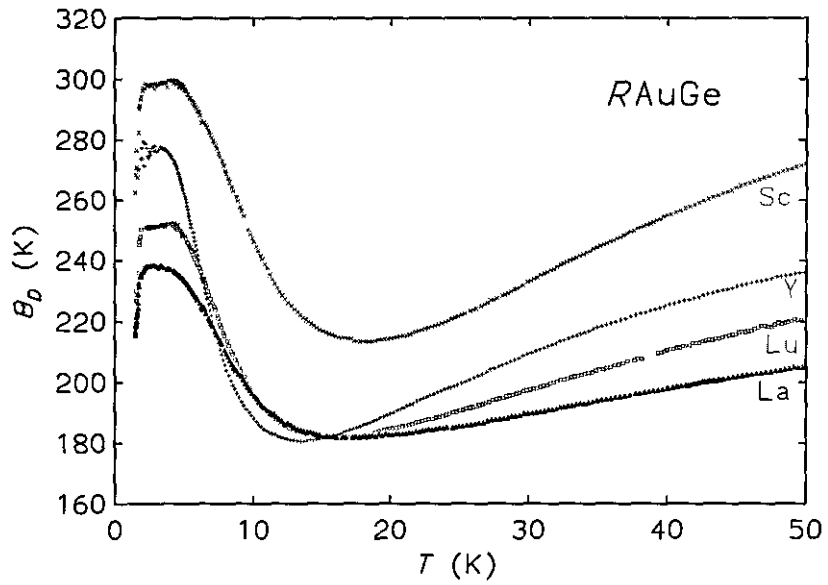

Figure 5.9: Equivalent Debye temperatures, $\Theta_D(T)$, for the specific heats of the four non-magnetic REAuGe taken from [16].

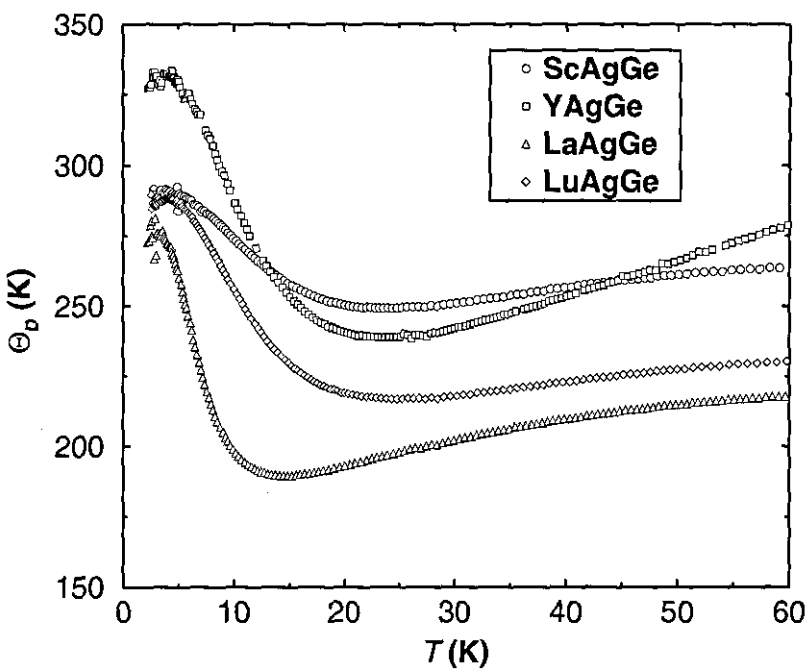

Figure 5.10: Equivalent Debye temperatures, $\Theta_D(T)$, against T for the specific heats of the four non-magnetic REAgGe.

in a given series. This corresponds to a constant strength interatomic binding force. The resulting values of

$$\Theta_D^{RE}(0) = \Theta_D^{Sc}(0)\sqrt{M^{Sc}/M^{RE}} \tag{5.9}$$

are listed in table 5.3 as the 1st scaling.

From the REAuGe compounds, the results are seen to be reasonable for YAuGe and LuAuGe. However, LaAuGe does not fit so well to this scheme, which signifies that the average binding forces in LaAuGe are weaker that in the other isostructural REAuGe compounds. The REAgGe compounds also do not fit particularly well to this model, as is observed from the calculated values of $\Theta_D(0)$(1st scaling) in table 5.3.

A second, more realistic, scaling may be applied by bearing in mind that the binding forces vary from compound to compound. This can be particularly well modelled for the REAuGe compounds by noting the small change in the [AuGe] polyanion network from a 3-dimensional cages to 2-dimensional layers (see chapter 3), and the corresponding relative lattice contraction along the c axis as shown by the changes in c/a between ScAuGe and LuAuGe. Assuming then that the binding forces vary approximately as

$$D \propto 1/c \tag{5.10}$$

the second scalings of

$$\Theta_D^{RE}(0) = \Theta_D^{Sc}(0)\sqrt{M^{Sc}c^{Sc}/M^{RE}c^{RE}} \tag{5.11}$$

which are listed in table 5.3 as the 2nd scaling, give a more reasonable value for LaAuGe, although the results for the other compounds become slightly worse.

The scaling relationship of equation 5.11 is not applicable to the REAgGe compounds as the c/a ratio of the lattice parameters remains approximately constant for all of the compounds in the series.

Table 5.3: Molar mass, M, and observed and calculated initial Debye temperatures, Θ_D for the non-magnetic REAuGe and REAgGe compounds.

Compound	M	$\Theta_D(0)$(K)		
	g/mol	observed	1st scaling	2nd scaling
ScAuGe	314.5	298.3	-	-
YAuGe	358.5	276.3	279.4	270.4
LaAuGe	408.5	237.7	261.8	239.7
LuAuGe	444.5	251.5	250.9	279.2
ScAgGe	225.4	289.6	-	-
YAgGe	269.3	330.6	264.9	-
LaAgGe	319.4	275.0	243.2	-
LuAgGe	355.4	287.4	230.6	-

5.5 Magnetic Susceptibility

The molar magnetic susceptibilities of the non-magnetic REAuGe and REAgGe (RE = Sc,Y,La,Lu) are plotted in figures 5.11 and 5.12, respectively, in the temperature range from 5K to 350K in external fields up to $H_{ext} = 4$T.[2] For all of the compounds, a Curie type of upturn is observed below $T \approx 50$K which is due to the small amounts of magnetic RE impurities that are inherent in all the compounds. The amount of magnetic impurities contained in each compound is less than 0.5%, except for LuAuGe in which they are significantly greater.

The magnetic susceptibilities can be fitted according to

$$\chi_{\mathrm{mol}} = C/T + \chi_0 + a \cdot T \tag{5.12}$$

[2]The magnetic susceptibilities of all of the non-magnetic RETGe compounds have been measured down to $T = 0.3$K using a single shot ^{3}He cryostat. Superconductivity is found in ScAgGe at $T_C = 1.1(1)$K, and this first low temperature result is examined in appendix B.

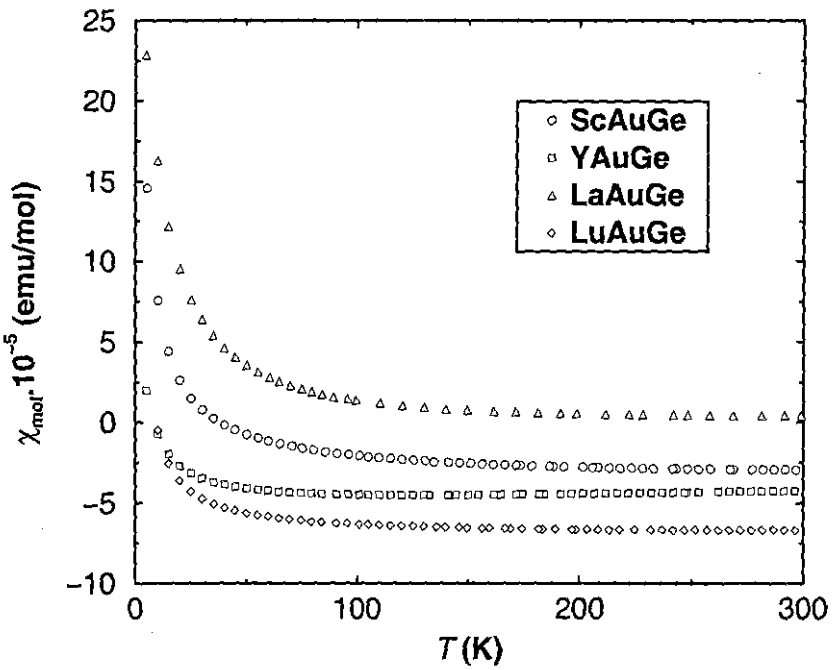

Figure 5.11: Molar magnetic susceptibilities of Sc-, Y-, La-, and LuAgGe as measured in an external field of 4T (taken from [16]).

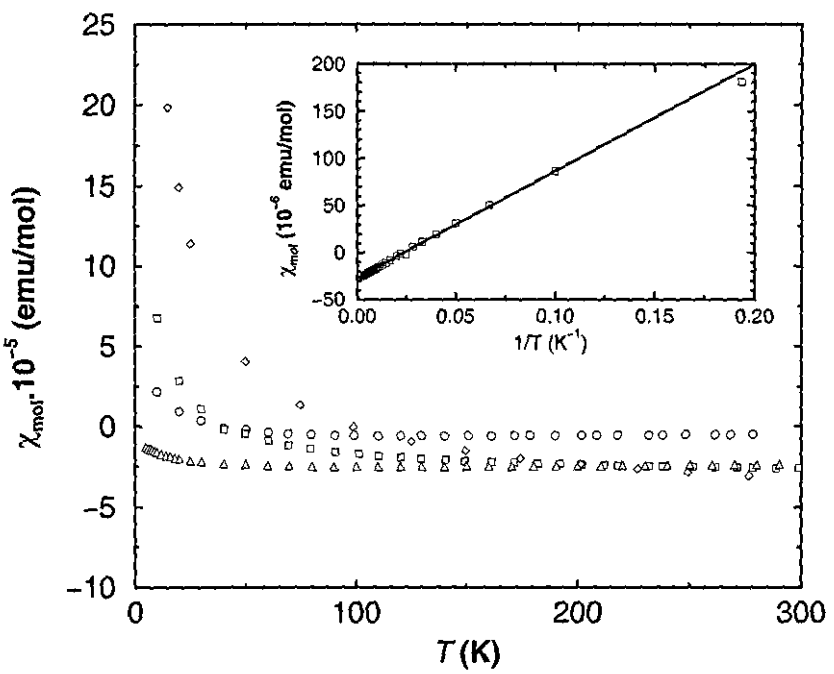

Figure 5.12: Molar magnetic susceptibilities of Sc-, Y-, La-, and LuAgGe as measured in an external field of 4T. The insert shows χ vs. $1/T$ for YAgGe. The intercept with the abscissa gives χ_0.

Table 5.4: Temperature independent part, χ_0, of the magnetic susceptibilities of the compounds RETGe (T=Ag,Au) as obtained from fits of the experimental data. The diamagnetic increments for the RE^{3+} ions, χ_{inc}^{RE} are taken from [48]. The Pauli paramagnetic susceptibility for the REAuGe is obtained according to $2/3\chi_P = \chi_0 - \chi_{inc}^{RE} - \chi_{inc}^{AuGe}$, which takes into account the Landau electron diamagnetism of $\chi_L = -1/3\chi_P$. The term χ_{inc}^{AuGe} is the extrapolated increment for the [AuGe] polyion. For the REAgGe, χ_P is simply given by $\chi_0 - \chi_{inc}^{RE3+} + \chi_{inc}^{Ag+} + \chi_{inc}^{Ge}$ [48]. The electronic densities of states, N_F at E_F are given in states eV^{-1} for two spins and one formula unit:RETGe.

	χ_0	χ_{inc}^{RE}	χ_P	γ	N_F	χ_P/γ
Compound	10^{-6} emu/mol			(mJ $mol^{-1}K^{-2}$)	(eV^{-1})	$(3(\mu_B/\pi k_B)^2)$
ScAuGe	-38(2)	-6	63(2)	0.72(1)	1.4	6.4
YAuGe	-56(1)	-12	45(3)	0.87(1)	0.6	3.8
LaAuGe	-10(2)	-20	126(4)	2.50(6)	2.1	3.7
LuAuGe	-78(1)	-17	20(3)	0.40(2)	0.4	3.6
ScAgGe	-26(2)	-6	21	3.79(3)	0.6	0.4
YAgGe	-29(2)	-12	26	0.85(1)	0.4	2.2
LaAgGe	-25(5)	-20	44	1.48(6)	0.3	2.2
LuAgGe	-35(5)	-17	24	1.24(2)	0.3	1.4

where the Curie term, C/T, arises from the magnetic impurities, χ_0 is the temperature independent part of the susceptibility, and is the sum of the closed shell and conduction electron contributions to the diamagnetic susceptibility. The $a \cdot T$ term accounts for the temperature dependence of the susceptibility. The small linear increase that is observed in each compound can be attributed to a temperature dependence of the conduction electron susceptibilities. However, the increase is strongly masked by the Curie-term which arises from the magnetic impurities.

The values of χ_0 for all the compounds are determined by plotting the magnetic susceptibil-

ity against inverse temperature, as is shown for YAgGe in figure 5.12(insert) as an example. A straight line can be fitted to the data, the intercept of which is equivalent to χ_0. The values of χ_0 are similar for both series of compounds, ranging from $-10 \cdot 10^{-6}$emu/mol for LaAuGe to $-78 \cdot 10^{-6}$emu/mol for LuAuGe. The values for each compound are listed in table 5.4.

χ_0 is composed of two contributions; a diamagnetic contribution arising from the closed shell electrons, and a term arising from the conduction electrons (the Pauli paramagnetism) according to

$$\chi_0 = \chi_{\text{dia}} + \chi_{\text{P}} \tag{5.13}$$

where it is known from theoretical considerations (see e.g. [49]) that

$$\chi_{\text{P}} = \mu_{\text{B}}^2 N(E_{\text{F}}) \tag{5.14}$$

Therefore, if the Pauli paramagnetic term can be extracted, approximate information about the electronic density of states can be obtained, and compared with the band structure and electronic specific heat capacity measurements.

In order to extract accurately the Pauli paramagnetism from χ_0, Schnelle et al. [16] calculated the diamagnetic increments [48] for the RE contribution, $\chi_{\text{inc}}^{\text{RE3+}}$, and for the polyanion complex, $\chi_{\text{inc}}^{[\text{AuGe}]}$. The value of $\chi_{\text{inc}}^{[\text{AuGe}]}$ is determined by correcting the fitted χ_0 by the RE increments, $\chi_{\text{inc}}^{\text{RE3+}}$, and plotting this against γ. In the case of the REAuGe compounds, this results in a line which can be fitted according to

$$\chi_0 - \chi_{\text{inc}}^{\text{RE3+}} = c \cdot \gamma - d \tag{5.15}$$

where $d = \chi_{\text{inc}}^{[\text{AuGe}]}$. The results are listed in table 5.4, with values of the Pauli susceptibility ranging from $\chi_{\text{P}} = 20 \cdot 10^{-6}$emu/mol for LuAuGe to $\chi_{\text{P}} = 126 \cdot 10^{-6}$emu/mol for LaAuGe. Again, the extremely large value for LaAuGe is a consequence of the highly structured density of states at the Fermi level.

For the REAgGe, the magnetic RE impurities are observed to be generally too large for

an exact determination of χ_P, so a more approximate method is used. The diamagnetic increments taken from [48] (in units of 10^{-6}emu/mol) for Sc^{3+} (-6), Y^{3+} (-12), La^{3+} (-20), Lu^{3+} (-17), Ag^{+} (-24), and Ge (-10) are assumed to be suitable for a first calculation. The sum $\chi_{inc}^{RE3+} + \chi_{inc}^{Ag+} + \chi_{inc}^{Ge}$ then approximately describes the core diamagnetism. The Pauli paramagnetic term is then calculated from equation 5.13, and the results are listed in table 5.4 together with the REAuGe results. These show values of χ_P ($21 - 44 \cdot 10^{-6}$emu/mol) which are slightly less than those of the REAuGe compounds.

The Wilson ratio, χ_P/γ, is calculated for all of the REAuGe and REAgGe compounds. According to the ideal Fermi-Sommerfeld free electron gas model [49], χ_P/γ should be unity. However, all of the compounds (except ScAgGe) take values that are markedly enhanced from unity (see table 5.4). These enhanced values could be due to exchange enhancements of the Pauli susceptibility and/or a low effective mass, leading to reduced values of γ.

5.6 Discussion

The results of resistivity, susceptibility, and specific heat capacity measurements, in conjunction with the band structure calculations reflect well the trends observed within the crystal structures (see chapter 3), especially for the REAuGe series. The gradual change in the c/a ratio from ScAuGe (1.589) to LaAuGe (1.830) reflects the gradual change from a 3-dimensional [AuGe] network in ScAuGe to decoupled and flatter [AuGe] layers in LaAuGe. This structural evolution is revealed by systematic trends in the electronic band structure, as shown by the TB-LMTO-LSA calculations. The corresponding REAgGe series (excluding LaAgGe) on the other hand have an almost constant value of $c/a = 0.59$, as is shown by the nearly identical electronic band structures.

Because of the pseudo-gap that appears in both the REAuGe and REAgGe series at E_F, $N(E_F)$ is small for all eight compounds, and this is reflected in the Pauli susceptibilities and the specific heat capacities. However, the enhancement of $N(E_F)$ due to the leading edge of the RE d bands lying on E_F in LaAuGe produces an additional electronic scattering mechanism, leading to a higher room temperature resistivity. YAgGe has a correspond-

ingly large room temperature resistivity, but this cannot be accounted for by electronic scattering from the band structure calculations. Instead, another scattering mechanism, such as phonon scattering could be responsible, and it is possible that the abnormally large initial Debye temperature, Θ_D is a reflection of this.

Additionally, the low temperature phonon properties of both the REAuGe and REAgGe series ($\Theta(T)$) are determined accurately with a view to the analysis of the specific heats of the magnetic REAuGe and REAgGe compounds, especially with a view to separating out the magnetic and CEF contributions in the specific heat capacity as, e.g., is done in chapters 4 and 6.

Chapter 6

CeAuGe and CeAgGe

6.1 Introduction

The physical properties of CeAuGe and CeAgGe are examined in this chapter in some detail, in accordance with the frequent observation of unusual magnetic effects that occur within cerium intermetallic compounds. Such phenomena generally arise from the cerium ions trying to assume the more stable electronic configuration of lanthanum. This leaves the cerium ions in the 4+ (or mixed 3+/4+) oxidation state, giving rise to hybridisation between the cerium $4f$ electrons and the surrounding conduction electrons. Unusual effects such as heavy-fermion behaviour, valence fluctuation, or the Kondo effect, are often the result [50].

Preliminary susceptibility measurements of CeAuGe and CeAgGe have been previously published by Pöttgen et al. (CeAuGe) [15] and Pecharsky et al. (CeAgGe) [12], and are shown in figure 6.1. They indicate that CeAuGe orders ferromagnetically at $\approx$ 10K, whereas CeAgGe orders antiferromagnetically at $\approx$ 5K. These results are seen to be particularly interesting for four main reasons:

- CeAuGe is one of only a small number of cerium intermetallic compounds that display ferromagnetism. Among the others are $CeRh_3B_2$ [51], $CeRu_2Ge_2$ [52], CeGaGe [53], and CeAgGa [54]. The vast majority order antiferromagnetically.

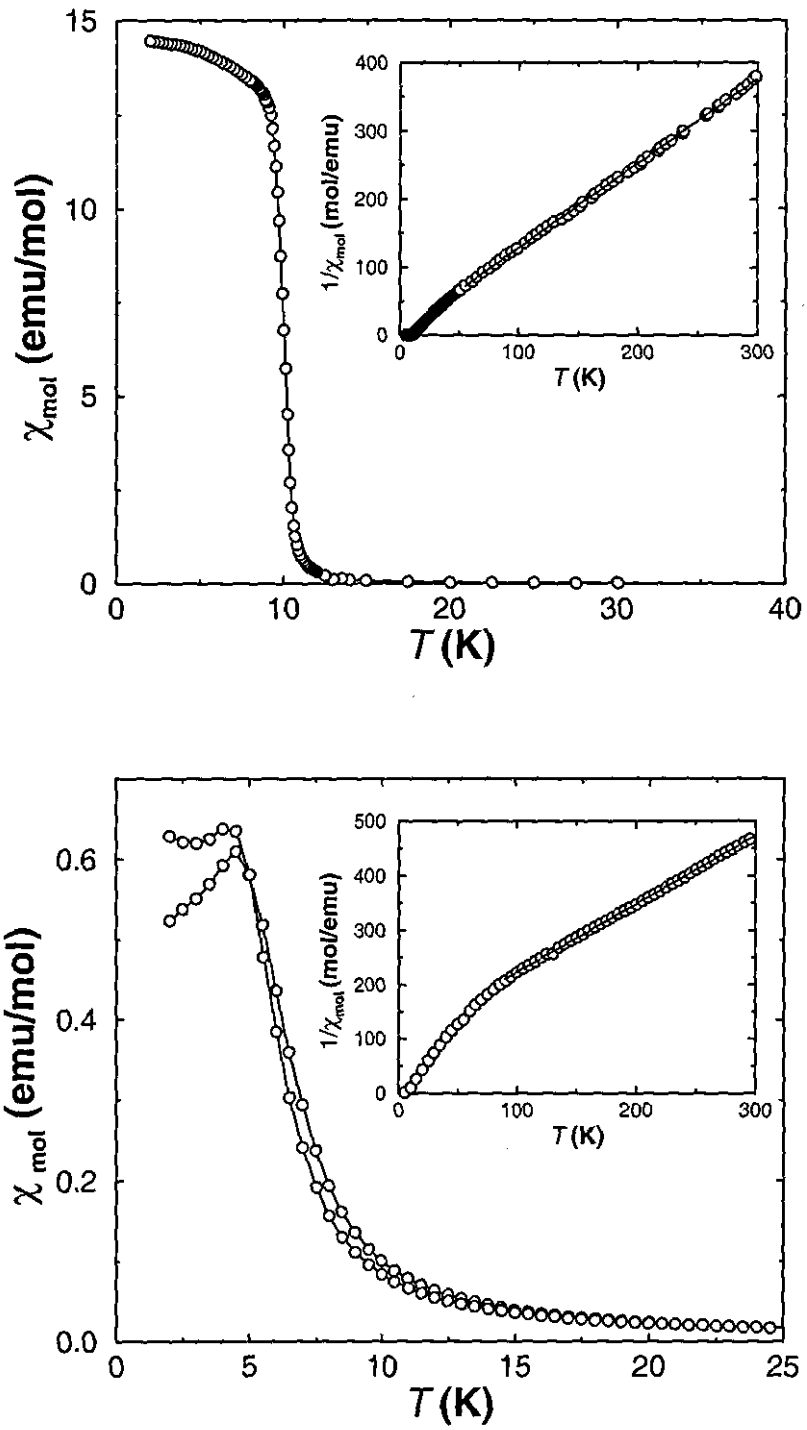

Figure 6.1: Molar susceptibility, χ_{mol}, as a function of temperature for CeAuGe [17] (top) and CeAgGe [this work] (bottom). The inserts show the inverse susceptibilities, with the high temperature data fitted to a Curie-Weiss law.

Table 6.1: Magnetic data of CeAuGe (taken from [15]) and CeAgGe (this work). μ_{sat} is the high field saturation magnetic moment, μ_{eff}^{exp} and μ_{eff} are the experimentally and theoretically determined magnetic moments, respectively. θ_P is the paramagnetic Weiss temperature, and $T_{C/N}$ is the Curie/Néel temperature of CeAuGe/CeAgGe.

	$T_{C/N}$(K)	$\mu_{sat}(\mu_B/Ce)$	$\mu_{eff}^{exp}(\mu_B)$	$\mu_{eff}(\mu_B)$	θ_P(K)
CeAuGe	10.0(2)	1.09(5)	2.55(5)	2.54	-5(1)
CeAgGe	4.9(2)	1.02(5)	2.54(4)	2.54	-82(1)

- The susceptibility curve of CeAgGe presented in figure 6.1 shows the magnetic susceptibility measured in an external field of 0.1T. Large differences are observed between the zero field cooled (z.f.c) and field cooled (f.c) curves, possibly indicating a spin glass like transition.

- CeAuGe and CeAgGe are isostructural. How does the small difference in interatomic spacing induced by the change from Au to Ag affect the magnetic structure so profoundly?

- As previously examined in chapter 4, the critical temperatures of T_C(CeAuGe) = 10K and T_N(CeAgGe) = 5K are extremely high compared to the values that may be expected according to the DeGennes scaling law with other members of the same series of REAuGe and REAgGe compounds.

The susceptibility data for both polycrystalline CeAuGe and CeAgGe are seen to fit well to the Curie-Weiss law at high temperatures (figure 6.1, inserts). In both cases the magnetic moments correspond closely to values ($\mu_{eff} = 2.54\mu_B$) expected for free cerium ions in the 3+ oxidation state. This suggests that the Ce $f-$ electrons are very well localised on the Ce atomic positions. Magnetisation measurements at $T = 5$K in CeAuGe reveal a saturation magnetisation of $1.09(5)\mu_B$/Ce atom, which is considerably reduced from the free Ce ion value of $g_J \cdot J = 2.14\mu_B$. Such reduced values are often observed for

intermetallic compounds, and are most likely due to CEF splitting effects on the J=5/2 Ce^{3+} ground state. In the case of CeAgGe, a saturation value of $1.02(5)\mu_B$/Ce atom in the $T = 2$K isotherm is obtained, which is very close to the CeAuGe value. The relevant magnetic data obtained for CeAuGe and CeAgGe are summarised in table 6.1.

In this chapter the various physical properties of CeAuGe and CeAgGe are studied further in order to investigate in more detail their magnetic properties. In particular the question of the occurrence of heavy fermion behaviour is addressed, and also the specific magnetic structures of CeAuGe and CeAgGe along with the behaviour of the magnetic ions in their local CEF environments are considered.

In section 6.2, the low temperature nuclear and magnetic structures are investigated by powder neutron diffraction. The critical behaviour of CeAuGe in the region around T_C is analysed in section 6.3. The results of specific heat capacity measurements and also of inelastic neutron scattering are compared and contrasted in sections 6.4 and 6.5, and in section 6.6, the anisotropic properties of CeAuGe are examined from susceptibility measurements performed on large single crystals. In section 7 the results of pressure studies on CeAuGe are reported. Finally, the results of this chapter are discussed and summarised in section 6.8.

6.2 Low Temperature Nuclear and Magnetic Structures

Elastic neutron scattering experiments on polycrystalline samples of CeAuGe and CeAgGe are performed with the aim of determining accurately their low temperature nuclear structures, and also their magnetic structures below $T_{C/N}$. Measurements are carried out using two of the instruments situated at the I.L.L, Grenoble; the high resolution diffractometer, D2B, and the high flux diffractometer, D20. These two diffractometers are both described in greater detail in chapter 7.

6.2.1 High Resolution Neutron Diffraction (D2B)

Experimental Conditions

The high resolution powder diffractometer, D2B, is set up using a Ge(335) monochromator having a take-off angle of 135°. This produces neutrons with a wavelength of $\lambda = 1.594$Å, and with a neutron flux at the sample of $\approx 10^6\,\mathrm{ncm}^{-2}$ [76].
Measurements are taken for both samples in the range $5° < 2\theta < 165°$ at temperatures of $T = 15$K and $T = 1.7$K for CeAuGe, and at $T = 10$K and $T = 1.7$K for CeAgGe in order to compare the neutron diffraction patterns above and below the respective magnetic ordering temperatures.

Results

Nuclear Refinements The diffraction patterns of CeAuGe (15K) and CeAgGe (10K) taken just above the magnetic ordering temperatures are presented in figures 6.2(top) and 6.2(bottom), respectively. Both diffraction patterns are refined using the Rietveld method [80] with the program *Fullprof* [79]. The crystal structure parameters obtained from single crystal X-Ray diffraction are used as starting values [14]. Both diffraction patterns refine well in correspondence to the room temperature structures, with the agreement factors being given by $R_{\mathrm{wp,CeAuGe}} = 8.99\%$ and $\chi^2_{\mathrm{CeAuGe}} = 7.01$, and $R_{\mathrm{wp,CeAgGe}} = 3.43\%$ and

$\chi^2_{\mathrm{CeAgGe}} = 1.32$, where the weighted profile, $\mathrm{R_{wp}}$ is defined as

$$R_{\mathrm{wp}} = 100 \left(\frac{S_{\mathrm{iw}} |y_{\mathrm{oi}} - y_{\mathrm{ci}}|^2}{S_{\mathrm{iw}} |y_{\mathrm{oi}}|^2} \right)^{1/2} \tag{6.1}$$

and where S_{iw} is the weighted standard deviation at i, which is defined as $S_{\mathrm{iw}} = 1/y_{\mathrm{oi}}$. y_{oi} and y_{oc} are the observed and calculated intensities, respectively, at position i in 2θ, and the goodness of fit parameter, χ^2, is defined as

$$\chi^2 = \left(\frac{R_{\mathrm{wp}}}{R_{\mathrm{exp}}} \right)^2 \tag{6.2}$$

where R_{exp} is the expected profile R-value as calculated from the number of (a)degrees of freedom and (b)refined and (c)fixed parameters [79].

It is therefore evident from the quality of the refinement, and its agreement to the room temperature structure that no structural phase changes occur towards lower temperatures. In addition, no un-indexed Bragg reflection are observed, indicating that the samples are single phased.

However, a small reduction in the unit cell volume is observed between room temperature and 15K(10K). The main contraction occurs along the c-axis, which results in an increase in the puckering of the $[\mathrm{Au(Ag)Ge}]_{\mathrm{x}}$ polyanion layers. e.g. for CeAuGe $a = 4.460$Å and $c = 7.936$Å at $T = 293$K compared to $a = 4.457$Å and $c = 7.849$Å at $T = 15$K.

Magnetic Structure Refinements Below the magnetic ordering temperatures additional coherent scattering occurs which arises from the magnetic superstructure. In the case of ferromagnetic CeAuGe, the magnetic unit cell is constrained to be equivalent to the nuclear unit cell, and the magnetic Bragg peaks will be superimposed on the nuclear Bragg peaks. For CeAgGe, which orders antiferromagnetically, additional magnetic Bragg scattering will occur at 2θ values corresponding to the (larger) magnetic unit cell.

Diffraction patterns are recorded at the lowest obtainable temperature of $T = 1.7$K for both CeAuGe and CeAgGe under identical conditions as the 15K (10K) data, i.e. the same total neutron count at the sample. The nuclear contributions to the diffraction patterns

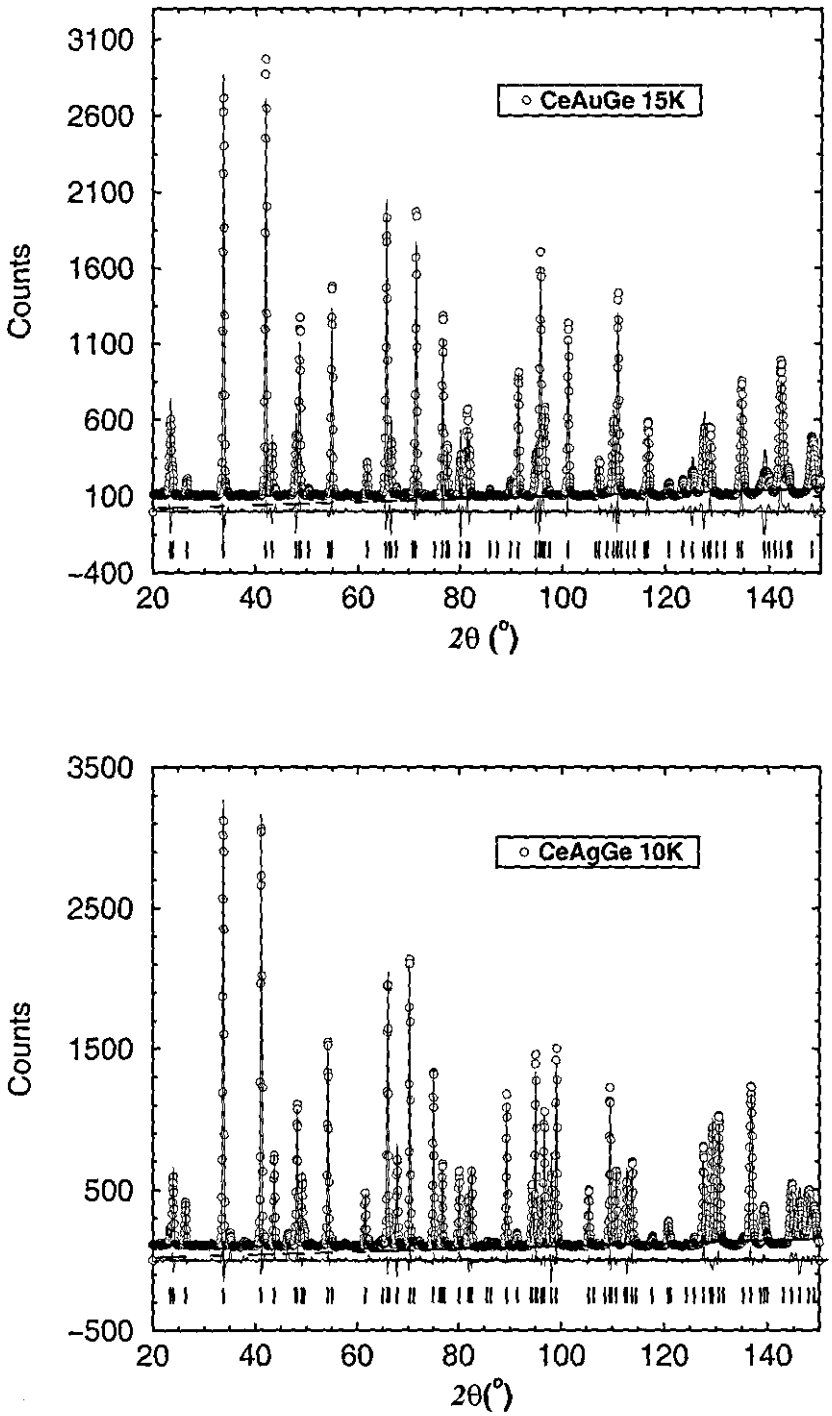

Figure 6.2: Diffraction patterns of CeAuGe (top) and CeAgGe (bottom) taken on the high resolution diffractometer D2B. The measured data are represented by open circles, and the Rietveld fits by the full lines. The difference patterns, and peak positions (vertical lines) are also given.

Table 6.2: Atomic coordinates and isotropic displacement parameters (pm^2) for CeAuGe and CeAgGe. U_{eq} is defined as one third of the trace of the orthogonalised U_{ij} tensor.

atom	Wyck. site	x	y	z	U_{eq} (pm^2)	atom	Wyck. site	x	y	z	U_{eq} (pm^2)
X-Ray single crystal data at 293K						*X-Ray powder data at 293K*					
Ce	2a	0	0	0.9842	70	Ce	2a	0	0	0.9948	60
Au	2b	1/3	2/3	0.2500[b]	93	Ag	2b	1/3	2/3	0.2500[b]	60
Ge	2b	1/3	2/3	0.7489	68	Ge	2b	1/3	2/3	0.6995	60
neutron powder data at 15K						*neutron powder data at 10K*					
Ce	2a	0	0	0.9781	60	Ce	2a	0	0	0.9516	60
Au	2b	1/3	2/3	0.2500[b]	60	Ag	2b	1/3	2/3	0.2500[b]	60
Ge	2b	1/3	2/3	0.7060	60	Ge	2b	1/3	2/3	0.6938	60

[b] Fixed parameter

are refined in the same manner as for the 15K (10K) patterns and are observed to be nearly identical, with only slight changes in the lattice parameters. However, no magnetic contributions to the diffraction patterns can be directly observed for either compound. The magnetic reflections are assumed to be too small to be directly visible in comparison to the nuclear reflections. This is due to the very small magnetic moment at the Ce^{3+} ions sites.

Magnetic peaks may be observed in the case of CeAuGe by suitable subtraction of the nuclear peaks from the 1.7K diffraction pattern using the 15K pattern. A Fortran program is used for this purpose which correctly scales the two diffraction patterns, and which also takes into account a slight 2θ offset of 0.02° due to the change in lattice parameters between the two temperatures and any small instrumental misalignments. The resulting difference pattern contains purely magnetic peaks, and is shown in figure 6.3.

A total of eight magnetic peaks at low angles can be identified to be sufficiently intense to be eligible for refinement. The two peaks positioned at $2\theta \approx 42°$ and $2\theta \approx 66°$ are not included due to the equally large negative intensities at the same positions, indicating that

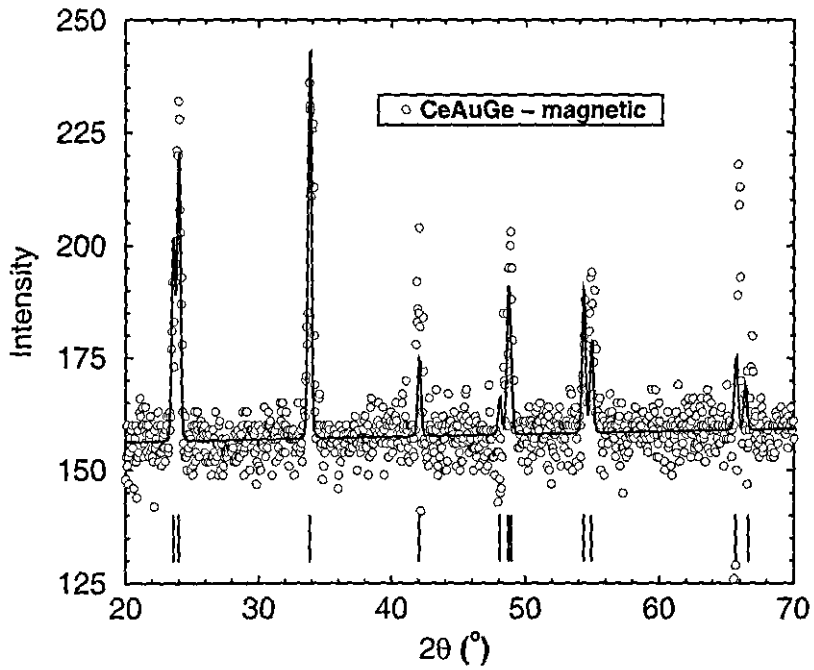

Figure 6.3: Difference pattern of CeAuGe D2B data (1.7K - 15K). The difference pattern is represented by open circles, and the Rietveld fit by the full line. The magnetic peak positions are shown by vertical lines.

the 2θ-correction in the subtraction procedure is not perfect. The largest magnetic peak is approximately 10 times smaller than the corresponding nuclear peak. For CeAgGe, no clear magnetic reflections could be found above the level of the background noise.

The magnetic reflections are seen to be too small for a full refinement to be made. Therefore the structural refinement details are constrained to those acquired at 15K, with only the magnitude and orientation of the magnetic moments allowed to refine. The best refinement corresponds to a total Ce magnetic moment of $\mu_{Ce} = 1.1\mu_B$, lying approximately along the a-axis, with $R_{mag} \approx 30\%$. This is in good agreement with the Ce saturation moment observed previously from the susceptibility measurements.

6.2.2 High Flux Neutron Diffraction (D20)

Experimental Conditions

CeAgGe is additionally measured on the high flux, medium resolution neutron diffractometer, D20, as a consequence of the lack of information gained about its magnetic structure from the previous experiments on D2B.

The high flux two axis diffractometer, D20, is for this experiment set up to produce maximum neutron flux at the sample. A pyrolytic graphite (HOPG) monochromator with a take-off angle of 42° is utilised. This produces a neutron wavelength of $\lambda = 2.411$Å, and a maximum flux of $6 \cdot 10^7\,\mathrm{ncm}^{-2}$, which is approximately an order of magnitude greater than D2B [78]. Additionally, the new ^{3}He micro-strip gas detector offers a significantly improved counting efficiency. Measurements are taken for CeAgGe at $T = 15$K and $T = 1.7$K in the range $0° < 2\theta < 150°$.

Results

Nuclear Structure The nuclear structure of CeAgGe is already determined at low temperatures from the refinement of the data from the high resolution diffractometer, D2B, and the same sample is used for the D20 diffraction experiment as the previous D2B experiment. The fitted diffraction pattern obtained on D20 at a temperature of $T = 15$K is shown in figure 6.4(top). Identical structural parameters are used as for D2B with only the line shape being refined. Due to the higher flux of this instrument, four very small impurity Bragg peaks become visible at $2\theta = 32.8°$, 54.3°, 65.9°, and 73.2°, which are not resolved in the D2B patterns.

Magnetic Structure In the diffraction pattern recorded at $T = 1.7$K, several very small commensurate Bragg peaks are observed at low angles, which are attributed to the magnetic superstructure. In order to examine these peaks more closely the nuclear peaks are subtracted from the $T = 1.7$K diffraction pattern using the $T = 15$K pattern, in the manner performed prior to the D2B CeAuGe magnetic refinement. The difference pattern

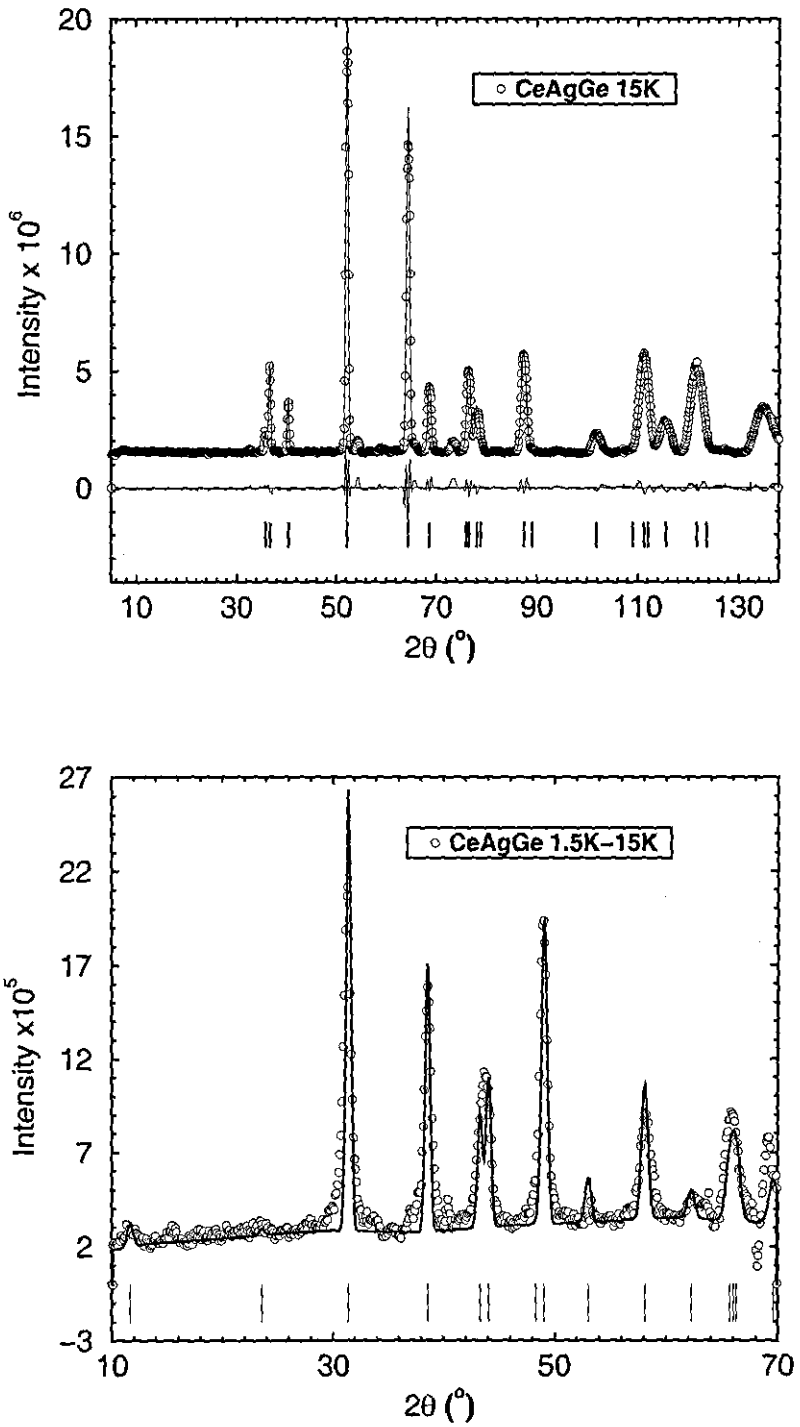

Figure 6.4: Diffraction pattern of CeAgGe at $T = 15$K recorded using the high flux powder neutron diffractometer, D20 (top). Difference pattern between $T = 15$K and $T = 1.7$K diffraction patterns (bottom). Open circles represent the experimental data, and the full lines the fits obtained from Rietveld refinement. The peak positions are shown by vertical lines.

is displayed in figure 6.4(bottom). Several distinct magnetic Bragg peaks are observed which do not correspond to the nuclear reflections indicating a true antiferromagnetic structure.

The magnetic peaks can be indexed on the basis of a $\tau = [1/3, 0, 0]$ propagation vector, which is determined by trial and error. This indicates that the Ce magnetic moments couple ferromagnetically along the *b*- and *c*-axes, and are either amplitude or phase modulated along the *a*-axis. An analysis using the method of representations [81] (see Appendix C for an example of this method) reveals that only the identity operator of the crystallographic space group $P6_3mc$ is consistent with the propagation vector, so no special symmetry considerations may be taken into account.

The magnetic moment of the Ce atoms are refined using the lattice parameters, atomic positions, and peak line shapes calculated from the nuclear structure at $T = 1.7$K in conjunction with the propagation vector, $\tau = [1/3, 0, 0]$. The magnetic moments along each crystallographic axis are allowed to refine freely, and converge to a value with the magnetic moment lying entirely in the *ab*-plane, with $\mu_{\mathrm{CeAgGe,x}} = 1.8\mu_{\mathrm{B}}$ and $\mu_{\mathrm{CeAgGe,y}} = 0.7\mu_{\mathrm{B}}$. The resultant total magnetic moment is $\mu_{\mathrm{CeAgGe}} = 1.57\mu_{\mathrm{B}}$, which is somewhat larger than the the saturation magnetic moment of $\mu_{\mathrm{sat}}(\mathrm{CeAgGe}) = 1.02(5)\mu_{\mathrm{B}}/\mathrm{Ce}$ obtained from magnetisation measurements.

6.3 Critical Behaviour of the Ferromagnetic Phase Transition in CeAuGe

6.3.1 Introduction

The analysis of the critical field behaviour of the ferromagnetic phase transition in CeAuGe described in this section is performed in order to examine in depth its behaviour within the critical regime close to the transition temperature. The analysis consists of several different methods of graphically plotting the magnetisation curves around the critical regime. The analysis provides firstly a very accurate measure of the transition temperature, T_C, and proves whether a second order transition from the ferro- to the paramagnetic state takes place. More importantly, the information gained from the analysis can be compared to the various theoretical models, in this case the 3D-Heisenberg [55] and 3D-Ising [56] models, and to gauge the strength of the magnetic anisotropy present within the compound.
The critical regime is classically defined as the region where $t \to 0$, with $t = T/T_C - 1$. Within this region, four power laws describe the temperature dependence of the spontaneous polarisation, J_S, the zero field susceptibility, $\chi(T)$, both above and below T_C, and the field dependence of the polarisation, $J(\mu_0 H, T = T_C)$, respectively:

$$J_S = J_0(-t)^{\beta} \qquad (t \to 0, t \leq 0, \mu_0 H = 0) \tag{6.3}$$

$$\chi \approx (-t)^{-\gamma'} \qquad (t \to 0, t \leq 0, \mu_0 H = 0) \tag{6.4}$$

$$\chi = \left(\frac{h_0}{J_0}\right) t^{-\gamma} \qquad (t \to 0, t \geq 0, \mu_0 H = 0) \tag{6.5}$$

$$J = D(\mu_0 H)^{1/\delta} \qquad (t = 0) \tag{6.6}$$

The pre-factors, J_0, h_0/J_0, and D, are denoted as critical amplitudes [57, 59]. It is noted that the critical exponents, β, γ, γ', and δ, and also the critical amplitudes, J_0,

h_0/J_0, and D, are universal quantities, and that the power laws are only valid within the critical regime, $T \approx T_C$.

The critical exponents are related by scaling laws. Of relevance for magnetic phase changes is the scaling law [60]:

$$\gamma = \gamma' = \beta(\delta - 1) \tag{6.7}$$

Therefore, only two of the exponents are independent. Equation 6.7 may then be used to check the values determined by the various methods.

The critical exponents expected according to the 3D-Heisenberg model (n=3), and the 3D-Ising model (n=1) are calculated to contrast them with the experimentally determined values. These are listed later in this section in table 6.3, together with the experimentally determined results. Both models assume that the exchange coupling of the magnetic moments are of short range order.

6.3.2 Experimental

All measurements are performed on the same polycrystalline sample of CeAuGe (m = 332.37mg) using the MPMS SQUID magnetometer described previously in chapter 4, and in external magnetic fields up to $\mu_0 H_{\text{ext}} = 1$T. The internal field is determined by subtracting the demagnetising field from the external field. Measurements are made in the range of 1.5K to 40K. Since the ferromagnetic transition in CeAuGe occurs at $T_C \approx 10$K the critical regime extends from approximately 9.5K $< T <$ 10.5K. This is an extremely small temperature interval and requires isotherms to be measured around T_C at intervals of $\Delta T \approx 0.05$K, which requires both very good instrument temperature stability and accuracy.

6.3.3 Results

The starting point for the analysis of the critical behaviour of CeAuGe is the measurement of the magnetisation isotherms, as shown in figure 6.5 taken from 1.5K to 40K at various

temperatures. From these basic measurements, the various types of analyses described in the following sections are performed.

Modified Arrott plots

The modified Arrott plot is a well established method of determining both the critical temperature, T_C, and the critical exponents, β, γ, and γ'. This determination is based upon the Arrott-Noakes equation of state [61]

$$\left(\frac{\mu_0 H}{J}\right)^{1/\gamma} = \frac{T - T_C}{T_1} + \left(\frac{J}{J_1}\right)^{1/\beta} \tag{6.8}$$

where T_1 and J_1 are material constants. In order to extract the exponent values, the data are plotted as $J^{1/\beta}$ versus $(\mu_0 H/J)^{1/\gamma}$, as is shown in figure 6.6 for several isotherms close to T_C. The exponents are chosen in such a manner that the isotherms near the critical isotherm exhibit linear behaviour. Deviation from linearity is observed at low fields, and is seen to be temperature dependent, as has been observed previously in several other materials [62, 63]. By extrapolating from the linear region, the determination of the critical isotherm, $(T = T_C)$, is possible, and is seen to be the one passing through the origin. From figure 6.6, it is observed that T_C corresponds to the $T = 9.72$K isotherm.

Kouvel-Fisher plots

The spontaneous polarisation, J_S, and the susceptibility, χ, cannot be determined from figure 6.5 by direct methods because they are both zero field quantities $(H \to 0)$. However, both values, J_S and χ, may be extracted from the modified Arrott plot in figure 6.6.
The spontaneous polarisation, J_S, for $T < T_C$ is determined from the intercept of the extrapolated isotherms with the $J^{1/\beta}$-axis, and the zero field inverse susceptibility, χ^{-1}, for $T > T_C$ from the interception with the $(\mu_0 H/J)^{1/\gamma}$-axis. The values obtained in this way are shown in figures 6.7(top) and 6.7(bottom), respectively. Based upon the course of $J_S(T)$ and $\chi^{-1}(T)$, the method of Kouvel and Fisher [64] is applied for the extraction of the critical values of β and γ. This method works as follows: A cubic spline is first fitted to

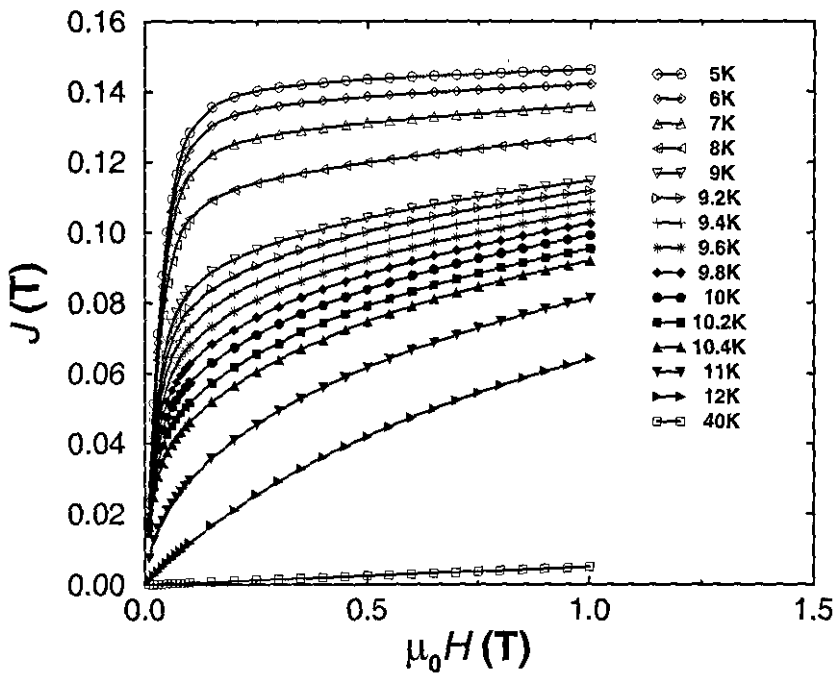

Figure 6.5: Polarisation curves, J_S, measured at selected temperatures between 1.5K and 40K (data collection courtesy of R. Reisser).

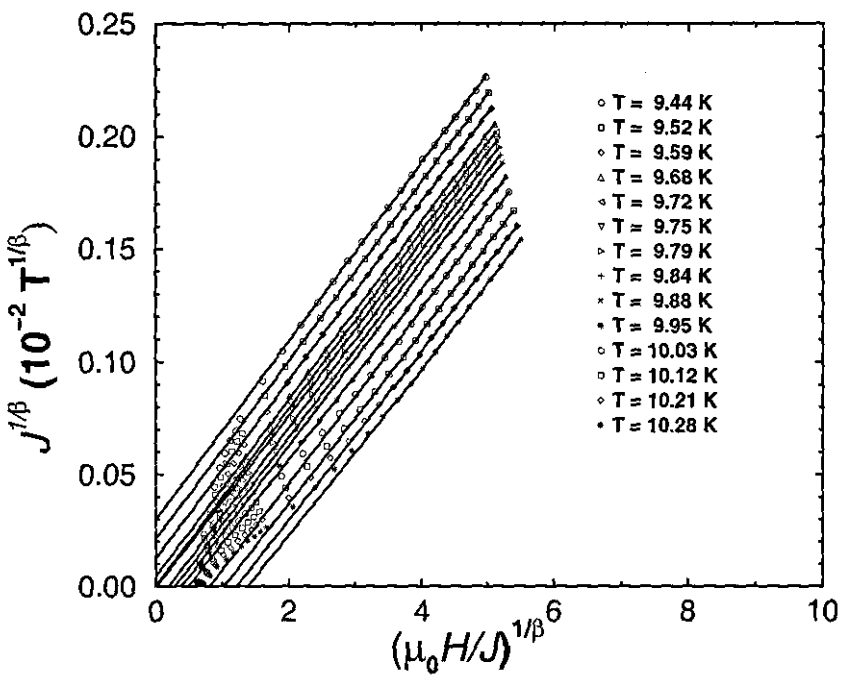

Figure 6.6: Modified Arrott plot for isotherms in the critical regime.

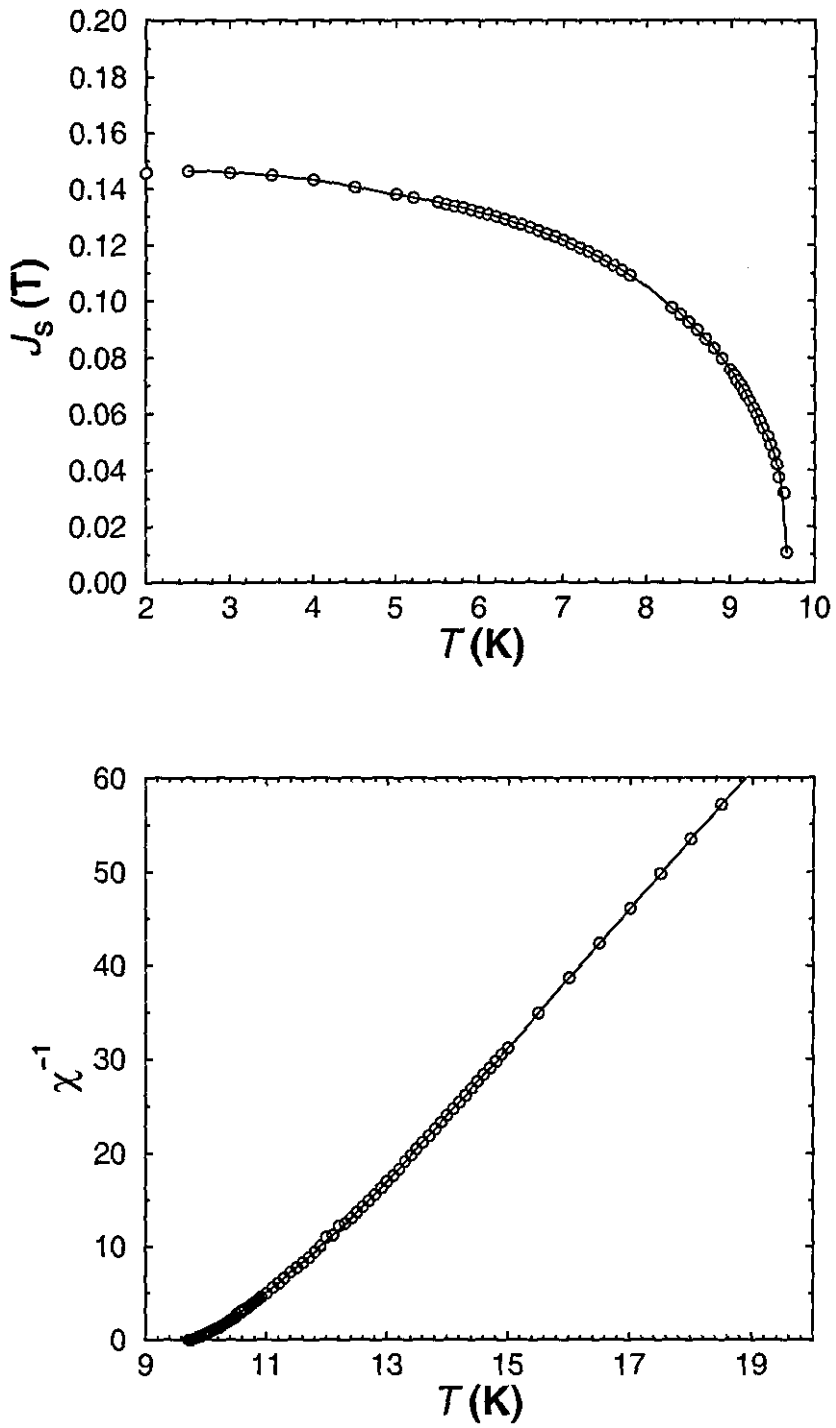

Figure 6.7: Temperature dependence of the spontaneous polarisation, J_S, and the inverse zero field susceptibility, χ^{-1}. The full lines show the fits of the power laws, $J = J_0(-t)^{\beta}$ and $\chi^{-1} = (h_0/J_0)t^{\gamma}$, respectively.

both sets of data, shown by the full lines in figures 6.7(top + bottom). Theses fits are then used to calculate numerically the quantities $(J_S dJ_S^{-1}/dT)^{-1}$ and $(\chi d\chi^{-1}/dT)^{-1}$. Plotting these quantities as a function of the temperature yields a straight line for $T \rightarrow T_C$ in both cases as is shown in figures 6.8(top) and 6.8(bottom), respectively. In these so called Kouvel-Fisher plots the inverse slope of the linear regression to the fitted data produces the critical exponents, $\beta = 0.369$ and $\gamma = 1.386$. In this graph, the onset of deviation from linearity marks the end of the asymtopic critical regime, and, in addition, the intercept with the T-axis yields the critical temperature, $T_C = 9.73(2)$K.

Determination of the critical exponent δ

The critical exponent, δ, is determined using equation 6.6, which describes the field dependence of the critical isotherm, $T = T_C$. The data within the critical regime is represented by a $ln(J)$ vs. $ln(\mu_0 H)$ plot, as shown in figure 6.9. The critical isotherm is then defined as the curve having the smallest deviance from linearity at high fields. The fits, together with equation 6.6, produce a value of $\delta = 4.80(10)$.

Scaling plots

As a further independent method for the determination of both the critical temperature, T_C, and the critical exponents, β, γ, and γ', the reduced equation of state is considered in the form

$$\frac{J}{|t|^{\beta}} = f_{\pm}\left(\frac{\mu_0 H}{|t|^{\beta\delta}}\right) \tag{6.9}$$

and using equation 6.7

$$\frac{J}{|t|^{\beta}} = f_{\pm}\left(\frac{\mu_0 H}{|t|^{\beta+\gamma}}\right) \tag{6.10}$$

where f is a scaling function and the $\pm$ sign denotes the ferromagnetic and paramagnetic regimes, respectively. When the data are plotted in the form $ln(J/|t|^{\beta})$ versus $ln(\mu_0 H/|t|^{\beta+\gamma})$, it is found that if the correct numerical values are chosen for β, γ, and T_C,

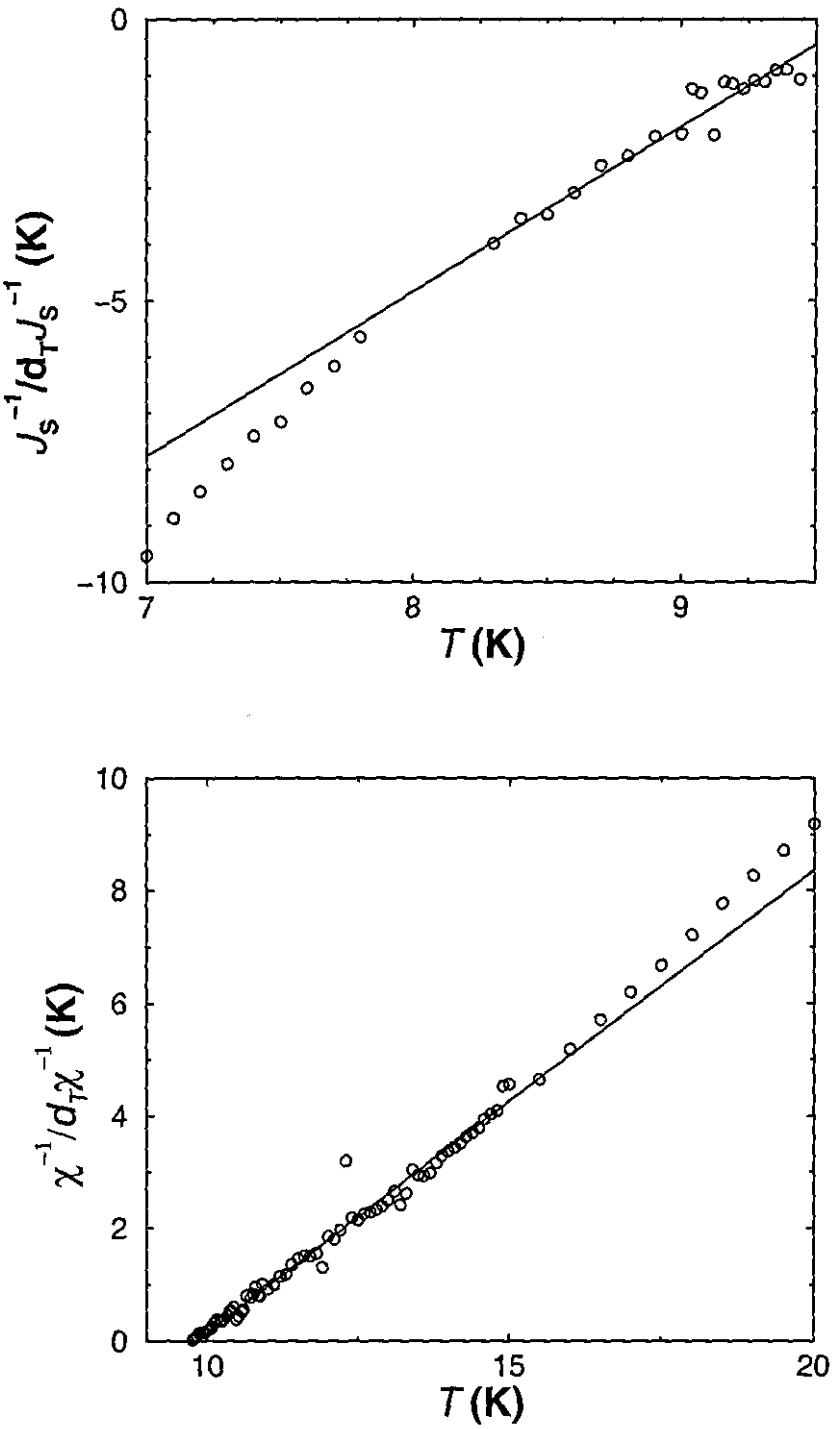

Figure 6.8: Kouvel-Fisher plots for β and γ.

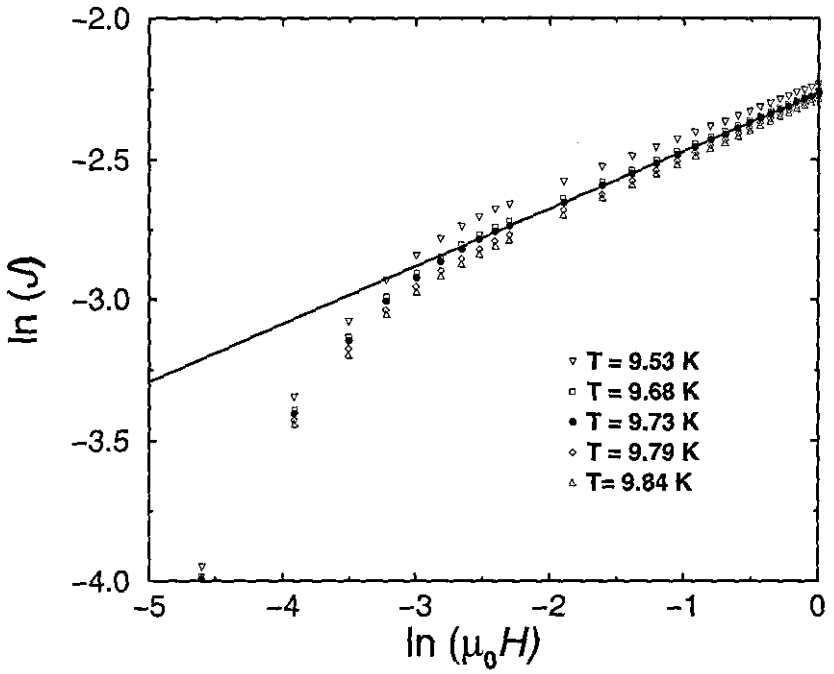

Figure 6.9: Plot of $ln(J)$ versus $ln(\mu_0 H)$ at several temperatures around the critical point of CeAuGe. The straight line is the best least-squares fit to the high field data ($\mu_0 H > 0.1$T).

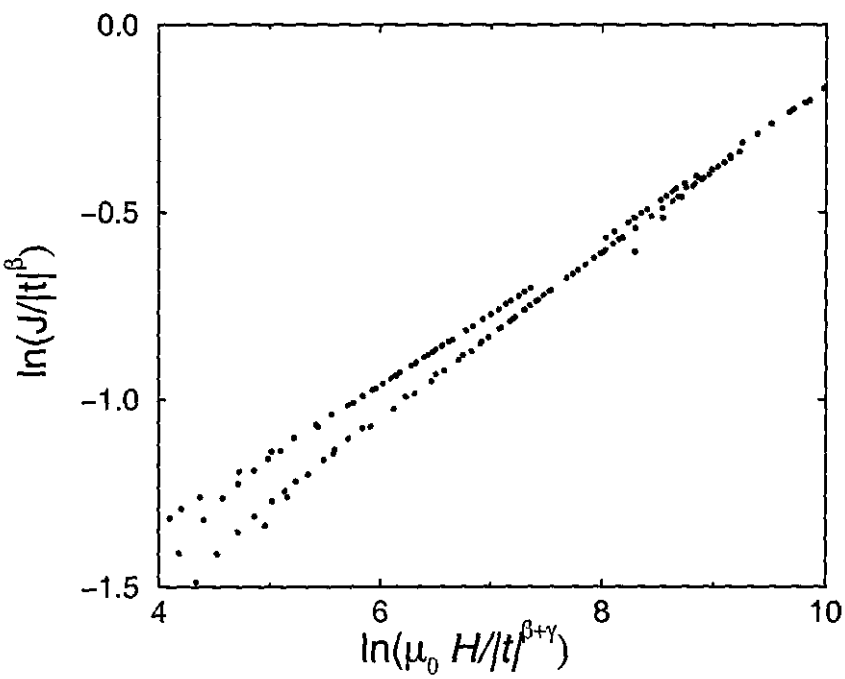

Figure 6.10: Scaling plot using the optimal parameters (see table 6.3.

the data collapses onto branches. This is shown in figure 6.10 for the values $\beta = 0.369$, $\gamma = 1.388$, and $T_C = 9.74$. In addition, the validity of the relationship, $\gamma = \gamma'$ (equation 6.7) may be checked by the variation of γ' and γ independently. In the scaling plot the upper branch represents the data for the ferromagnetic range, and the lower branch for the paramagnetic range.

Critical Amplitudes

The critical amplitude, D, can be calculated from the $ln(J)$ vs. $ln(\mu_0 H)$ plot given in figure 6.9 by considering the intersection of the straight line (representing the critical isotherm) with the $ln(J)$-axis. The critical amplitudes, J_0 and $J_0/J_0/h_0$, are obtained by fitting the corresponding power laws (equations 6.3 and 6.5) to the spontaneous polarisation, $J_S(T)$ and the inverse zero field susceptibility, $\chi^{-1}(T)$. To obtain reasonable amplitudes, the values of the critical exponents as derived from the Kouvel-Fisher method are used. Additionally, both the width of the critical regime and the amplitude are varied. The best fit is considered to be the one with the smallest standard deviation. Using the quantities, J_0, h_0/J_0, and D, the reduced quantities, $J_0/J_S(0)$, $\mu h_0/k_B T_C$, and DJ_0^δ can be calculated, and which are listed in table 6.4. In order to do this, the saturation polarisation, J_0, and the magnetic moment, μ, are determined from a measurement of the magnetic moment at $T = 1.5$K.

6.3.4 Discussion

CeAuGe is seen here to exhibit ferro- or ferrimagnetism, as is evident from figure 6.1(top) in section 6.1. The critical temperature is determined accurately by the various methods which are listed in table 6.5. These are all in excellent agreement with each other, and amount to an average value of $T_C = 9.73(2)$K. This value is consistent with all previous polycrystalline (powder) measurements.

The analysis confirms the existence of a second order phase transition. The experimentally determined values of the critical exponents are seen to be in relatively good agreement with

Table 6.3: Critical exponents as derived from both the different experimental methods and theoretical models. (d=3,n=3): 3D Heisenberg model; (d=3,n=1): 3D Ising model.

	Modified Arrott			Kouvel-Fischer	
	β	γ'	γ	β	γ
CeAuGe	0.365(5)	1.387(5)	1.387(5)	0.369(5)	1.386(6)
(d=3,n=3)	0.365(3)		1.386(4)		
(d=3,n=1)	0.325(2)		1.241(4)		
	Scaling plot			$ln(J)$ vs. $ln(\mu_0 H)$	scaling law
	β	γ'	γ	δ	δ
CeAuGe	0.369(2)	1.388(3)	1.388(4)	4.80(10)	4.76(4)
(d=3,n=3)				4.80(4)	
(d=3,n=1)				4.82(2)	

those derived from the 3D-Heisenberg model, as are compared in table 6.3, together with the results of the 3D-Ising model. Additionally, the exponent values fulfil the scaling law of equation 6.7. This analysis suggests that the critical behaviour of CeAuGe is well described within the limits of the 3D-Heisenberg model.

As well as a determination of the critical exponents, the temperature dependent Kouvel-Fisher exponent

$$\gamma(T) = (T - T_C)\chi(T)\frac{d\chi^{-1}}{dT} \tag{6.11}$$

is calculated, the results of which are plotted in figure 6.11. This describes the temperature dependence of χ^{-1} in the range between the critical regime and the high temperature range described by the Curie-Weiss law. For an isotropic homogeneous ferromagnet, the exponent typically starts at the critical value and decreases monotonically with increasing temperature to the mean-field value of $\gamma = 1$. Previous investigations have shown that a non-monotonic temperature dependence, with a maximum at lower temperatures is seen

Table 6.4: Values experimentally determined for the magnetic saturation and the critical amplitudes as well as a comparison of the reduced critical amplitudes with the theoretical predictions of different models.

	J_S (T)	μ (μ_B)	J_0 (T)	h_0/J_0	D $(T^{1-\delta})$	J_0/J_S	$\frac{\mu h_0}{k_B T_C}$	$\frac{DJ_0^\delta}{h_0}$
CeAuGe	0.137(2)	0.80(2)	0.18(1)	128(4)	52750	1.32(8)	1.28(9)	0.61(30)
(d=3,n=3)						1.37(7)	1.58	1.33(1)
(d=3,n=1)						1.486(1)	1.52	1.81(1)

to be caused by chemical disorder. As the course of $\gamma(T)$ in the case of CeAuGe decreases monotonically, this is a good indication of the high structural order within the compound, especially with respect to the occupation of the Au and Ge positions. However, at higher temperatures, the value of γ dips below the mean-field value of $\gamma = 1$. Such behaviour is usually associated with ferrimagnetic ordering [65].

From the modified Arrott plot (figure 6.6), the existence of magnetic anisotropy is clearly evident. In this plot, the isotherms intersect at a point shifted to the right of the origin on the $(\mu_0 H/J)^{1/\gamma}$-axis. Such an effect has been observed for compounds characterised by a strong magnetic anisotropy [66]. The size of the shift is proportional to the the magnitude of the anisotropy. This anisotropy is corroborated by the observation of the convex curvature of the curves of the $ln(J)$ vs. $ln(\mu_0 H)$ plot (figure 6.11). This has been evidenced in many compounds before with known strong magnetic anisotropy [66].

Table 6.5: Values for the critical temperature, T_C, as derived from different methods (K-F=Kouvel-Fisher plot).

Kink point	Modified Arrott	K-F	K-F	$ln(J)$ vs. $ln(\mu_0 H)$	Scaling plot
T_C(K)	T_C(K)	T_C^-(K)	T_C^+(K)	T_C(K)	T_C(K)
9.7(3)	9.72(4)	9.73(2)	9.72(2)	9.72(4)	9.74(2)

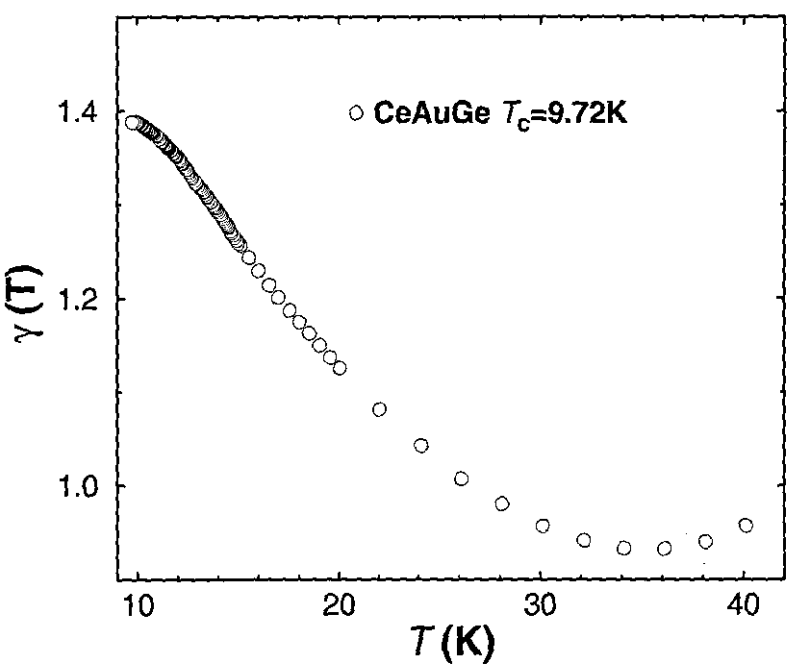

Figure 6.11: Temperature dependence of the Kouvel Fisher exponent.

6.4 Specific Heat Capacity

6.4.1 Experimental

The specific heat capacities of CeAuGe and CeAgGe are measured on polycrystalline lumps of CeAuGe (m = 391.2mg) and CeAgGe (m = 166.6mg) using the apparatus and techniques described in detail in chapter 4.

6.4.2 Results

The specific heat capacities of CeAuGe and CeAgGe are plotted in figures 6.12(top) and 6.12(bottom), respectively, as functions of c_P/T vs. T. The electronic and phonon contributions to the specific heats are subtracted using the specific heat capacities of the non-magnetic and isostructural compounds, YAuGe, and LaAgGe, respectively, with the Debye temperatures scaled to the lattice constants of the two Ce compounds. Details of the electronic and phonon properties of YAuGe and LaAgGe are given in chapter 5 and [16].

CeAuGe

From figure 6.12(top) a fairly sharp anomaly in the specific heat occurs centred at 9.7(K), which is seen to correspond to the ferromagnetic ordering already established from the magnetisation measurements.

The electronic and phonon contributions to the specific heat capacity are calculated by scaling the specific heat capacity of the non-magnetic isostructural compound, YAuGe, to the lattice parameters of CeAuGe. Normally one would expect LaAuGe to be more suited to this purpose, as the atomic mass of La, and also the lattice constants and the degree of puckering of the $[AuGe]_x$ network, are the closest to those of CeAuGe. However, using YAuGe is found to be superior (and also to ScAuGe and LuAuGe) as the shape of the specific heat curve is the most similar to CeAuGe, and is therefore used in the analysis. The electronic and phonon contributions to the specific heat capacity of YAuGe are listed

in chapter 5. In particular, a Sommerfeld co-efficient of $\gamma = 0.4\text{mJ/molK}^2$ is calculated for this compound.

The question regarding the size of γ, is of particular importance for Ce compounds, as most heavy fermion systems are primarily characterised by having an anomalously large value of γ. The value of $\gamma_{\text{YAuGe}} = 0.4\text{mJ/molK}^2$ is calculated from the low temperature linear fit of c_P/T vs. T^2. This is more difficult to calculate in the case of CeAuGe because of the magnetic ordering at 9.7(2)K. There are two methods commonly reported in the literature for determining γ for magnetic compounds. The first involves extrapolating the fit of c_P/T vs. T^2 from a region just above T_C. In the case of CeAuGe, the fit between 12K and 20K results in $\gamma \approx 146\text{mJ/molK}^2$, which is in agreement with values quoted for heavy fermion compounds in the literature using the same method, e.g. $\gamma \approx 123\text{mJ/molK}^2$ for the antiferromagnet, CePdIn [67]. However, these results are dubious at the best, and in the case of CeAuGe are made meaningless by the large Schottky anomaly due to CEF excitations occurring above T_C. A better method is to take the value of C/T as $T \to 0$, as e.g $C/T \approx 700\text{mJ/molK}^2$ at 70mK for CePdIn [68]. Unfortunately, the specific heat of CeAuGe has only been measured down to 1.5K, so a compromise between the two methods is made. The curve of c_P/T vs. T^2 is fitted between 1.5K and 3.5K, where the magnetic contribution has decreased to a low value. This then gives a very approximate value of $\gamma \approx 24\text{mJ/molK}^2$, which still places CeAuGe within the regime of heavy fermion behaviour.

Above T_C, a very large Schottky anomaly is observed up to at least $T = 50$K. Ce is a ${}^2F_{5/2}$ Kramers ion, and is thus expected to split into 2J+1=6 energy levels (or 3 Kramers doublets). The Schottky anomaly is fitted according to this scheme, with the first excited doublet estimated to occur at an energy above ≈ 160K.

The magnetic entropy of CeAuGe is shown in figure 6.13, as is calculated from the integral over the magnetic contribution to the specific heat capacity

$$S_{\text{mag}} = \int_0^\infty \frac{c_{\text{mag}}}{T} dT \tag{6.12}$$

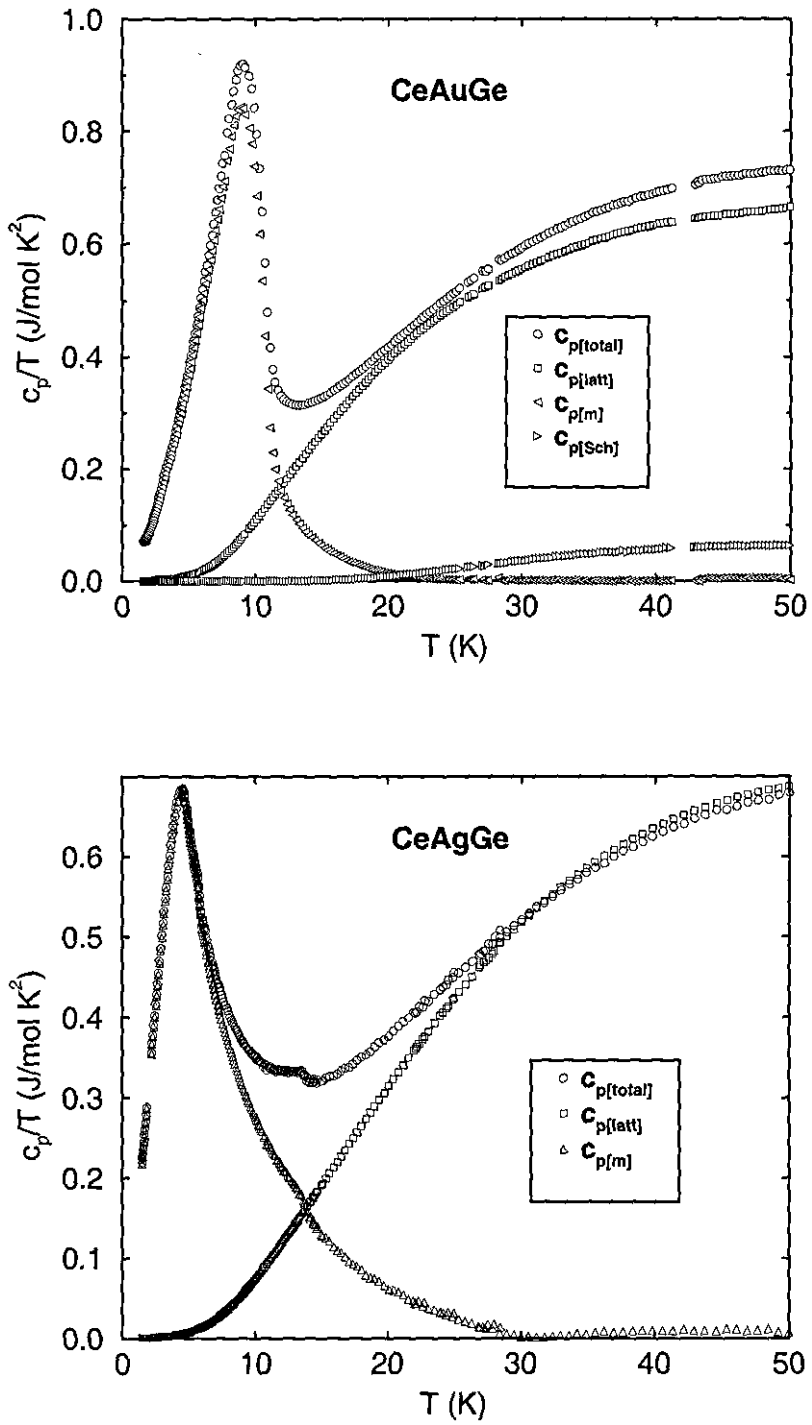

Figure 6.12: Specific heat capacity of polycrystalline CeAuGe (top) and CeAgGe (bottom). The open circles, squares, and triangles represent the measured data, the lattice contributions, and the magnetic contribution, respectively. For CeAuGe, the magnetic contribution is split into its Schottky and ordering components.

where S_{mag} is the magnetic entropy which in this case is plotted in figure 6.13 in units of R, the gas constant. From figure 6.13 it is observed that S_{mag} increases steeply until it reaches a maximum value of Rln(2) at $T \approx 20$K. Above this temperature S_{mag} remains approximately constant at the value of Rln(2). This proves unambiguously that the magnetic Ce ions are in a doublet ground-state.

CeAgGe

The specific heat capacity of CeAgGe, as shown in figure 6.12(bottom), shows a sharp magnetic ordering peak at $T = 4.6(2)$K, which is comparable to the value observed in the susceptibility measurements (4.9K), and the experiments of Pecharsky et. al (4.9(2)K) [12]. Two additional anomalies at $T = 7$K and $T = 14$K are observed above T_N. The 'shoulder' at $T = 7$K probably arises from a small amount of a $CeAg_2Ge_2$ impurity phase, which has been reported in the literature as having an ordering temperature of $T_N = 7$K [52]. The anomaly at $T = 14$K arises from an inconsistency in the experimental measurement.
The electronic and lattice contributions to the specific heat capacity are calculated by scaling the specific heat capacity of the non-magnetic isostructural compound, LaAgGe, to the lattice parameters of CeAgGe. LaAgGe has a Sommerfeld co-efficient of $\gamma = 1.48$mJ/molK^2 as calculated in chapter 5. The value of γ for CeAgGe is calculated from the extrapolation of c_P/T vs. T^2 between T_N and 20K (In this case T_N is too low for the low temperature data to be considered.). This gives a value of $\gamma_{CeAgGe} = 248$mJ/molK^2, which is again comparable to values observed for other heavy fermion systems using the same method.
Above T_N, a small Schottky anomaly is observed, which extends up to $T \approx 60$K. Unfortunately, the quality of the data is not sufficient to determine the excited CEF levels from the Schottky anomaly. However, the specific heat capacity corresponds very well to the measurements of Pecharsky et. al [12], where they estimated that the first excited energy levels lie above 100K.
The magnetic entropy, S_{mag}, of CeAgGe is presented in figure 6.13 alongside that of CeAuGe, and has a very similar behaviour. S_{mag} rises sharply to a maximum of Rln(2) at

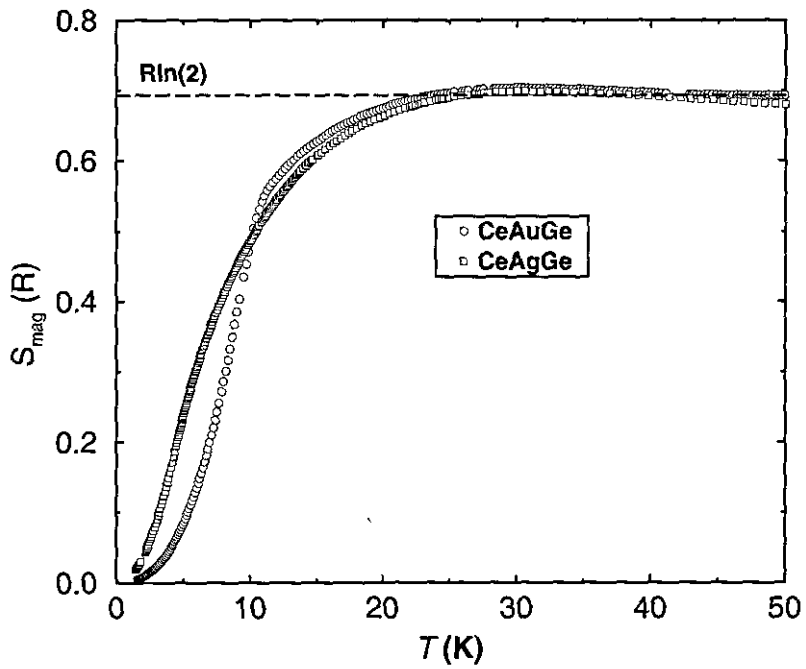

Figure 6.13: Magnetic entropy of CeAuGe and CeAgGe as calculated from specific heat capacity measurements using equation 6.12. CeAuGe and CeAgGe are represented by open circles and squares, respectively. The dashed line shows the value of Rln(2).

approximately $T = 20$K, and remains at this value towards higher temperatures. The value of Rln(2) suggests a doublet ground-state in agreement with the findings for CeAuGe.

6.5 Inelastic Neutron Diffraction

6.5.1 Experimental

The inelastic neutron scattering experiments are carried out using the triple-axis spectrometer, IN3, situated at the ILL reactor in Grenoble. The aim of the experiment is to observe and contrast the different CEF excitations that occur within CeAuGe and CeAgGe. Inelastic neutron scattering is proven to be the most direct method for determining CEF excitations in opaque samples. E.g. it is much superior to their determination from the specific heat Schottky analysis presented in the previous section, and should lead to a more quantitative understanding of the CEF excited states.

The measurements are made on the same coarsely powdered samples of CeAuGe and CeAgGe as used for the neutron elastic scattering experiments on D2B and D20. The samples each have a mass of $\approx$ 8g, which is small compared to the amounts usually required for inelastic neutron scattering experiments. The measured counting rates are correspondingly small. The samples are contained in cylindrical aluminium cans, which produce low incoherent scattering, and mounted in a standard ILL orange cryostat. All the measurements are made at constant temperatures of $T = 20$K and $T = 10$K for CeAuGe and CeAgGe, respectively. These temperatures are well above the magnetic ordering temperatures of both compounds, and should exclude any magnon excitations. Scans in constant momentum transfer of Q=1.5 and Q=2.5 are made for both compounds in the energy transfer range, $-2\text{meV} < \Delta E < 40\text{meV}$ in low resolution mode, and $20\text{meV} < \Delta E < 30\text{meV}$ in high resolution mode.

6.5.2 Results

The scans of CeAuGe and CeAgGe in the energy transfer range, $-2\text{meV} < \Delta E < 40\text{meV}$ at Q=2.5 are presented in figure 6.14, where the CeAgGe data are shown raised for clarity and the region between $20\text{meV} < \Delta E < 30\text{meV}$ is magnified. From this figure a large peak at $\Delta E = 0\text{meV}$ is observed in the scans of both CeAuGe and CeAgGe which corresponds to

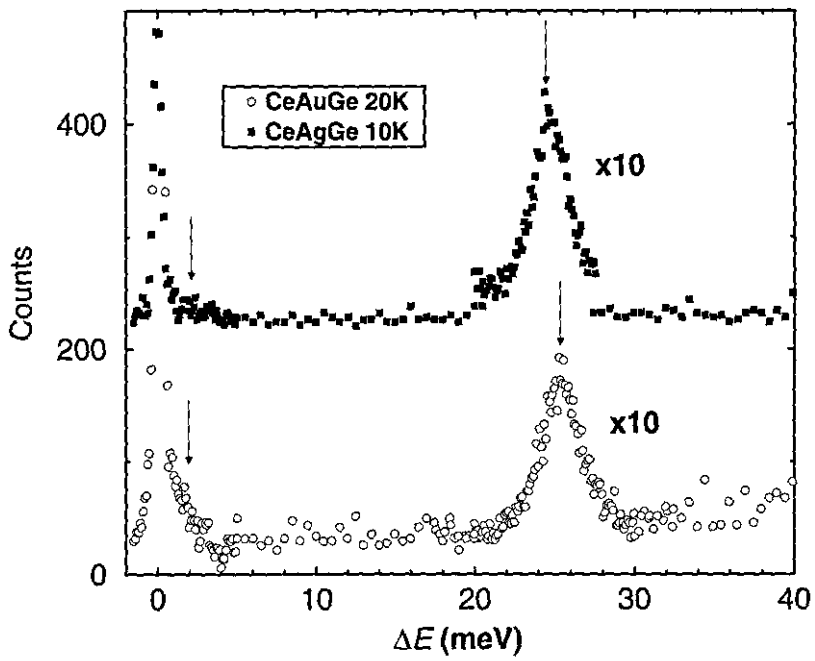

Figure 6.14: Energy transfer spectrum of CeAuGe (circles) and CeAgGe (squares) over the full measured energy transfer range at Q=2.5. CeAgGe is moved upwards by 200 counts for clarity, and the region 20meV $< E <$ 30meV for both scans is magnified. The possible peaks arising from CEF excitations are marked with arrows. The large peaks at $\Delta E = 0$meV are Bragg reflections.

the elastically scattered Bragg reflection. A small additional peak is observed for CeAuGe at $\Delta E \approx 26$meV, as is marked by an arrow in figure 6.14. In the CeAgGe scan, a similar peak is observed at the slightly lower energy transfer of $\Delta E \approx 25.5$meV, which is also marked by an arrow. In both the CeAuGe and CeAgGe scans there is the possibility that another peak may occur at very low ΔE, on the shoulder of the Bragg reflection.

The peaks observed at $\Delta E \approx 26$meV for CeAuGe and at $\Delta E \approx 25.5$meV for CeAgGe arise from CEF excitations. If they are local CEF excitations, and not, for example, phonon excitations, the peak positions in ΔE should be invariant of Q. In contrast, magnon or phonon excitations are Q dependent, having a quadratic dispersion relation, $E \propto Q^2$.

Although magnon excitations should not occur at the temperatures measured, which are well above the respective magnetic ordering temperatures, the assumption is tested by re-measuring the scans in the range $-2\text{meV} < \Delta E < 40\text{meV}$, but at constant momentum transfer, Q=1.5, for both CeAuGe and CeAgGe. The scans at Q=1.5 are not presented here, but show that the peaks remain at the same positions in ΔE in both the CeAuGe and CeAgGe scans, confirming the assumption of CEF excitations.

In order to perform a quantitative analysis of the CEF excitations, high resolution scans are measured at Q=2.5 in the ranges $-2\text{meV} < \Delta E < 5\text{meV}$ and $20\text{meV} < \Delta E < 30\text{meV}$ for both CeAuGe and CeAgGe in order to examine both the shoulders on the Bragg peaks and the peaks at higher ΔE. The results of the scans measured around the Bragg reflection prove inconclusive due to the limited instrumental resolution. These scans are consequently not presented. The results of the $20\text{meV} < \Delta E < 30\text{meV}$ scans are presented in figures 6.15(top) and 6.15(bottom) for CeAuGe and CeAgGe, respectively, and show very clearly Lorentzian shaped peaks, where the function for n Lorentzian peaks is given by

$$y(\Delta E) = y_0 + \sum_{1}^{n} \frac{2A_n}{\pi} \frac{W}{4(\Delta E - E_n)^2 - \delta E^2} \tag{6.13}$$

where y_0 is the background count, A_n is the integrated intensity of the n^{th} peak, E_n the position of the n^{th} peak, and δE is the full width at half the maximum intensity (FWHM). The peaks are primarily fitted taking approximate values of y_0, A_n, and E_n as observed from figure 6.15 as starting values, and refining them simultaneously with δE as a variable. Both the CeAuGe and CeAgGe peaks can in principle be well fitted using single Lorentzian lines. However, when the instrumental resolution is taken into account, the best fit of δE is observed to be somewhat larger than the determined experimental resolution. The resolution for the triple-axis diffractometer, IN3, is shown in figure 6.16 as a function of monochromator energy. A polycrystalline graphite monochromator, PG(002), is used for the experiment, which diffracts neutrons having $\lambda = 2.4\text{Å}$, which is equivalent to an energy of $E(\text{meV}) = 81.81(1/\lambda(\text{Å})^2) = 14.7\text{meV}$. Since the CEF peaks lie at approximately $\Delta E = 25\text{meV}$, E_{mono} should correspond to $14.7\text{meV} + 25\text{meV} \approx 40\text{meV}$. According

Table 6.6: Peak profile data of the fits to the IN3 data for CeAuGe and CeAgGe assuming $\delta E = 2.2$meV.

Compound	y_0	A_1	E_1		A_2	E_2	
	(counts)	(counts)	(meV)	(K)	(counts)	(meV)	(K)
CeAuGe	35(2)	294(32)	24.9(1)	289(1)	252(32)	26.0(1)	302(1)
CeAgGe	25(2)	397(39)	24.4(1)	283(1)	207(40)	25.4(1)	295(2)

to figure 6.16, the corresponding FWHM should lie between 2meV $< \delta E <$ 2.75meV, depending upon the collimator used and the specific experimental conditions.

Assuming δE to be between 2meV and 2.75meV, a single Lorentzian function cannot be suitably fitted to the peaks. For 2meV $< \delta E <$ 2.75meV the peaks can only be fitted well when it is assumed that they are each composed of two Lorentzian peaks. Due to the low instrumental resolution of IN3, such double peaks cannot be distinguished clearly, and the peak positions and integrated intensities vary strongly with the value of δE chosen. It is no longer possible to refine all the Lorentzian parameters together as they converge at similar values to those obtained for the single Lorentzian, but with a very broad peak on one shoulder.

The fits are instead refined keeping the value of δE constant and equivalent for both peaks, and testing different values of δE between 2meV and 3.5meV. A minimum for the standard deviation, χ^2 (as defined in section 6.2), is found for $\chi^2 = 71.9$ at $\delta = 3.0(1)$meV. This corresponds essentially to a single Lorentzian peak with a very small peak next to it. However, the difference in χ^2 is only about 8% across the range of δE tested between 2meV and 3.5meV, and a fit to a double peak having similar integrated intensities is more physically meaningful. The fits to the peaks for CeAuGe and CeAgGe corresponding to a value of $\delta E = 2.2$meV are shown in figures 6.15(top) and 6.15(bottom), respectively, by the dashed lines as representative fits to the double peaks. The details of the fits are summarised in table 6.6.

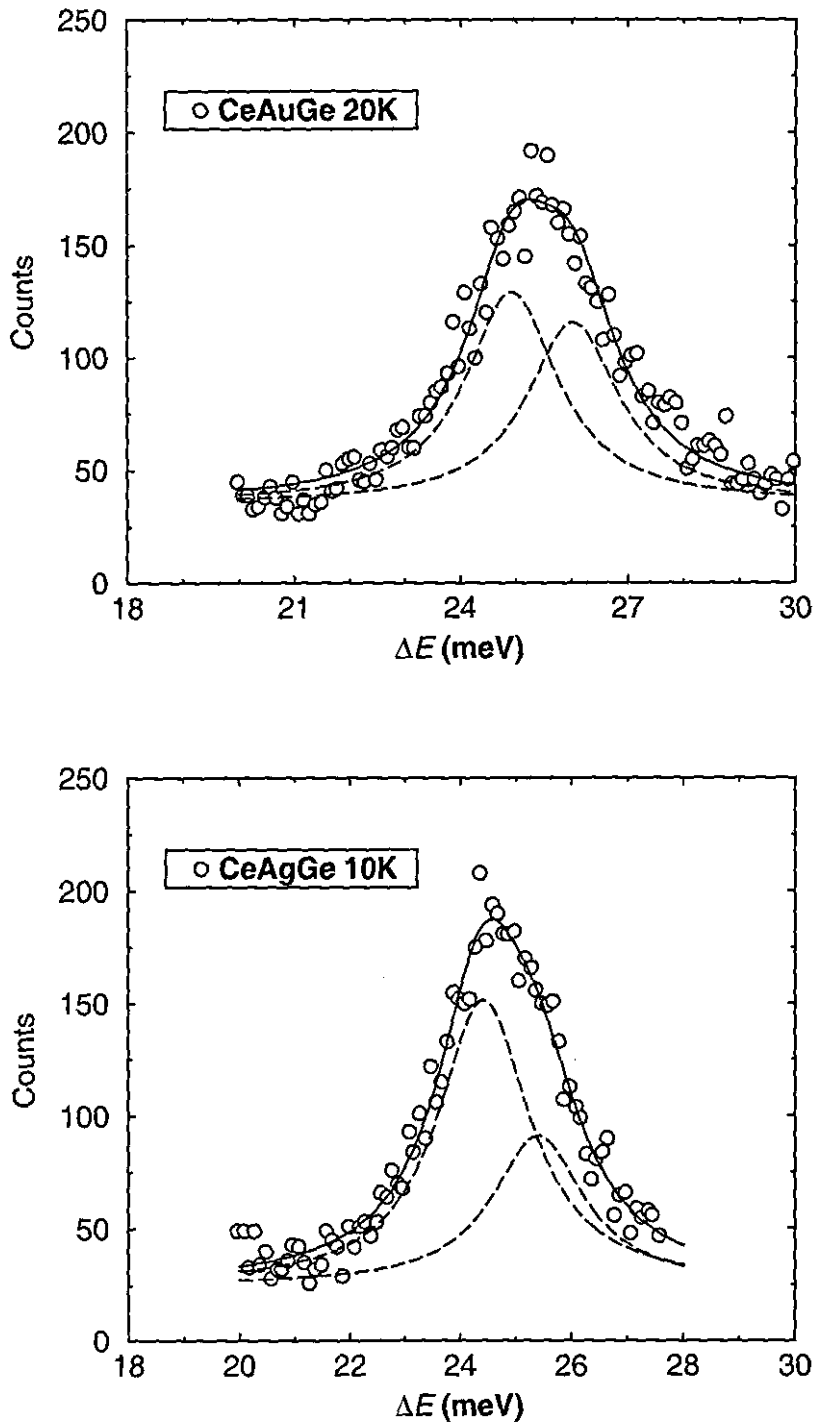

Figure 6.15: Energy transfer spectrum of CeAuGe (top) and CeAgGe (bottom). The measured points are represented by open circles, the fits to individual Lorentzian functions by dashed lines, and the total fits by the full lines.

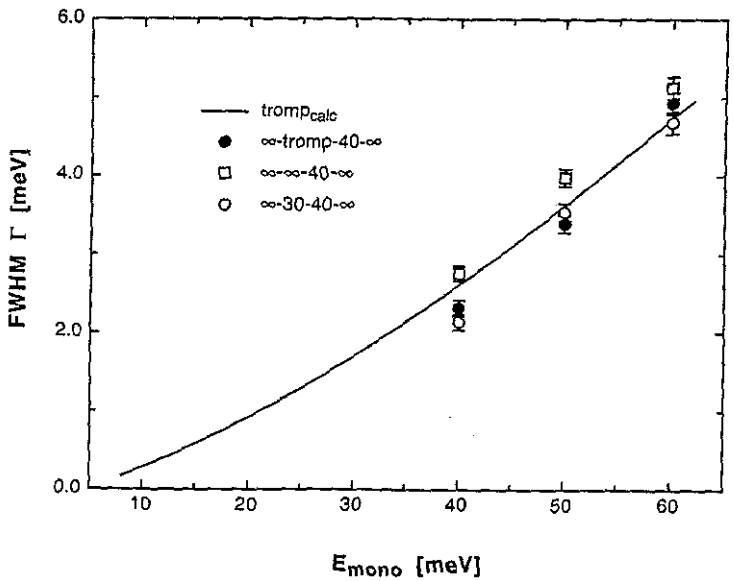

Figure 6.16: Instrumental resolution function of the triple-axis spectrometer, IN3, taken from [77]. The full line is the theoretically calculated resolution function, and the points represent experimental measurements for a Vanadium sample using various types of collimators.

From the results in table 6.6 the first excited states of CeAuGe lie at an energy of $E_1(\text{CeAuGe}) = 24.9(1)\text{meV}$ and at the slightly lower energy of $E_1(\text{CeAgGe}) = 24.4(1)\text{meV}$ for CeAgGe. In both compounds, the second excited levels occur very close to the first excited energy levels, with $E_2(\text{CeAuGe}) = 26.0(1)\text{meV}$ and $E_2(\text{CeAgGe}) = 25.4(1)\text{meV}$. The difference between the first and second excited states is identical for CeAuGe and CeAgGe within the limits of experimental error, being approximately 1.5meV apart.

From the experimental evidence, two possible scenarios can then be envisaged, and which are presented in figure 6.17, in which Ce^{3+} has a total of $(2J+1)/2 = 3$ doublet energy levels. However, both of these models assume that no more excited states occur above $\Delta E = 40\text{meV}$, the maximum instrumental energy transfer.

In the first case, depicted in figure 6.17(a), the $J = 5/2$ ground-state multiplet of the $4f^1$ configuration of Ce^{3+} splits into two almost degenerate doublet ground-states (quasi-quadruplet) and a doublet excited state at $\Delta E \approx 25\text{meV}$. This model assumes that the

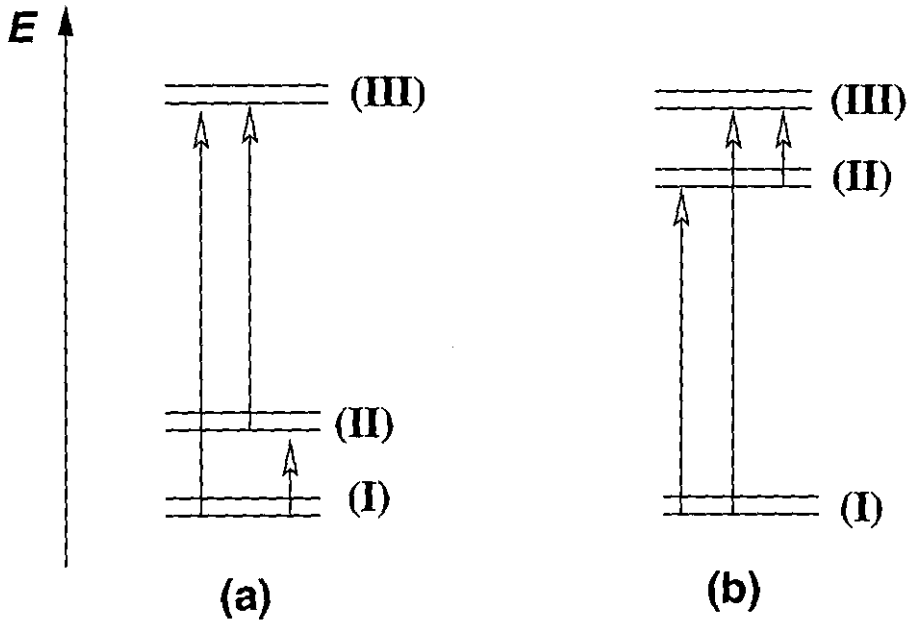

Figure 6.17: Possible energy level schemes for CeAuGe and CeAgGe as proposed from the inelastic neutron scattering experiments. (a) describes a quasi-quadruple ground-state state model with an excited doublet, (b) describes a doublet ground-state model with two excited doublets.

peak at $\Delta E \approx 25$meV is a single (perhaps broadened e.g. due to Korringa relaxation) peak corresponding to the energy difference between (I) and (III). However, this model can be effectively ruled out by the heat capacity measurements which predict the first excited doublet to occur above $\Delta E \approx 15$meV which contradicts the quasi-quadruplet ground-state hypothesis.

In the second case,which is depicted in figure 6.17(b), a doublet ground-state is also predicted. However, the CEF final states consist of two doublet excitations lying quite close together. The peak at $\Delta E \approx 25$meV, must then be considered as the sum of two Lorentzian peaks, with the first peak corresponding to the excitation between the ground-state (I) and the first excited doublet (II), and the second peak corresponding to the excitation energy between the ground-state (I) and the second excited doublet (III). Excitations between (II) and (III) are not visible due to the very low population of (II) as a consequence of the low

temperatures at which the measurements are made. This energy level scheme corresponds to the fits to the data shown in figure 6.15, and is consistent with the results of the heat capacity measurements.

Unfortunately, a conclusive statement as to the CEF splitting in CeAuGe and CeAgGe cannot be made from this experiment due to the ambiguities arising from the low resolution of the experimental data and the limited ($\Delta E_{\max} = 40$meV) range of IN3 over which measurements are possible. It is rather clear that an excitation of ≈ 25meV exists in both compounds.

6.6 CeAuGe Single Crystal Susceptibility

6.6.1 Experimental

The experiments described in this section are performed on the two single crystals of CeAuGe shown in figure 2.3, using the MPMS SQUID magnetometer set-up described in chapter 4. The first CeAuGe crystal (1) is cut with the long axis parallel to the crystallographic c-axis, and has a mass of $m = 60.1$mg. The second CeAuGe crystal (2) is cut with the long axis perpendicular to the crystallographic c-axis, and is slightly larger with a mass of $m = 88.4$mg. Measurements are taken in the temperature range of $2\text{K} < T < 300\text{K}$ and in external fields applied parallel to the long axis up to $H_{\text{ext}} = 7\text{T}$.

6.6.2 Results

The plot of molar magnetic susceptibility against temperature is shown in figure 6.18(top) for both zero field cooled (zfc) and field cooled (fc - 0.1T) conditions, and with H_{ext} both parallel and perpendicular to the crystallographic c-axis. From figure 6.18(top), a very sharp ferromagnetic transition at $T_{\text{C}} = 9.0(1)\text{K}$ is observed. This single crystal Curie temperature is markedly lower than observed from the corresponding polycrystalline measurements in which the value $T_{\text{C}} = 9.72(3)\text{K}$ is very accurately determined from the analysis of the critical region (chapter 6.3). Additionally, an extra shoulder seems to appear at $T_{\text{C2}} \approx 4.5\text{K}$. This is only evident in the zfc curve with the applied field parallel to the c-axis and might be connected with the rearrangement of the ferromagnetic domains.

The amount of magnetic anisotropy present in CeAuGe is quite striking. This is observed very clearly from the magnetisation curves presented in figures 6.19(top) and 6.19(bottom) for magnetic fields applied perpendicular and parallel to the c-axis, respectively. The Ce magnetic moment, μ_{exp} is nearly saturated in an external field of 0.1T when H_{ext} is applied perpendicular to the c-axis, and reaches a saturated value of $\mu_{\text{sat}} \approx 1.2\mu_{\text{B}}$/Ce atom at $H_{\text{ext}} = 7\text{T}$ within the $T = 2\text{K}$ isotherm. This value is in close agreement with previous measurements on polycrystals. However, when H_{ext} is applied parallel to the c-axis, μ_{exp}

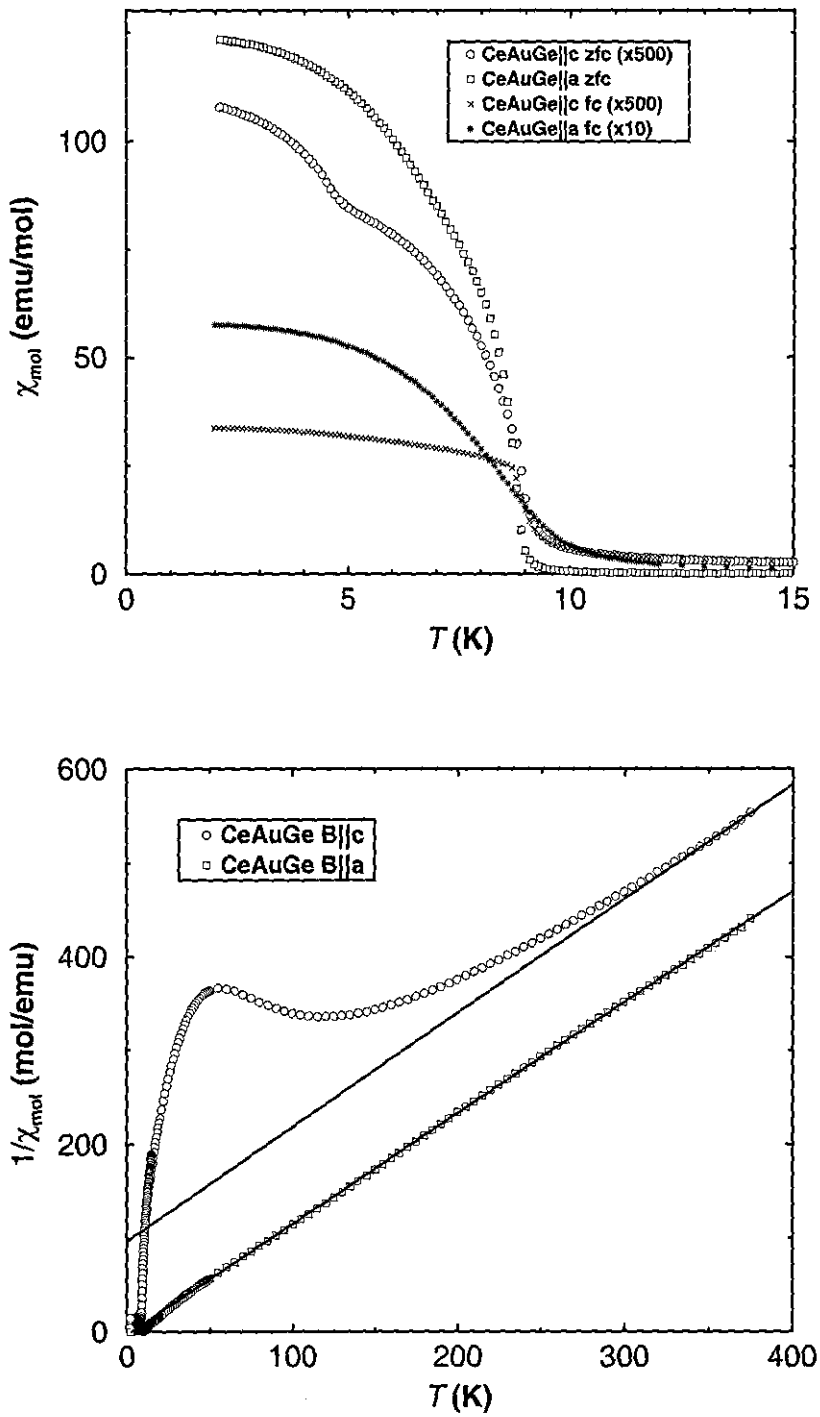

Figure 6.18: (top) Molar magnetic susceptibility of CeAuGe with the applied field both parallel and perpendicular to the crystallographic c-axis. (bottom) Inverse magnetic susceptibility of CeAuGe. The open symbols represent the measured data, and the full line the fit to the Curie-Weiss law.

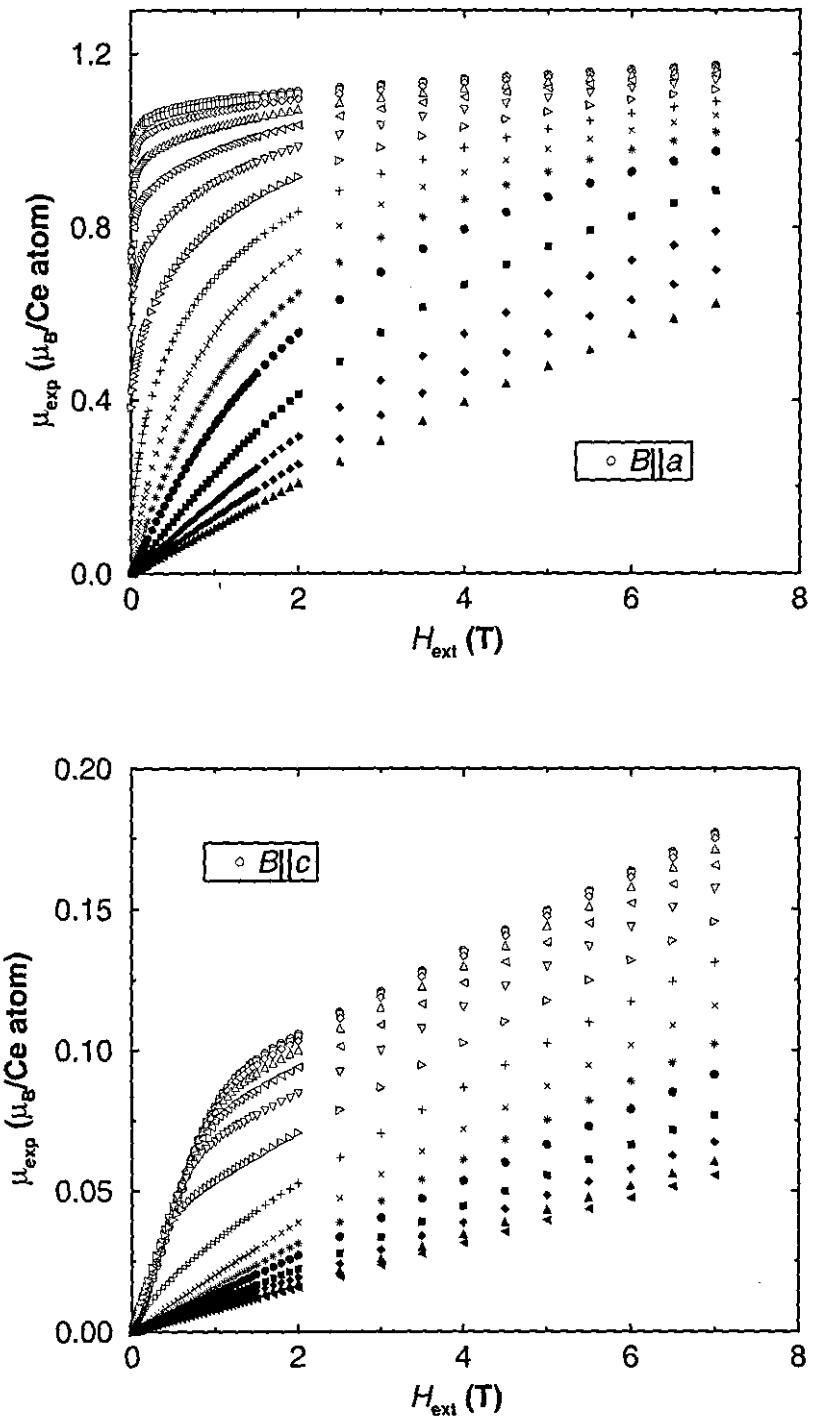

Figure 6.19: Magnetisation curves taken for single crystals of CeAuGe at various temperatures below and above T_C in external fields up to 7T. The crystallographic c-axis is oriented perpendicular (top) and parallel (bottom) to the applied field. The isotherms range from $T = 2$K (open circles) to $T = 20$K (filled triangles).

does not reach saturation up to $H_{ext} = 7$T, and the magnitude of $\mu^{\parallel}_{exp}$ is approximately a factor of ten lower than $\mu^{\perp}_{exp}$ at $H_{ext} = 7$T. These results immediately suggest that the easy axis lies within the ab-plane. This conclusion is in accordance with the earlier magnetic structure determination from the D2B experiment, which shows that the magnetic moments lie almost parallel to the a-axis.

The inverse magnetic susceptibilities of CeAuGe both parallel and perpendicular to the c-axis are presented in figure 6.18(bottom). The measurement with the field lying in the ab-plane is linear above T_C in accordance with the usual Curie-Weiss law, which is shown fitted by the full line above $T = 20$K. The fit results in a value of $\mu^{exp}_{eff} = 2.6(1)\mu_B$ which compares well to to the value of $\mu_{eff} = 2.54\mu_B$ expected for localised Ce^{3+} ions. The Curie-Weiss constant constant is $\theta_P = 2.7(5)$K.

However, the measurement with the external field lying parallel to the c-axis shows a broad maximum in the $1/\chi$ vs. T representation at $T \approx 40$K. Such maxima have been observed previously in other highly anisotropic systems such as $HoNi_2B_2C$ [69], and are a result of the large magnetic anisotropy within these compounds. Here the deviations from the Curie-Weiss start already at $T \approx 350$K. Above this temperature the fit to the Curie-Weiss law, shown by the full, line gives $\mu^{exp}_{eff} = 2.5(1)\mu_B$ and $\theta_P = -78(1)$K which is also in agreement with the value of $\mu_{eff} = 2.54\mu_B$ expected for localised Ce^{3+} ions.

The main contribution to the observed anisotropy in the magnetic susceptibility can be attributed to the CEF splitting of the ground state $J = 5/2$ multiplet of the Ce^{3+} ions. The Hamiltonian describing the contributions arising from the magnetic interactions may be written as

$$\mathcal{H} = \mathcal{H}_{CEF} + \mathcal{H}_{Zee} + \mathcal{H}_{ex} \tag{6.14}$$

where $\mathcal{H}_{CEF}$ is the crystal electric field Hamiltonian, $\mathcal{H}_{Zee}$ arises from the Zeeman splitting, and $\mathcal{H}_{ex}$ is the exchange field Hamiltonian.

The crystal electric field contribution can be written down as the sum of Stevens operators [70], which, in the case of the local C_{3v} crystal symmetry of the Ce atomic sites reduces to

the sum of three terms

$$\mathcal{H}_{\mathrm{CEF}} = B_2^0 O_2^0 + B_4^0 O_4^0 + B_4^3 O_4^3 \tag{6.15}$$

where the B_n^m are CEF parameters which have to be determined experimentally and where the Stevens operators, O_n^m, are sums of J, J_z, and the ladder operators $J_\pm$. These are tabulated, for example, in table 17 of Abragram and Bleaney [72]. The term in O_2^0 usually dominates in the Hamiltonian of equation 6.15. Since this is dependent only on terms in J_z then, to a first approximation, a negative value of B_2^0 corresponds to the magnetic moments lying parallel to the c-axis, and a positive value of B_2^0 corresponds to the magnetic moments lying perpendicular to the c-axis.

The Zeeman splitting term is given by

$$\mathcal{H}_{\mathrm{Zee}} = g_{\mathrm{J}} \mu_{\mathrm{B}} \vec{B} \cdot \vec{J} \tag{6.16}$$

where g_{J} is the Landé g-factor.

The program *Simult* [71] has been developed in order to determine the splitting of the six degenerate energy levels for Ce compounds under any given CEF environments. The program works by calculating a theoretical value of the inverse susceptibility, and comparing this with the experimental values. The theoretically determined susceptibilities are refined using a least-squares method where the exchange interactions are considered in a mean field theoretical (MFT) approach by the parameter λ, assuming temperatures high above T_{C}, is used [49]. Then

$$\frac{1}{\chi_{\mathrm{theor}}} = \frac{1}{\chi_{\mathrm{CEF}}} + \lambda \tag{6.17}$$

where χ_{CEF} is a function of B_2^0, B_4^0, B_4^3, T, and $\vec{B}$. Then, assuming small magnetic fields,

$$\chi_{\mathrm{CEF}} = \frac{dM}{dB} \approx \frac{M}{B} \tag{6.18}$$

Table 6.7: Results of the best simultaneously fitted parameters to the measured data of the susceptibility of single crystals of CeAuGe.

B_2^0	B_4^0	B_4^3	λ	χ_0	E_0	E_1	E_2
	(K)		(mol/emu)	(10^{-6} emu/mol)		(meV)	
9.4	-0.52	15.5	18.4	-16.5	0	24.9	30.6

where M is calculated from a consideration of Gibb's free energy, $M = -dF/dB$ and $F = -RT \ln Z$, where Z is the partition function, $\sum_i \exp E_i/k_B T$. The partition function is summed over all values of the $2J + 1$ energy levels as determined from a diagonalisation of the 6x6 Hermitian matrix [72]. The calculated energy values are used and iteratively worked backwards through the procedure to compare χ_{theor} with χ_{meas}.

The susceptibility curves of figure 6.20 with $B \perp c$ and $B||c$ are fitted simultaneously using the program *Simult* previously described. Five parameters are ultimately refineable, B_2^0, B_4^0, B_4^3, λ, and χ_0. The best fits are listed in table 6.7. Of note is the positive value of B_2^0 which corresponds to magnetic moments parallel to the c-axis in agreement with neutron diffraction. The fits are represented by full lines in figure 6.20, and are seen to be in good agreement with the experimental data for $B||c$ and in fair agreement for $B \perp c$. The final results produce values for the excited energy states with a ground state doublet at $E_0 = 0$meV, a first excited doublet at $E_1 = 24.6$meV, and a second excited doublet situated at $E_2 = 30.6$meV. The first excited state is in fair agreement with the second possible excitation energy level scheme derived from the inelastic neutron scattering and specific heat capacity results, which predict a Kramers doublet ground state and the first excited doublet at $E_1 = 25$meV. However, the second predicted excited doublet is not observed in the inelastic neutron scattering experiments, although this could just be a consequence of the insufficient neutron counting statistics achieved in the scans up to $\Delta E = 40$meV.

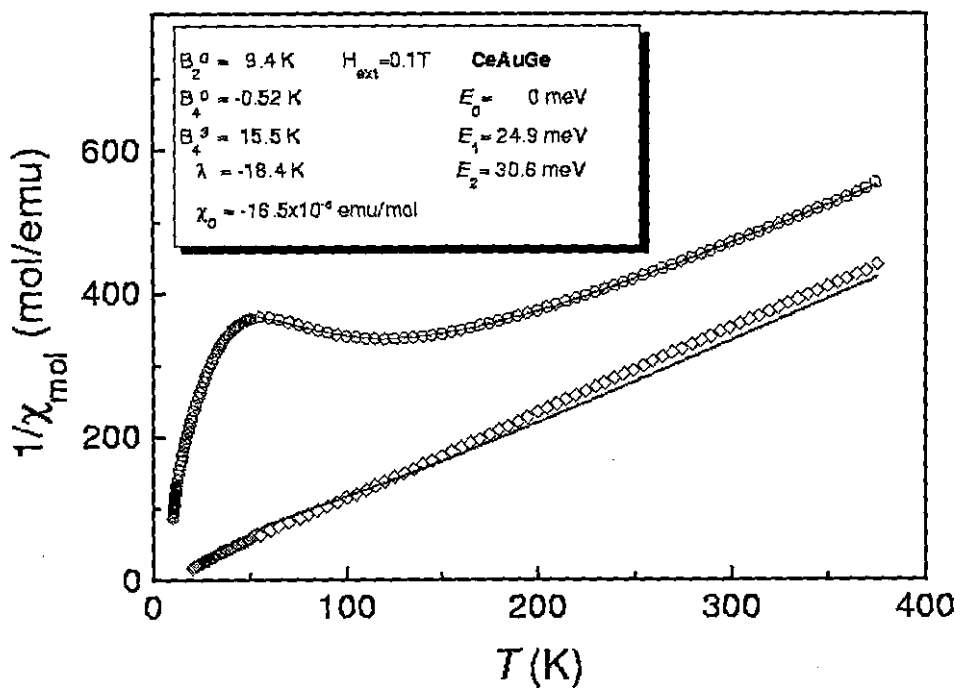

Figure 6.20: Inverse magnetic susceptibility of a CeAuGe single crystal both parallel and perpendicular to the c-axs. The open symbols depict the experimental data, and the full lines the fits according to the CEF parameters given in the text.

6.7 First Pressure Experiments on CeAuGe.

The changes in the crystal structure of CeAuGe under elevated pressures have been recently resolved by Schwarz [74]. The results are presented here in figure 6.21, where the measured lattice parameters of CeAuGe are plotted as a function of pressure up to $P = 20$GPa. At ambient pressure the crystal structure of CeAuGe corresponds to a ternary ordered $CaIn_2$ type (NdPtSb branch) structure as detailed in chapter 3. A monotonic decrease in the lattice parameters is then observed as pressure is applied. This change corresponds to a gradual increase of the buckling of the $[AuGe]_x$ polyanion layers until 3D $[AuGe]_x$ cages are formed (LiGaGe branch). This alteration in structure is also readily observed upon replacing Ce with RE atoms of smaller size [13], and also upon decreasing temperature.
At a pressure of $P = 8$GPa there is a discontinuity in the lattice parameters, indicating an abrupt change in the crystal structure. Above $P = 8$GPa CeAuGe crystallises in the orthorhombic TiNiSi type structure (compare EuAgGe in chapter 3). As the pressure is further increased a monotonic decrease in the lattice parameters is again observed.
The pressure studies in the following are motivated as a consequence of the large changes in crystal structure that occur in CeAuGe. In particular, it is extremely interesting to examine the effect of the Ce interatomic distances on the magnetic ordering temperature.

6.7.1 Experimental

The magnetic susceptibility of CeAuGe is measured using the MPMS SQUID magnetometer described previously in chapter 4 in conjunction with a specially designed hydrostatic pressure cell [73].
A small polycrystalline sample of CeAuGe ($m = 6.2$mg) is sealed into a Teflon capsule together with a small piece of pure lead, and the surrounding space filled with a *Flourinert* pressure transmitting liquid medium. The Teflon capsule is subsequently loaded into the pressure cell, where a maximum pressure of approximately 10kbar can be applied through the action of a hydraulic press and screw mechanism. It is assumed that through the action of the pressure transmitting medium that hydrostatic, and not uniaxial, pressure is applied

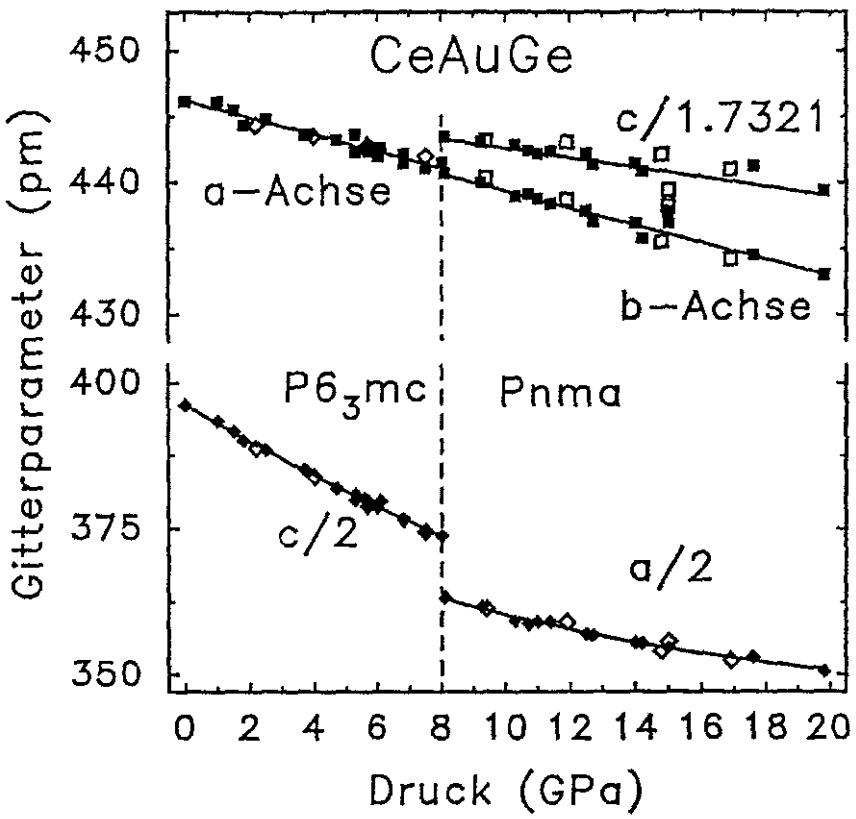

Figure 6.21: Lattice parameters of CeAuGe as a function of pressure up to 20GPa taken from [74]. The dashed vertical line at 8GPa represents the phase transition from the ordered $CaIn_2$ structure to the TiNiSi type structure.

to the sample.

The magnetic susceptibility is measured from $T = 6$K to $T = 15$K around T_C in a small external field of $H_{ext} = 10^{-3}$T. Two sets of six measurements are made, the first five in each set with consecutively increasing amounts of pressure being applied to the sample from 0kbar to the maximum available, and the final measurement with the pressure released.

6.7.2 Results

The magnetic susceptibility of CeAuGe close to T_C under several different pressures (second set only) is shown in figure 6.22. Two transitions are observed in each curve. The transition

at $T \approx 10$K arises from the ferromagnetic ordering of CeAuGe, and the lower transition, at $T \approx 7$K, from the superconducting transition of Pb. There is a clear increase in the T_C of CeAuGe with increasing pressure.

The small Pb sample is added to the pressure cell so that the the magnitude of the applied pressure can be calculated accurately. The superconducting transition temperature of Pb under normal conditions is $T_C = 7.2$K. The change in T_C of Pb under elevated pressures has been determined previously with great accuracy [75], and the dependence of the superconducting transition of Pb with applied pressure is empirically given by

$$P(\text{GPa}) = 19.516 - 2.675T_C(\text{K}) - 0.00498T_C^2(\text{K}^2) \tag{6.19}$$

where T_C is the superconducting transition temperature of Pb.

Therefore, by measuring the Pb transition temperature, the pressure on the sample is given very accurately by equation 6.19. In the first set of measurements the Pb transitions are not as sharp as maybe expected, which would suggest that hydrostatic conditions are not completely realised within the pressure cell, and the broadening of the transitions could be due to the direct action of the uniaxially applied pressure on the samples. The second set of measurements (figure 6.22) show much sharper Pb transitions up to the highest pressures, indicating that the problems of hydrostatic pressure are resolved in this case.

The calculated values of T_C for CeAuGe as defined by the point of inflection are plotted in figure 6.23 against the determined pressure values. The maximum pressure achieved with the pressure cell is $P \approx 10$kbar, and the Curie temperature ranges from a value of $T_C = 10.2$K at ambient pressure to $T_C = 11.86$K at $P = 8.5$kbar for the second set of measurements. In figure 6.23, the results of the first set of measurements are represented by open squares, and the second set by open triangles.

The results of the first and second sets of measurements are in good agreement with each other at low pressure. A linear increase of T_C with increasing pressure is observed for the second set of measurements. The positive deviation from linearity of the first set above $P \approx 3$kbar very likely results from the non-hydrostatic conditions within the pressure cell

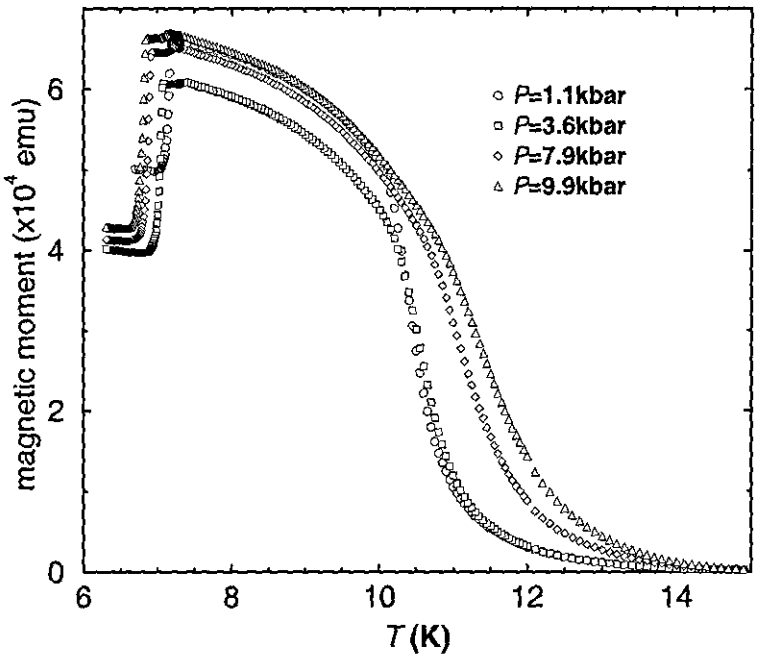

Figure 6.22: Magnetic susceptibility of CeAuGe under elevated pressures. Only the second set of measurements are shown.

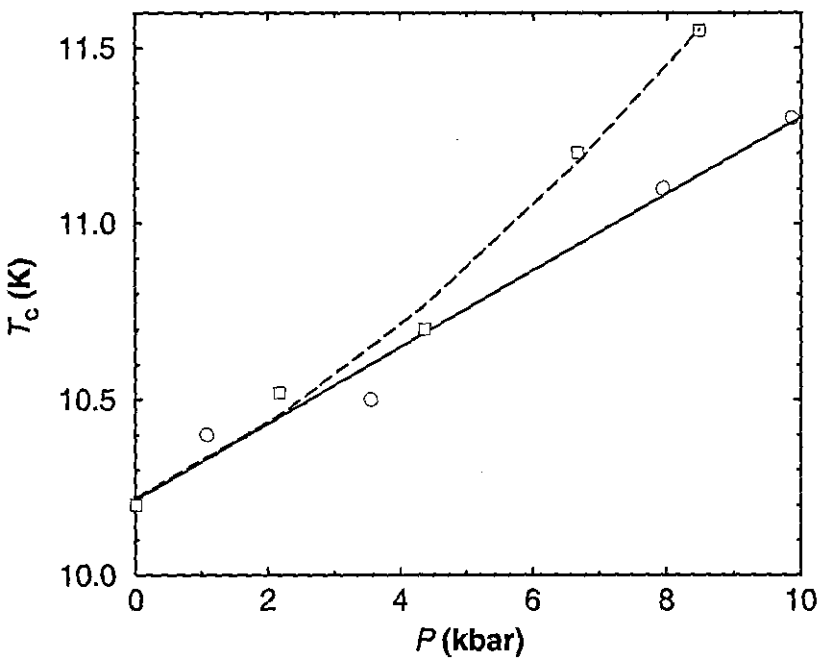

Figure 6.23: Change of Curie temperature of CeAuGe with increasing pressure up to 10kbar. The open squares (first set) and circles (second set) represent the T_C at P as derived from the susceptibility measurements. The full line is a linear fit to the deduced values.

in the first run.

The second set of data points is fitted extremely well using a straight line, and extrapolate back to a zero pressure value of $T_C = 10.2$K, which is in good agreement with previously determined measurements on polycrystals. From the slope of the fitted line an increase in T_C of $0.11 \cdot 10^{-2}$K/kbar is determined. The increase of T_C over the measured pressure range of $\approx 10\%$ is observed to be due to changes in the exchange interactions. CEF effects play a very minor role in the change in T_C as is observed by the nearly constant Ce magnetic moments for all the measurements.

6.8 Discussion

Throughout this chapter many varied techniques are utilised in an attempt to elucidate the differing magnetic properties of CeAuGe and CeAgGe, although a more considerable amount of effort is put into the examination of CeAuGe than CeAgGe. This is partly because the ferromagnetic ground-state of CeAuGe warrants and facilitates such studies as the determination of its behaviour around the critical regime, which is not so straightforward with the antiferromagnetic CeAgGe, and is also partly due to the availability of large, good quality single crystals of CeAuGe which are examined here for the first time.

The magnetic structures of both CeAuGe and CeAgGe are determined by elastic neutron scattering on polycrystalline samples. CeAuGe is found to have a simple ferromagnetic structure at $T = 1.5$K with the magnetic moments aligned along the a-axis within the limits of experimental error, which is fairly large considering the very low intensity of the observed magnetic peaks. Any type of ferrimagnetic ordering can, however, be ruled out. The magnitude of the Ce magnetic moments is $\approx 1.1\mu_B$, which is in remarkable agreement with the high field saturated magnetic moment of $1.09(2)\mu_B$/Ce ion determined from the polycrystalline magnetisation measurements.

CeAgGe on the other hand has an antiferromagnetic structure at $T = 1.5$K. This is described by a $\tau = [1/3, 0, 0]$ propagation vector, i.e a magnetic unit cell which has an a-axis that is three times the crystallographic a-axis. The magnetic moments lie exclusively in the ab-plane, and have a magnitude of $\approx 1.6\mu_B$ which can be compared to the saturated magnetic moment of $1.02(5)\mu_B$/Ce ion obtained from magnetisation measurements. As with CeAuGe the experimental error of the neutron scattering experiment is quite high.

That the Ce magnetic moment in both CeAuGe and CeAgGe is substantially reduced from the Ce^{3+} free ion value of $2.54\mu_B$ is a frequent observation in Ce based intermetallics, and in this case is explained in terms of the large CEF acting on the Ce ions.

The crystal electric field excitations are examined using three methods (i) specific heat capacity, (ii) inelastic neutron scattering, and for CeAuGe (iii) single crystal susceptibility. The resolution of the heat capacity measurements is not sufficient to determine the posi-

tion of the excited states, except to say that the first excited levels occur above $\approx$ 15meV. However, for both compounds, the magnetic entropy very quickly reaches a value of $R\ln 2$ which unambiguously proves a CEF doublet ground-state. However, since Ce splits into $(2J+1)/2 = 3$ doublet states, this still leaves a question mark over the position of the other two doublet levels.

While on the subject of the specific heat capacity measurements it is appropriate to mention the estimated values of the Sommerfeld co-efficient, γ. Unfortunately, although several guesses are made at values of γ which place it within the range of heavy fermion behaviour, it is clear that the large magnetic contribution at low temperatures corrupts these estimates and makes them unreliable. It therefore has to be concluded that there is not sufficient evidence of heavy fermion behaviour from the specific heat or any hint of heavy fermion behaviour in any of the other magnetic or transport measurements performed on CeAuGe or CeAgGe.

From the inelastic neutron scattering results, a broad peak (compared to that expected from the instrumental resolution) is observed for both CeAuGe and CeAgGe at an energy transfer of $E \approx 25$meV. No other peaks are observed up to $E_{\max} = 30$meV in the high resolution scans and up to $E_{\max} = 40$meV in the low resolution scans. There are then two plausible energy level schemes that are consistent with the specific heat capacity results. The first is a doublet ground-state with two very closely spaced doublets (a quasi-quadruplet) situated at $E \approx 25$meV. The second corresponds to a doublet ground-state, with one excited doublet at $E \approx 25$meV (with a thermally broadened peak), and a second doublet at $E > 40$meV, although other low intensity peaks between 30-40meV cannot be ruled out.

The simultaneous CEF fits to the high temperature single crystal susceptibility of CeAuGe parallel and perpendicular to the c-axis result in an energy level scheme of $E_1 = 0$meV, $E_2 = 25$meV, and $E_3 = 31$meV, which is also fits with the preceding experiments. However, a more detailed inelastic neutron diffraction study of both CeAuGe and CeAgGe is needed to clarify this situation.

Several interesting results are also obtained from the analysis of the behaviour of CeAuGe

within the ferromagnetic critical regime. Firstly, the Curie temperature of CeAuGe is determined very accurately to be $T_C = 9.72(3)$K for polycrystals. The surprising result is the contrast to the single crystal susceptibility which clearly shows a sharp ferromagnetic transition at the significantly lower temperature of $T_C = 9.0(1)$K. It is possible that the lower temperature could arise from disorder among the Au/Ge atomic sites. However, due to the size of the crystals, elastic neutron scattering is necessary to determine the exact atomic arrangement on the lattice sites in a similar manner to their determination from single crystal X-Ray diffraction. Another interesting feature of the single crystal susceptibility measurements is the additional transition that is observed with the external field applied parallel to the c-axis, although this result remains unexplained at the present.
The analysis of the critical regime of CeAuGe also hints at the strong magnetic anisotropy which is clearly evident in the single crystal measurements. Additionally, the evaluation of the critical exponents, γ, β, and δ, together with the critical amplitudes shows strong agreement with the corresponding values determined from the 3D-Heisenberg model. Since the underlying magnetic properties of CeAgGe have been seen up to now to almost mirror those of CeAuGe is it also tentatively suggested that a similar large magnetic anisotropy would also be observed in CeAgGe single crystals.

Chapter 7

Magnetic Structure Determination

7.1 Introduction

The magnetic structures of the heavy rare-earth gold and silver germanides, REAuGe and REAgGe, with RE=Tb, Dy, Ho, Er, are systematically studied in this chapter by the method of elastic neutron diffraction experiments on powdered samples. This study is motivated by the observation of complex magnetic ordering behaviour found within these compounds which is already observed in the susceptibility and specific heat capacity measurements reported in chapter 4. These measurements show that the REAuGe compounds order antiferromagnetically, and in the case of HoAuGe and ErAuGe show additional re-orientation of the magnetic moments below T_N. DyAgGe orders ferromagnetically, with possible further re-orientation below T_C, and the other REAgGe order antiferromagnetically. However, since all the compounds within a given series crystallise in the same structure type (REAuGe - $CaIn_2$ derivative; REAgGe - Fe_2P derivative) it is anticipated that their magnetic structures could be related. Therefore the experiments detailed within this chapter are performed in order to determine and contrast the types of magnetically ordered structures that are formed below $T_{N/C}$, and also to observe any changes with temperature that may occur.

Magnetically ordering compounds that contain heavy rare-earth elements (Tb-Tm) have

been previously proven to be particularly suitable for elastic neutron diffraction studies because (a) they are comparatively low absorbers of neutrons compared to other RE elements, e.g. Gd, and (b) their magnetic moments are observed to be of a suitable size ($\approx 10\mu_B$) for coherent magnetic diffraction effects to be of the same order of magnitude as nuclear diffraction. This enables the possibility of simultaneously performing magnetic structure refinements alongside nuclear structure refinements, and using the Rietveld method [80]. All the elastic neutron diffraction measurements described in this chapter are performed on either the high-flux, low-resolution diffractometer, D1B, or the more recent high-flux, medium-resolution diffractometer, D20, situated at the ILL in Grenoble, France.

7.2 Experimental

7.2.1 D1B Instrumentation Characteristics

D1B is a two-axis diffractometer which is set up to produce a high neutron flux (with a correspondingly low resolution). This makes it ideally suited for the determination of magnetic structures, since both the magnetic peak intensity and instrumental resolution decrease rapidly with increasing scattering angle. Therefore intensive magnetic peaks are only expected at low angles where the resolution is still expected to be sufficient (FWHM$\rightarrow$ 0.2°).

The schematic layout of D1B is shown in figure 7.1. Thermal neutrons are taken from the neutron guide at a take-off angle of $\approx 44°$ by a pyrolytic graphite (002) monochromator. This leaves the neutrons with a wavelength of $\lambda = 2.52$Å, which are focused onto the sample using a set of Soller collimating slits. This set-up achieves a maximum flux at the sample of about $6.5 \times 10^6 \text{ncm}^{-2}\text{s}^{-1}$, and has a maximum beam cross-section of $5 \times 2\text{cm}^2$. The sample is contained in a standard ILL Orange cryostat which is specially designed to produce a low background count, and which allows temperatures down to $T \approx 1.5$K. The neutrons are subsequently scattered by the sample into a ^{3}He multi-detector. The multi-detector consists of 400 cells, each covering an angular range of $2\theta = 0.2°$, making

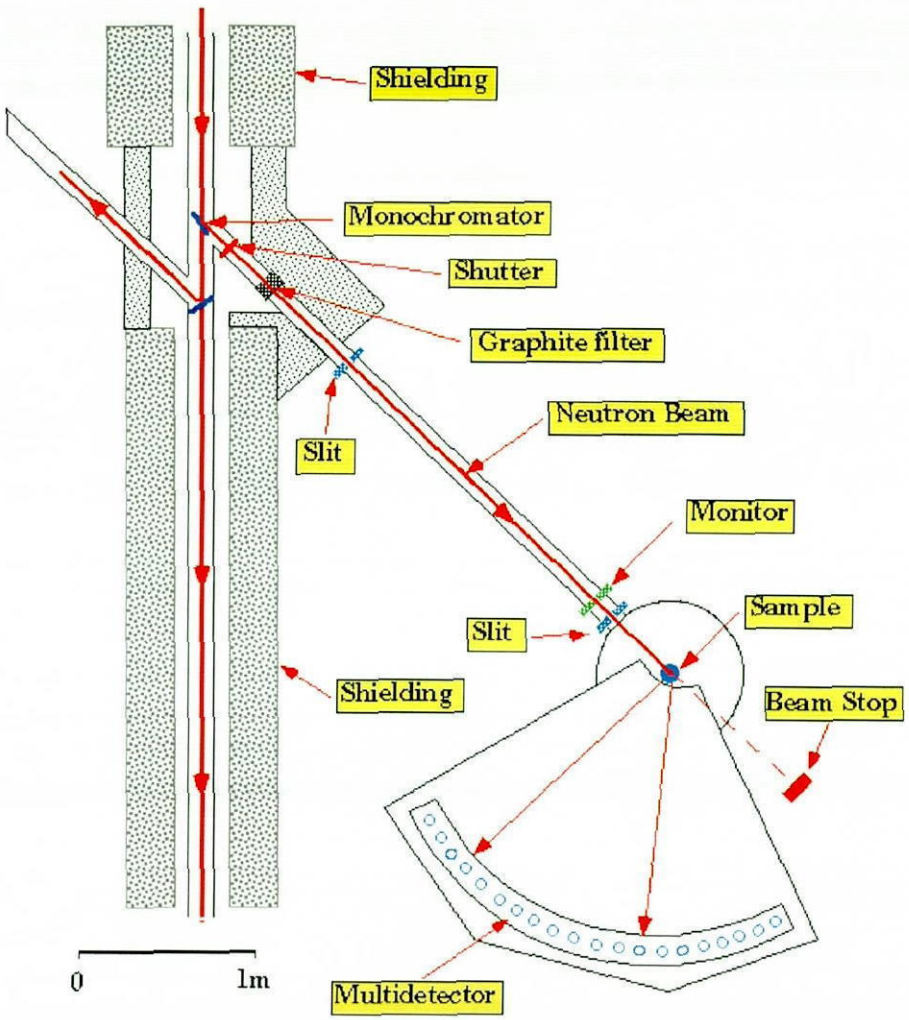

Figure 7.1: Schematic layout of D1B taken from [78].

up a full detector range of $2\theta = 80°$. At a wavelength of $\lambda = 2.52$Å, the detector efficiency is about 60%.

7.2.2 D20 Instrumentation Characteristics

The high-flux medium-resolution diffractometer, D20, is a recently developed instrument at the ILL (first operated in mid 1997) that aims to provide the high neutron flux available on D1B, combined with much higher resolution. The instrument layout is very similar to D1B in being a two-axis diffractometer, and is therefore not shown.

In the experiments described in this chapter, neutrons are taken off the beam guide using a pyrolytic graphite (002) monochromator at an angle of 42°. This leaves the neutrons with a wavelength of $\lambda = 2.41$Å, and enables a neutron flux of $3.7 \times 10^7 \text{ncm}^{-2}\text{s}^{-1}$ at the sample. The beam is collimated using several sets of Soller slits, and a set of adjustable slits situated between the monochromator and the sample. The resolution of the instrument can therefore be controlled by adjusting the slits, and is also dependent on the sample diameter.

In correspondence with D1B, the sample is contained in an ILL Orange cryostat. The neutrons are diffracted by the sample into a detector bank consisting of a ^{3}He micro-strip gas-detector. It consists of 1600 detection cells, each with a height of 150mm and an angular width of $2\theta = 0.1°$, giving a detector range of $2\theta = 160°$ combined with a very high counting efficiency.

7.2.3 Sample Preparation

Approximately 7g each of the previously prepared polycrystalline samples are ground into a coarse powder using an agate pestle and mortar. The powders are subsequently enclosed in thin walled vanadium sample holders of the dimensions shown in figure 7.2(left). For the compounds containing elements which are strongly neutron absorbant, i.e gold, which has a neutron absorption cross-section of ≈ 99 barn, a double walled vanadium holder is used (figure 7.2(right)) in order to reduce the neutron absorption.

7.2.4 Experimental Setup

The vanadium sample holder is placed in a standard I.L.L orange cryostat, allowing temperature control from $T \approx 1.5$K up to room temperature. The cryostat is mounted on the θ-table in such a way that the sample sits centrally within the neutron beam line, and the neutrons diffracted into the detector bank. Measurements are taken for all of the samples, REAuGe and REAgGe (RE=Tb-Er), firstly at the lowest temperatures, and again at a temperature just above the magnetic ordering transition under identical (except tempera-

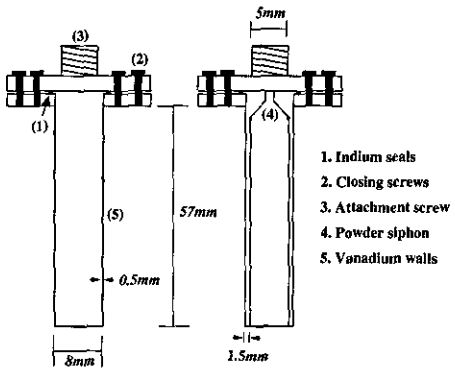

Figure 7.2: Vanadium sample holders used for neutron powder diffraction. (left) Single walled vanadium can. (right) Double walled vanadium can.

ture) conditions, i.e. total neutron count, wavelength, 2θ range, and beam size. Depending upon the time permitted for the individual experiments, scans in temperature between the two extremes are also performed.

The instruments are both controlled using Silicon Graphics workstations, and with the programs, *Lamp*, *PlotPow*, and *Fullprof* [79], being used for the data acquisition, visualisation and treatment.

7.3 Heavy Rare-Earth Gold Germanides

7.3.1 Nuclear Structures

Diffraction patterns of each of the four compounds, TbAuGe, DyAuGe, HoAuGe, and ErAuGe, are recorded at temperatures just above T_N in the angular range $5° < 2\theta < 85°$. These diffraction patterns are shown in the upper panels of figures 7.3 - 7.6, respectively. The temperatures are chosen to be high enough that no coherent magnetic scattering is observed, but low enough that the crystallographic parameters can be subsequently used in the magnetic structure refinements.

The low instrumental resolution of D1B is quite apparent from figures 7.3 - 7.6, and a total of eight Bragg reflections in each diffraction pattern are observed within the 2θ range

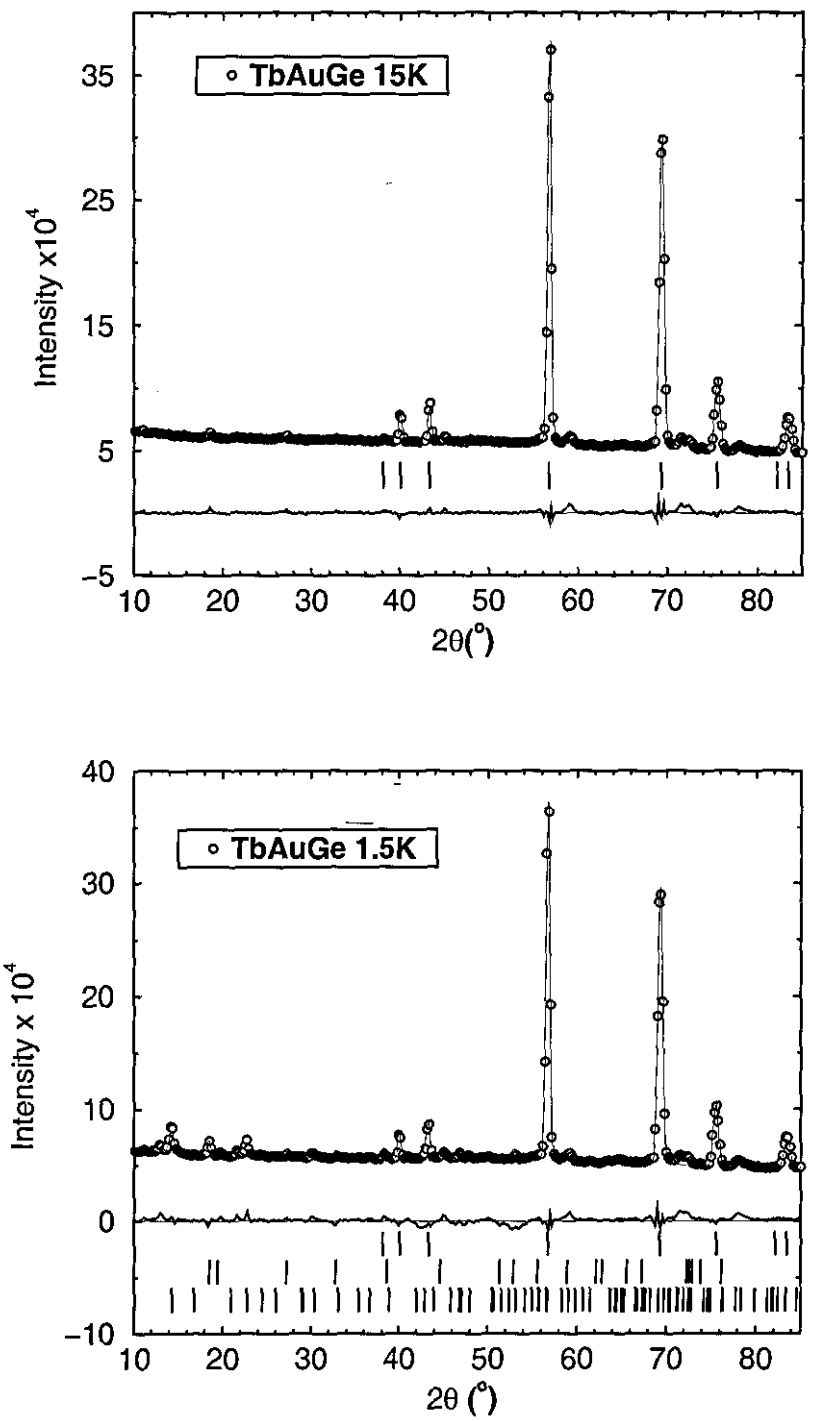

Figure 7.3: Neutron powder diffraction patterns of TbAuGe taken at 15K (top) and 1.5K (bottom). The open circles are the experimental data and the full line is the Rietveld fit to this data. The difference pattern, and also the peak positions are shown beneath the data. The uppermost vertical bars correspond to the nuclear peaks, and the middle and lower vertical bars are the peaks arising from the commensurate and incommensurate magnetic phases, respectively.

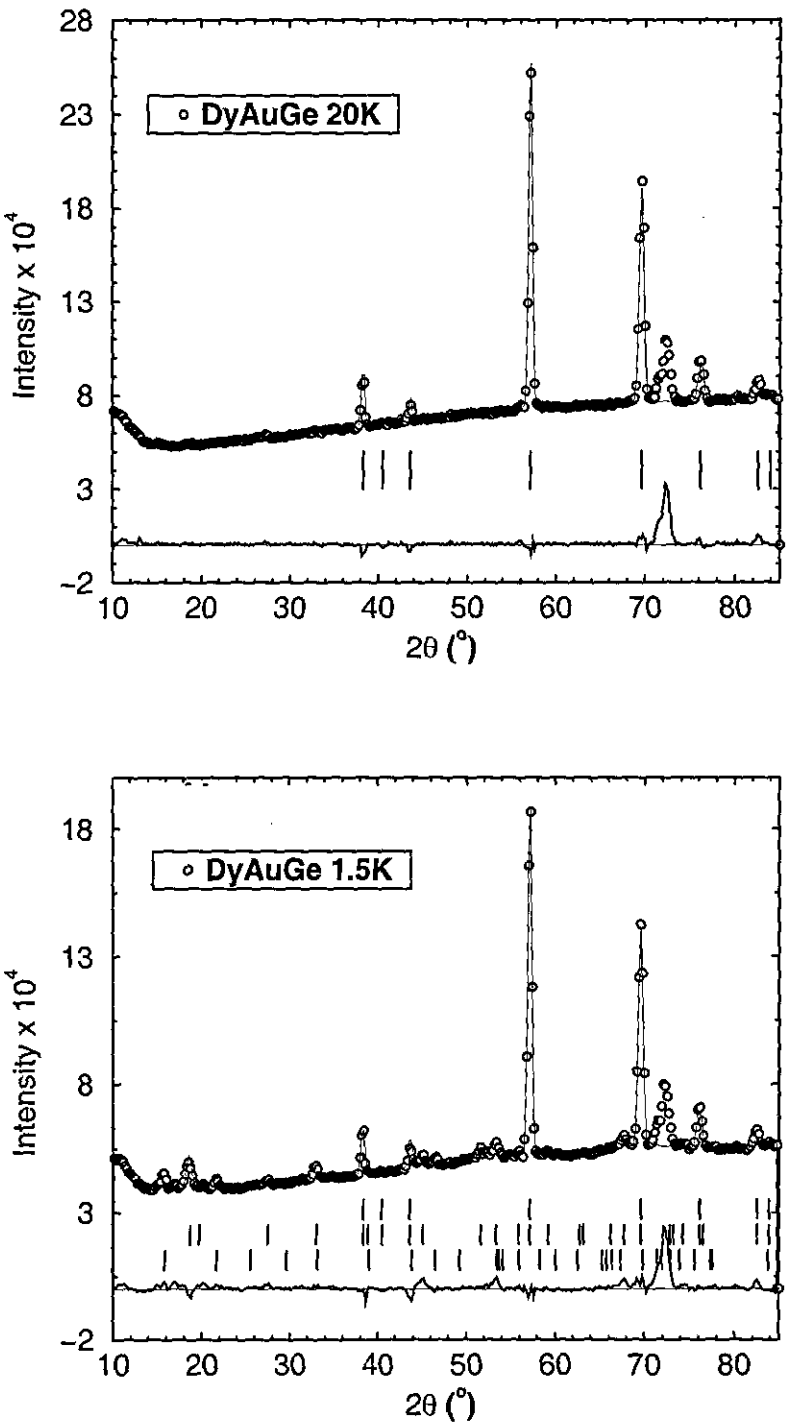

Figure 7.4: Neutron powder diffraction patterns of DyAuGe taken at 20K (top) and 1.5K (bottom). The open circles are the experimental data and the full line is the Rietveld fit to this data. The difference pattern, and also the peak positions are shown beneath the data. The uppermost vertical bars correspond to the nuclear peaks, and the middle and lower vertical bars are the peaks arising from the commensurate and incommensurate magnetic phases, respectively.

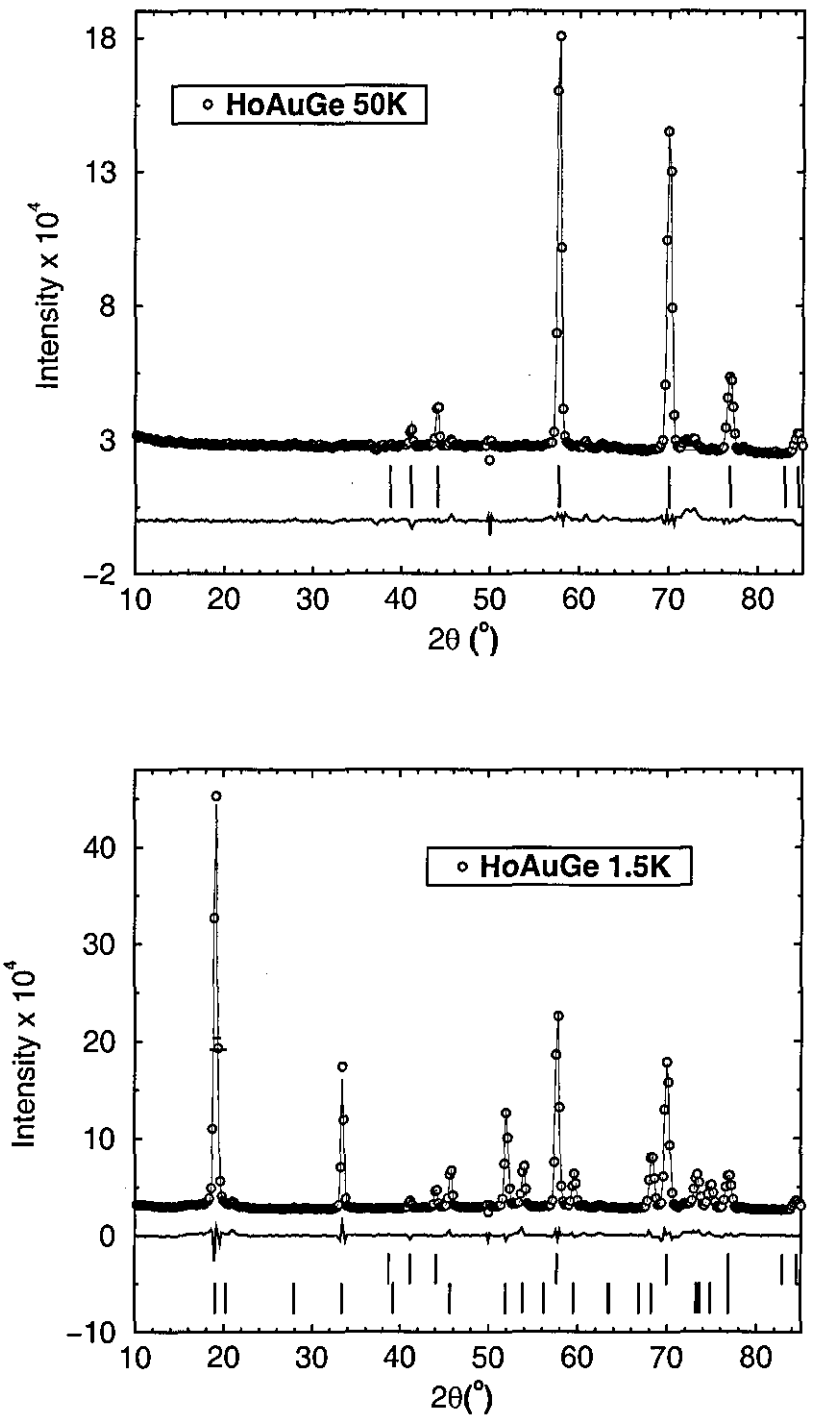

Figure 7.5: Neutron powder diffraction patterns of HoAuGe taken at 50K (top) and 1.5K (bottom). The open circles are the experimental data and the full line is the Rietveld fit to this data. The difference pattern, and also the peak positions are shown beneath the data. The uppermost vertical bars correspond to the nuclear peaks, and the lower vertical bars represent the peaks arising from the commensurate magnetic phase.

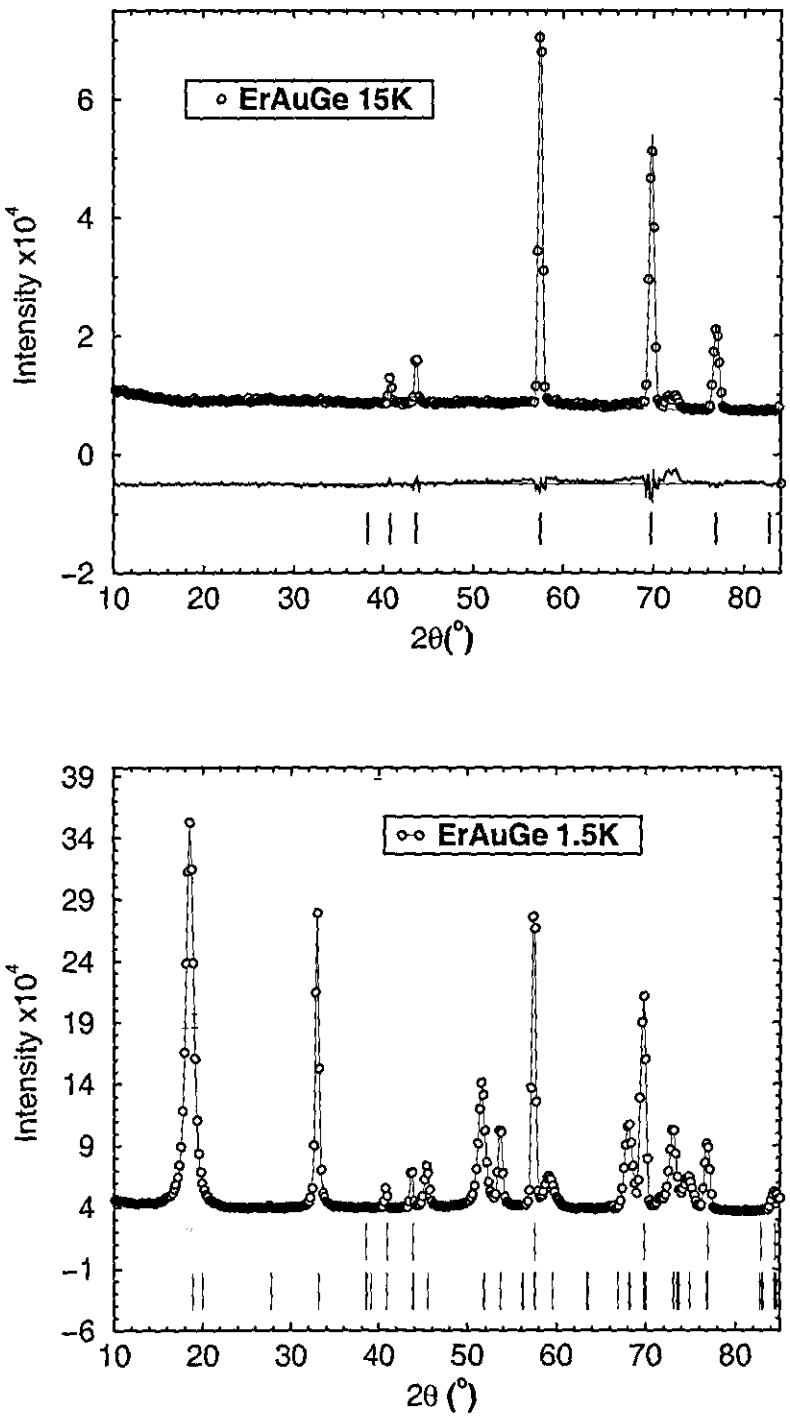

Figure 7.6: Neutron powder diffraction patterns of ErAuGe taken at 15K (top) and 1.5K (bottom). The open circles are the experimental data and the full line is the Rietveld fit to this data (upper panel only). The uppermost vertical bars correspond to the nuclear peaks, and the lower vertical bars represent the peaks arising from the commensurate magnetic phase.

Table 7.1: Lattice constants, atomic coordinates, and isotropic displacement parameters (pm^2) for TbAuGe, DyAuGe, HoAuGe, and ErAuGe at the temperatures indicated. U_{eq} is defined as one third of the trace of the orthogonalised U_{ij} tensor, and is held fixed.

Atom	Wyck. site	x	y	z	U_{eq} (pm^2)	Atom	Wyck. site	x	y	z	U_{eq} (pm^2)
TbAuGe neutron powder data at 15K						*HoAuGe neutron powder data at 50K*					
a=4.4081Å, c=7.2773Å						a=4.4026Å, c=7.2044Å					
Tb	2a	0	0	0.97195	60	Ho	2a	0	0	0.96272	60
Au	2b	1/3	2/3	0.2500[b]	60	Au	2b	1/3	2/3	0.2500[b]	60
Ge	2b	1/3	2/3	0.67736	60	Ge	2b	1/3	2/3	0.67021	60
DyAuGe neutron powder data at 20K						*ErAuGe neutron powder data at 15K*					
a=4.3973Å, c=7.2255Å						a=4.3850Å, c=7.1471Å					
Dy	2a	0	0	0.96094	60	Er	2a	0	0	0.94819	60
Au	2b	1/3	2/3	0.2500[b]	60	Au	2b	1/3	2/3	0.2500[b]	60
Ge	2b	1/3	2/3	0.64740	60	Ge	2b	1/3	2/3	0.66239	60

[b] Fixed parameter.

accessible. The information provided by the diffraction patterns is not sufficient for a full Rietveld refinement of the nuclear structure to be carried out, so the compounds are all assumed to have the same ternary ordered $CaIn_2$ derived structure that is observed from the room temperature single crystal and powder diffraction measurements (see chapter 4 and appendix A).

The compounds are refined using the Rietveld method on the program *Fullprof*, assuming the lattice parameters and atomic positions are allowed to vary only slightly from their room temperature values. The atomic displacement parameters are fixed at constant values. The peaks are fitted assuming a Pseudo-Voigt line shape, which is a mixture of both Gaussian and Lorentzian line-shapes.

The results of the Rietveld refinements are shown in figures 7.3 - 7.6 by the full lines through the experimental points, and the positions of the Bragg reflections are marked by vertical

lines. From the figures, two additional peaks are observed situated around $2\theta \approx 72°$, and are seen to be of varying intensity depending on the compound. These are ascribed to a small unidentified impurity phase in the samples, which is however unobserved in the Guinier X-Ray diffraction patterns. The amount of the impurity phase is seen to be only significant for DyAuGe (figure 7.4).

The results of the refinements, with the region $70.5° < 2\theta < 74°$ excluded for each compound, are summarised in table 7.1. The goodness of fit parameters, as defined in section 6.2 are less than $R_{wp} = 4\%$ and $\chi^2 = 30$, which prove the possibility that the room temperature and low temperature ($T \approx 20$K) nuclear structures remain constant. The only differences that can be observed are small contractions in the unit cell volumes as the compounds are cooled towards low temperatures. However, from the diffraction diagrams themselves it is not possible to rule out the existence of disorder among the Au and Ge sites (as the diffraction patterns can be equally well refined using the space group $P6_3/mmc$ with a random occupation of the Au/Ge sites) as already discussed in chapter 3, and this fact must be kept in mind for the magnetic structure refinements.

7.3.2 Magnetic Structures

The neutron diffraction patterns recorded at the lowest possible temperatures ($T \approx 1.5$K) are shown in figures 7.3 - 7.6(lower panels) for TbAuGe, DyAuGe, HoAuGe, and ErAuGe, respectively, where the measurements are taken in the same 2θ range used for the nuclear structure determination.

In addition to the eight diffraction peaks corresponding to the nuclear reflections, several additional peaks are observed for each compound which may be attributed to coherent magnetic scattering. It is also observed that no magnetic peaks occur below $2\theta = 10°$, so the region below this is excluded due to the large background 'hump' that builds up towards small angles. The region $70.5° < 2\theta < 74°$, which contains the two observed impurity peaks is also excluded from all the refinements.

The peaks arising from nuclear interactions are refined assuming that the crystal structures

of the compounds at $T = 1.5$K are identical to those calculated in the previous section at temperatures just above T_N. That is, the lattice parameters, atomic positions, and line-shapes, are kept at constant values in all subsequent refinements.

From an inspection of the diffraction patterns at $T = 1.5$K, the magnetic peak positions and intensities appear to be similar for TbAuGe and DyAuGe on the one hand, and HoAuGe and ErAuGe on the other: The magnetic peaks in the diffraction diagrams of HoAuGe and ErAuGe are observed to be much larger than the peaks in the TbAuGe and DyAuGe, and are situated at different 2θ positions. Therefore, in the following sections, the magnetic refinements of HoAuGe and ErAuGe are treated separately first, followed by the magnetic refinements of TbAuGe and DyAuGe. The temperature dependence of the magnetic structures are first considered after the $T = 1.5$K diffraction patterns have been clarified.

HoAuGe and ErAuGe

The propagation vectors which describe the magnetic structures of HoAuGe and ErAuGe are identified using the trial and error method of systematically testing all common propagation vectors individually. Both HoAuGe and ErAuGe can be described using the same propagation vector, as is observed from the identical positions (within the limits of their different crystallographic lattice constants) of their magnetic peaks. It is found that they can be well described on the basis of a $\tau = [1/2, 0, 0]$ propagation vector, that is, with a magnetic unit cell having the same dimensions as the crystallographic unit cell, but doubled along the a-axis. The positions indexed as magnetic peaks are shown in figures 7.5 and 7.6 (lower panels) by the lower sets of vertical lines for HoAuGe and ErAuGe, respectively.

It is assumed on the basis of the susceptibility measurements discussed in chapter 4 that the full magnetic moment is localised on the rare-earth ions. In this case the full set of permissible magnetic couplings that is consistent with the $\tau = [1/2, 0, 0]$ propagation vector and the underlying $P6_3mc$ crystal symmetry can be calculated using a method that utilises group theoretical techniques known as representation analysis. This method was

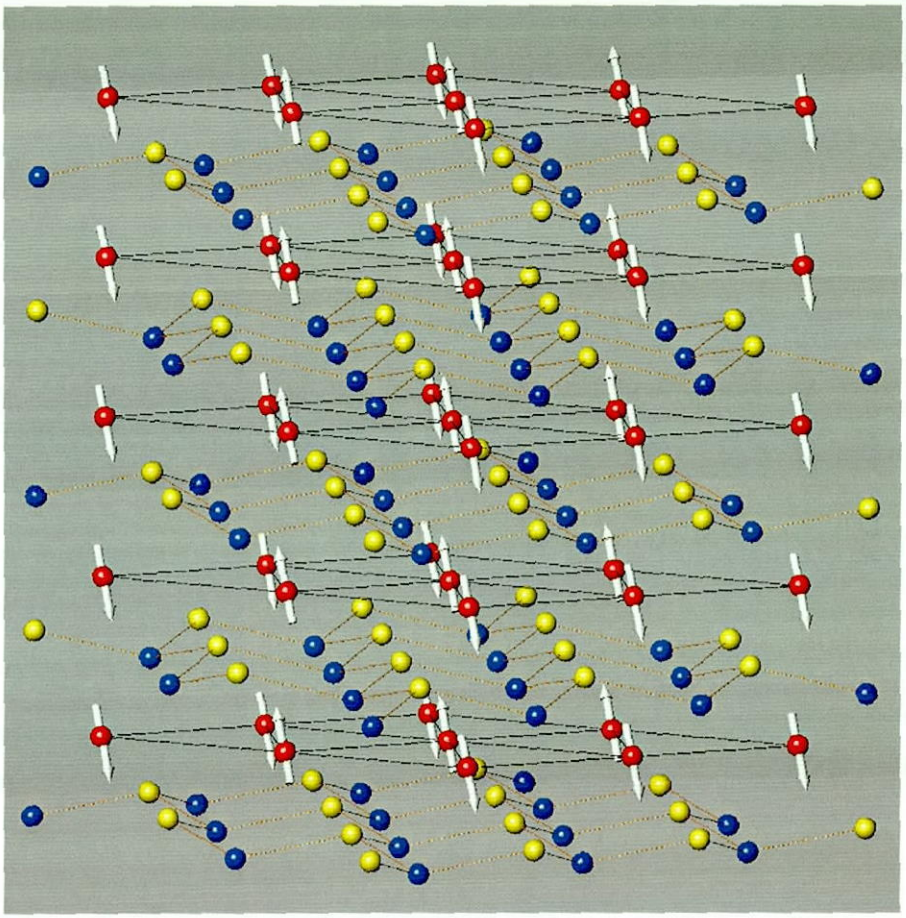

Figure 7.7: Magnetic structure of HoAuGe at $T = 1.5$K, having a propagation vector, $\tau = [1/2, 0, 0]$. Ho, Au, and Ge atoms are represented as red, gold, and blue spheres, respectively. The solid arrows represent the Ho magnetic moments.

first proposed by Bertaut [81, 82], and is described more detail in Appendix C using the HoAuGe/ErAuGe case as an explicit example.

The results of the representation analysis reveal four possible magnetic couplings which are compatible with the underlying crystal symmetry, space group $P6_3mc$, and propagation vector, $\tau = [1/2, 0, 0]$. These are labelled $\Gamma_1, \Gamma_2, \Gamma_3, \Gamma_4$. In Appendix C it is proven that Γ_1 corresponds to an arrangement in which the magnetic moments are coupled antiferromagnetically along the b- and c-axes, and ferromagnetically along the a-axis. Γ_2 and Γ_4 correspond to identical ferromagnetic arrangements with the magnetic moments lying

exclusively along the a-axis. Γ_3 corresponds to antiferromagnetic coupling along the a-axis, with ferromagnetic coupling along b and c.

Each possible magnetic structure is tested in turn, and it is observed that the only solution consistent with the data is the Γ_3 mode. Since this is a one-dimensional representation, the magnetic couplings may be classified using the Shubnikov notation [83] as $Pmc'2'_1$. The corresponding full magnetic structure of HoAuGe is displayed as an example in figure 7.7. The diffraction pattern of ErAuGe at $T = 1.5$K is shown in the lower panel of figure 7.6. The magnetic diffraction peaks occur at very similar positions as for HoAuGe as are marked by the lower set of vertical bars, indicating that the magnetic structure can be described by the same simple commensurate $\tau = [1/2, 0, 0]$ propagation vector. However, a very large amount of peak broadening is observed for the magnetic reflections when compared to the equivalent HoAuGe diffraction pattern, and it is found that the peaks cannot be satisfactorily fitted using Gaussian, Lorentzian, or Pseudo-Voigt line-shapes. Therefore, no full refinement of the magnetic structure is presented here. However, using the results of the representation analysis described in Appendix C in conjuction with the bulk magnetic measurements described in chapter 4, it is assumed that the magnetic coupling between Er atoms is in either the antiferromagnetic Γ_1 or Γ_3 mode, with the magnitude of the magnetic moments having approximately the full $g_J \cdot J = 9\mu_B$ saturated value.

The very broad magnetic peaks observed for ErAuGe could be accounted for by thermal, or more probably at low temperatures, magnetic disorder on the Er atomic sites. It is likely that such disorder might arise from a random arrangement of Au and Ge atoms on the Au/Ge atomic sites as already conjectured in the previous section. Although such a random distribution cannot be proved or disproved from the diffraction patterns, such a structure could possibly alter the magnetic coupling between the Er atoms significantly due to, e.g. the random CEF felt at each magnetic site.

If a random arrangement of Au/Ge atoms within the puckered layers is assumed, the symmetry of the nuclear structure is reduced to $P6_3/mmc$. However, this group also contains the four symmetry elements, E, 2, m_{2xx}, and c_{yz}, of $P6_3mc$ that are consistent with $\tau = [1/2, 0, 0]$. Therefore, the four coupling modes, $\Gamma_1 - \Gamma_4$, of the magnetic moments are

still applicable to this disordered structure.

TbAuGe and DyAuGe

The diffraction patterns of TbAuGe and DyAuGe at $T = 1.5$K are shown in figures 7.3 and 7.4 (bottom). It is observed that magnetic reflections occur in both compounds at positions corresponding to the $\tau = [1/2, 0, 0]$ propagation vector previously discovered in the HoAuGe and ErAuGe compounds. However, two major differences are observed.
Firstly, the intensities of the magnetic peaks observed in the TbAuGe and DyAuGe diffraction patterns are significantly reduced compared to their HoAuGe and ErAuGe counterparts. According to magnetic neutron scattering theory, the magnetic peak intensity is proportional to the square of the magnetic moment (see for example Squires [84]). Since the magnetic moments for Tb, Dy, Ho, and Er ions are similar in magnitude, it is concluded that the magnetic moments of Tb and Dy in these compounds are far from saturated. This has to be attributed to large CEF effects within these compounds.
Secondly, pairs of satellite peaks are observed to flank all of the $\tau = [1/2, 0, 0]$ magnetic peaks in the TbAuGe and DyAuGe diffraction patterns, indicating the existence of incommensurate structures within these compounds.
It is found, again using trial and error methods, that TbAuGe and DyAuGe can be best indexed on the basis of two separate propagation vectors:

- $\tau_1 = [1/2, 0, 0]$. This commensurate propagation vector corresponds to the propagation vector calculated from the HoAuGe and ErAuGe diffraction patterns.
- $\tau_2 = [0, \tau_y, 0]$. This is an incommensurate propagation vector, and accounts well for the observed satellite peaks. τ_y is found to take values of 0.39 and 0.42 for TbAuGe and DyAuGe, respectively.

The magnetic moment oscillating according to τ_1 is confined to lie along the c-axis, and the magnetic moment oscillations of τ_2 are confined to the a-axis. The resulting *amplitude*

Table 7.2: Results of the magnetic Rietveld refinements of TbAuGe, DyAuGe, HoAuGe, and ErAuGe at $T = 1.5$K. The magnetic moments $\mu_{x,exp}(RE)$ and $\mu_{z,exp}(RE)$ are aligned parallel to the a- and c-axis, respectively. The corresponding total experimental value, $\mu_{exp}(RE)$, is compared to the theoretical value, $\mu_S(RE^{3+}) = g_J.J\mu_B$. The magnetic moments of the two RE sites are constrained to be equal by symmetry.

	τ	$\mu_{x,exp}(RE)$	$\mu_{z,exp}(RE)$	$\mu_{exp}(RE)$	$\mu_S(RE^{3+})$	R_M
			(μ_B)			%
TbAuGe	[1/2,0,0]+[0,0.39,0]	2.24	1.06	2.48	9	17.9
DyAuGe	[1/2,0,0]+[0,0.42,0]	2.23	1.95	2.96	10	21.4
HoAuGe	[1/2,0,0]	2.12	6.55	6.88	10	2.6
ErAuGe	[1/2,0,0]	-	-	-	9	-

modulated magnetic structure can be described as the superposition of two sine waves, one having a magnetic moment amplitude equal to m_1 and the other having an amplitude of m_2, and with the periodicity of the propagation vector, τ_1 or τ_2. In this particular case m_1 is observed to be equivalent to (0,0,μ_z) from table 7.2, and $\vec{m}_2 = (\mu_x, 0, 0)$. The resulting magnetic structure is incommensurate to the underlying crystal lattice as is described by the general formula

$$\vec{m}(RE) = \vec{m}_1.exp(2\pi i\vec{\tau}_1 \cdot \vec{r}) + \vec{m}_2.exp(2\pi i\vec{\tau}_2 \cdot \vec{r}) \tag{7.1}$$

where $\vec{m}(RE)$ is the total magnetic moment on a particular rare-earth site, $\vec{m}_1$ and $\vec{m}_2$ are moment contributions from each propagation vector, $\vec{\tau}_1$ and $\vec{\tau}_2$, and $\vec{r} = n_1\vec{a} + n_2\vec{b} + n_3\vec{c}$ is a rare-earth atomic position. Since $\tau_1 = [1/2, 0, 0]$ then

$$\vec{\tau}_1.\vec{r} = \frac{n_1}{2} \tag{7.2}$$

and equation 7.1 reduces to

$$\vec{m}(RE) = \vec{m}_1(-1)^{n_1} + \vec{m}_2.exp(2\pi i\vec{\tau}_2 \cdot \vec{r}) \tag{7.3}$$

where $\vec{m}_1(-1)^{n_1}$ has a magnitude of m_1 at the n_1^{th} RE site when n_1 is even, and $-m_1$ at the n_1^{th} RE sites when n_1 is odd.

This structure is depicted graphically as projected onto the ac-plane in figure 7.8. The dots represent the RE atomic sites. The z component of the magnetic moment propagates along the a-axis commensurately with the crystallographic lattice, and is represented in the diagram by the two vertical arrows, one up and one down on each RE atom. The x component propagates along the b-axis with the long commensurate propagation vector $\tau_2 = [0, \tau_y, 0]$ with the values of τ_y being given in tables 7.2 and 7.3 for the various compounds. As one moves along the b-axis from RE site (1) through to RE site (5), the z component remains constant, but the x component oscillates sinusoidally with a periodicity that is the inverse of the propagation vector. In this way an incommensurate magnetic structure is build up, as is especially clear when, for example, the propagation along the ab direction is considered.

The results of the magnetic refinements of TbAuGe and DyAuGe are summarised in table 7.2, where the resultant magnetic moment of the Tb and Dy atoms are seen to be much reduced compared to their full saturated values.

Temperature dependence of the magnetic structures of HoAuGe and ErAuGe

From the susceptibility measurements described in chapter 4 it is seen that anomalies in the susceptibility are observed for HoAuGe and ErAuGe at several temperatures below T_N. These occur at $\approx$ 4K and $\approx$ 2K for HoAuGe and at $\approx$ 3.5K for ErAuGe. In order to look for any changes in the magnetic structures that may correspond to these anomalies, additional diffraction patterns are recorded for both HoAuGe and ErAuGe at various temperatures between T = 1.5K and T_N. The magnetic diffraction patterns of HoAuGe at 1.3K, 2.9K, 4.9K, and 6.9K are plotted in figure 7.9. ErAuGe is not shown again as the diffraction patterns are qualitatively the same as for HoAuGe, but with the same increased linewidth previously observed in the T = 1.5K pattern.

From figure 7.9, a gradual change in magnetic structure is observed for HoAuGe (and also

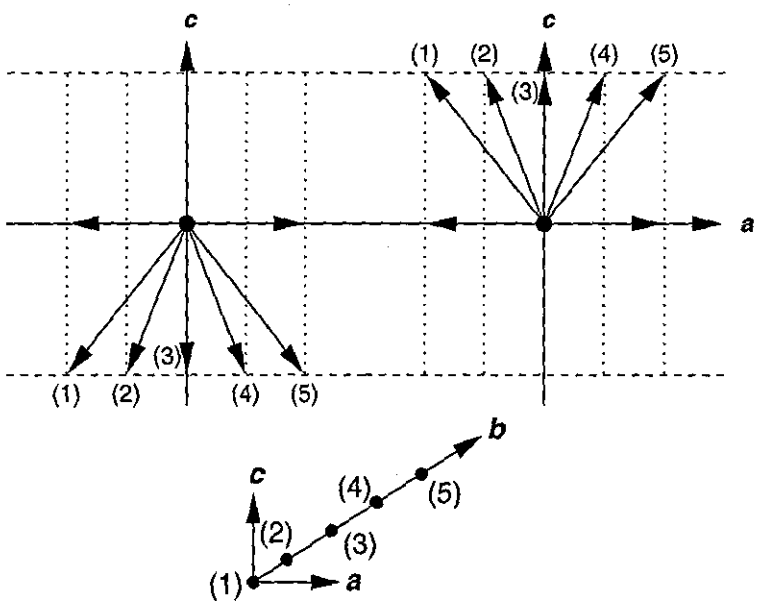

Figure 7.8: Schematic representation of the incommensurate magnetic structure found in REAuGe as composed from the two sine-modulated propagation vectors, $\tau_1 = [1/2, 0, 0]$ and $\tau_2 = [0, \tau_y, 0]$ described in the text.

for ErAuGe) as the temperature is increased from $T = 1.5$K to T_N. The magnetic structure is seen to be commensurate at $T = 1.5$K, as already discussed in the previous sections. At $T = 2.9$K the magnetic structure has already changed, and has a form very similar to the incommensurate structures refined for TbAuGe and DyAuGe at $T = 1.5$K. As the temperature increases through $T = 4.9$K the magnetic structure remains incommensurate, with the intensities of the magnetic peaks decreasing until they dissappear completely at T_N. Unfortunately, more diffraction patterns at intermediate temperatures are not recorded due to the limited amount of beamtime available for this experiment. However, a clear change in the magnetic structure from commensurate to incommensurate type is evident between $T = 1.5$K and $T = 2.9$K that could well account for at least the $T = 2$K anomaly in the susceptibility measurements, although the reason for the anomaly at $T = 4$K remains unclear.

The results of the magnetic refinements of HoAuGe at T= 1.3K, 2.9K, 4.9K, and 6.9K are summarised in table 7.3.

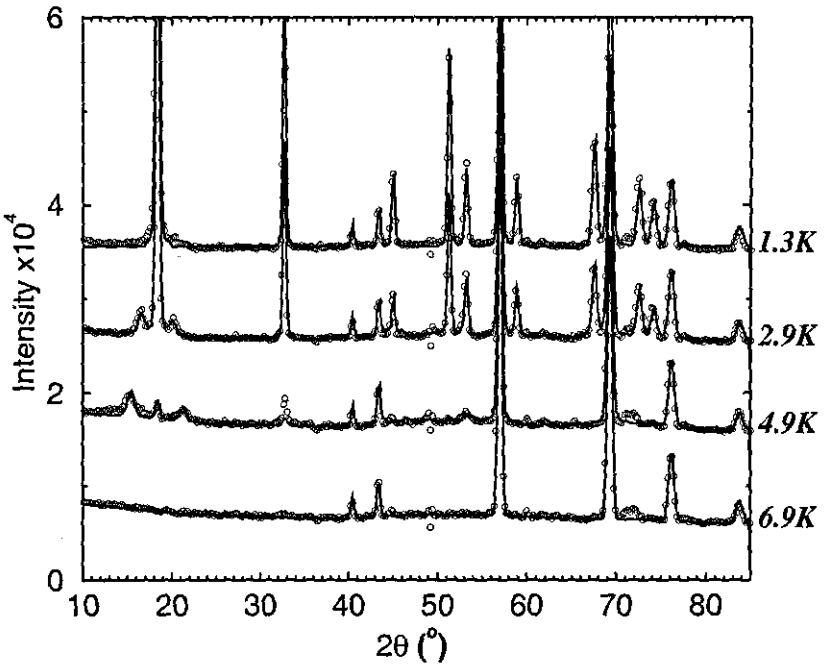

Figure 7.9: Neutron powder diffraction patterns of HoAuGe taken at (from top to bottom) 1.3K, 2.9K, 4.9K, and 6.9K. The open circles are the experimental data and the full lines are the Rietveld fit to this data.

7.3.3 Discussion

A general trend is observed in all the isostructural compounds, TbAuGe, DyAuGe, HoAuGe, and ErAuGe. In all four compounds the same amplitude modulated incommensurate structure is observed close to T_N. As the temperature is lowered further, the magnitude of the magnetic moments increase until, in the case of HoAuGe and ErAuGe, a simple antiferromagnetic structure with $\tau = [1/2, 0, 0]$ is achieved. On the evidence of HoAuGe and ErAuGe, it is assumed that similar commensurate structures will be revealed in TbAuGe and DyAuGe if the temperature is lowered far enough.

The tendency of a magnetic structure to change towards a commensurate structure at low temperatures has been observed previously in several other intermetallic compounds, and in particular, a theoretical model has been proposed by Gignoux et al. [85] who show that,

Table 7.3: Results of the magnetic Rietveld refinements of HoAuGe at T=2.9K and 4.9K.

Temp. (K)	τ	$\mu_{x,exp}(RE)$	$\mu_{z,exp}(RE)$	$\mu_{exp}(RE)$ (μ_B)	$\mu_S(RE^{3+})$	R_M %
2.9	[1/2,0,0]+[0,0.45,0]	3.14	5.85	3.96	10	23.1
4.9	[1/2,0,0]+[0,0.42,0]	3.21	1.27	3.45	10	31.4

on the basis of free energy considerations, only simple commensurate magnetic structures are stable as $T \rightarrow 0$K.

Interestingly, the theory is also relevant for the application of external fields on a sample, and predicts the same change towards an incommensurate structure as the field strength is increased (up to the saturated ferromagnetic state that is always obtained if the field is high enough). Therefore, the meta-magnetic transitions observed in the magnetisation measurements of HoAuGe and ErAuGe (figures 4.9 and 4.11) could well indicate changes in the magnetic structures equivalent to the incommensurate magnetic structures that appear as $T \rightarrow T_N$. Measurements on single crystals of e.g. HoAuGe or ErAuGe in magnetic fields could be useful for future studies in order to follow up in detail the exact changes that occur in the magnetic structures.

7.4 Heavy Rare-Earth Silver Germanides

7.4.1 Nuclear Structures

Diffraction patterns of the two compounds, DyAgGe and HoAgGe, are presented in figures 7.10 and 7.11 at temperatures of $T = 30$K (DyAgGe) and $T = 20$K (HoAgGe) in the upper portions, and at $T = 1.5$K in the lower portions. The measurements on DyAgGe are made using the diffractometer D1B, in the angular range, $5° < 2\theta < 85°$. HoAgGe is measured on the diffractometer, D20, in the angular range $5° < 2\theta < 135°$. TbAgGe and ErAgGe are both left out of this study due partly to the magnetic impurities that are observed in

Table 7.4: Lattice constants, atomic coordinates, and isotropic displacement parameters (pm^2) for DyAgGe and HoAgGe at the temperatures shown. U_{eq} is defined as one third of the trace of the orthogonalised U_{ij} tensor, and is held fixed.

Atom	Wyck. site	x	y	z	U_{eq} (Å)	Atom	Wyck. site	x	y	z	U_{eq} (Å)
DyAgGe neutron powder data 30K						*HoAgGe neutron powder data 20K*					
a=7.0947Å, c=4.1933Å						a=7.0355Å, c=4.1559Å					
Dy	3f	0.58155	0	0	60	Ho	3f	0.58345	0	0	60
Ag	3g	0.23287	0	0.5	60	Ag	3g	0.24982	0	0.5	60
Ge	2d	1/3	2/3	0.5	60	Ge	2d	1/3	2/3	0.5	60
Ge	1a	0	2/3	0	60	Ge	1a	0	0	0	60

the susceptibility measurements of TbAgGe, and which persist in all bulk preparations of the compound, and also due to the limited amount of measurement time available on the diffractometers.

For both compounds the nuclear structures are determined using the results of single crystal and powder X-Ray diffraction (see chapter 3) as starting parameters. In the case of the measurements performed for DyAgGe on the low resolution instrument, D1B, a total of 12 nuclear reflection peaks are observed. The nuclear structure at T = 30K is refined freely using the Rietveld method. The final refinement, shown by the full line in figure 7.10, is observed to correspond closely to the room temperature structure. The results of the final neutron diffraction refinements at temperatures just above T_N are tabulated in table 7.4. However, it is observed that phase impurities are present in this compound, as is evident from the unindexed peaks. In both this and the subsequent magnetic refinement the regions of the impurity peaks are excluded from the refinements.

A total of 24 nuclear peaks are found in the diffraction pattern of HoAgGe taken at T = 20K. Again, the nuclear structure is refined freely using the Rietveld method, and

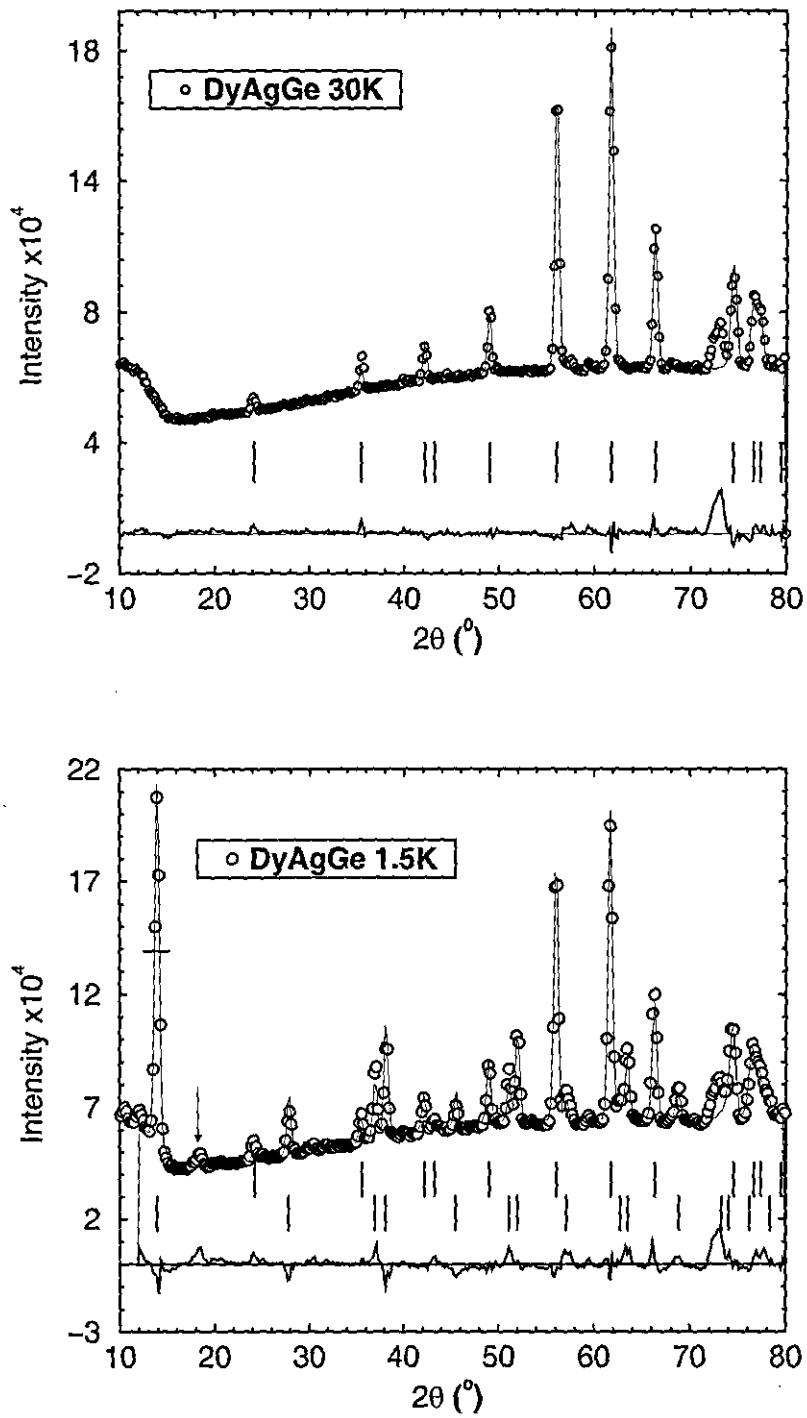

Figure 7.10: Neutron powder diffraction patterns of DyAgGe taken at 30K (top) and 1.5K (bottom) on the diffractometer D1B. The open circles are the experimental data and the full line is the Rietveld fit to this data. The difference pattern, and also the peak positions are shown below. The difference pattern, and also the peak positions are shown beneath the data. The uppermost vertical bars correspond to the nuclear peaks, and the lower vertical bars represent the peaks arising from the magnetic phase.

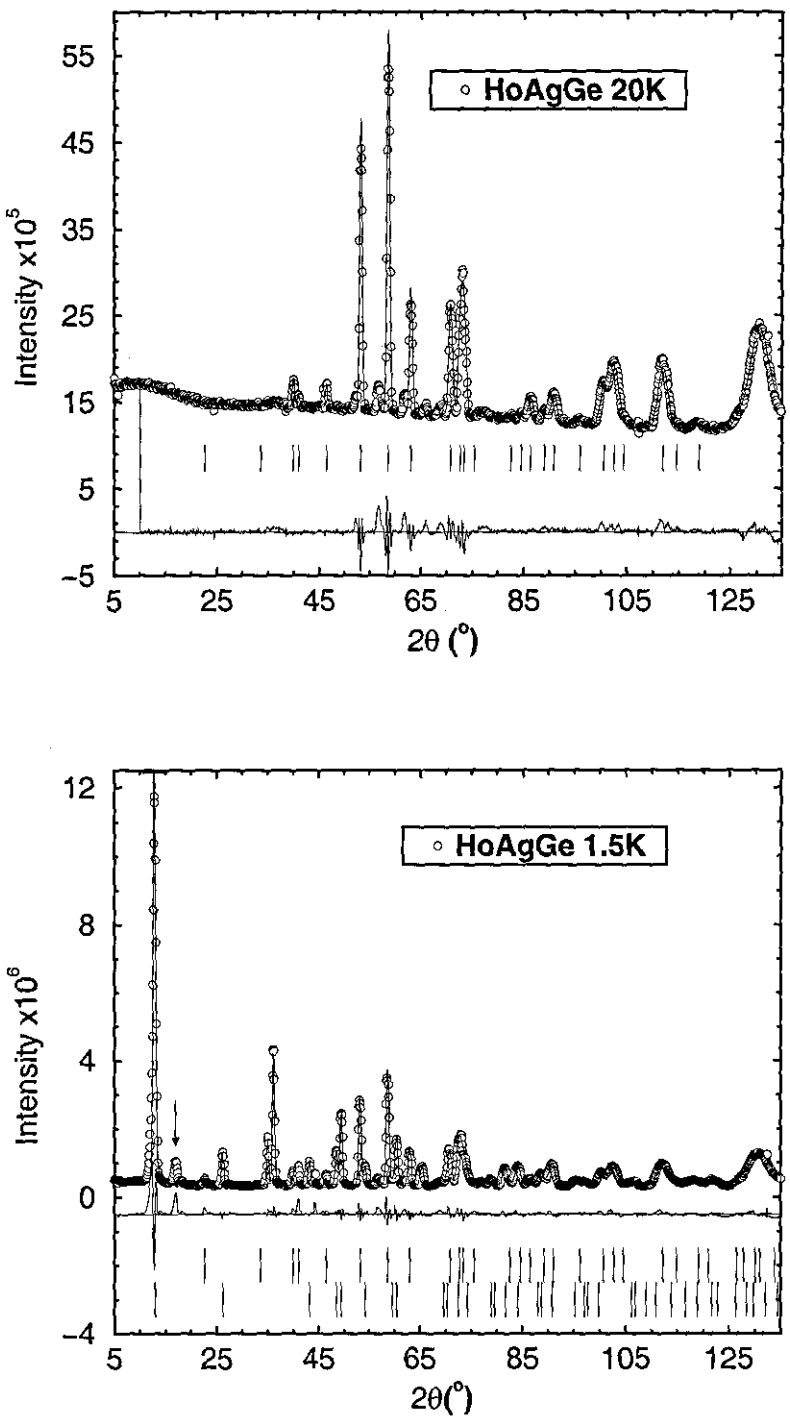

Figure 7.11: Neutron powder diffraction patterns of HoAgGe taken at 20K (top) and 1.5K (bottom) on the diffractometer D20. The open circles are the experimental data and the full line is the Rietveld fit to this data. The difference pattern, and also the peak positions are shown below. The difference pattern, and also the peak positions are shown beneath the data. The uppermost vertical bars correspond to the nuclear peaks, and the lower vertical bars represent the peaks arising from the magnetic scattering.

with the room temperature values as starting parameters. The results of the final refinement of HoAgGe are summarised in table 7.4, and are in good agreement with the room temperature structure but with a small contraction of the lattice parameters. Again, a significant amount of an impurity phase is observed.

The final refinements of both compounds (with the impurity peaks excluded) are better than $R_{wp} = 7\%$ and $\chi^2 = 50$.

7.4.2 Magnetic Structures

The neutron diffraction patterns of DyAgGe and HoAgGe taken at $T = 1.5$K are shown in the lower parts of figures 7.10 and 7.11, respectively. In addition to the nuclear reflections already discussed in the previous section, several additional large peaks resulting from coherent magnetic scattering are observed in each diffraction pattern. The positions of these magnetic peaks are the same for DyAgGe and HoAgGe indicating that they have a similar magnetic structure.

The initial refinements of DyAgGe and HoAgGe at $T = 1.5$K are performed assuming identical atomic positions and lattice parameters determined from the refinements made just above T_N. A fourth order polynomial is used to fit the background, and the same regions containing impurity peaks as identified from the $T > T_N$ refinements are excluded. A total of 15 magnetic peaks in the DyAgGe $T = 1.5$K diffraction pattern (figure 7.10, lower set of vertical lines) and 43 in the HoAgGe diffraction pattern (figure 7.11) can be identified. In both compounds the magnetic peaks are indexed on the basis of a $\tau = [1/3, 1/3, 0]$ propagation vector. However, in both the DyAgGe and HoAgGe diffraction patterns two peaks remain unindexed. These occur at $2\theta = 18°$ for DyAgGe and at $2\theta = 11°$ and $2\theta = 17°$ for HoAgGe, as identified by arrows in the figures. These arise either as magnetic peaks from the phase impurities or are the result of a slight incommensurate deviation from the $\tau = [1/3, 1/3, 0]$ propagation vector. However, in the following $\tau = [1/3, 1/3, 0]$ is assumed as the basis of the magnetic structure model.

In order to refine the magnitude and direction of the magnetic moments on the individual

RE atoms it is in principle possible to calculate the various arrangements of magnetic moments allowable under the crystal symmetry, P$\bar{6}$2m, combined with the propagation vector, $\tau = [1/3, 1/3, 0]$, using representation analysis in a similar way as described in Appendix C for HoAuGe and ErAuGe. However, it is found that all twelve symmetry elements of P$\bar{6}$2m are consistent with $\tau = [1/3, 1/3, 0]$, allowing virtually any arrangement of magnetic moments. The magnetic structure is instead solved by a more direct and intuitive method.

The rare-earth atoms in DyAgGe and HoAgGe are situated at three Wyckoff sites (3*f*) in the unit cell. These are

$$(x, 0, 0), (0, x, 0), (0, -x, -x) \tag{7.4}$$

where x=0.5816 for DyAgGe and x=0.5835 for HoAgGe. The magnetic refinements are then made using the following assumptions:

- The full magnetic moments lie on the RE atoms.
- The magnitude of the magnetic moments are identical on all three RE sites.
- The component of the magnetic moment lying within the *ab*-plane can be freely oriented, but are constrained to have an angle of 120° between consecutive RE atoms.
- The magnetic moment may have a component along the *c*-axis, but this is constrained to be equivalent for all RE atoms.

The refinements are performed using the program *Fullprof* where the magnetic moments are described in terms of polar co-ordinates, and the magnetic scale factor is constrained to be equivalent to the nuclear scale factor in order to obtain meaningful values of the magnetic moment magnitude. Once the magnetic moments are approximately refined, all the quantities; scale factor, lattice parameters, atomic positions, and magnetic moments are allowed to vary freely.

The final magnetic refinements of DyAgGe and HoAgGe are shown by the full lines in

Table 7.5: Results of the magnetic structure refinements of DyAgGe and HoAgGe. μ_{exp} is the magnitude of the magnetic moment, θ is the angle between the magnetic moment and the a-axis in the ab-plane, and ϕ is the angle to the c-axis perpendicular to the ab-plane. R_{wp} is quoted only for the magnetic phase.

Compound	τ	μ_{exp} (μ_B)	θ (°)	ϕ (°)	R_{wp} %	χ^2
DyAgGe	[1/3,1/3,0]	7.3	115(±120)	42	8.1	82
HoAgGe	[1/3,1/3,0]	9.9	105(±120)	≈ 90	6.7	64

figures 7.10 and 7.11, respectively, and the difference between the experimental data and the fits is shown by the full line along the zero x-axis. The final refined magnetic structure of DyAgGe is shown projected onto the ab-plane in figure 7.12 as an example. The magnetic moment magnitudes and directions of DyAgGe and HoAgGe are summarised in table 7.5. The magnetic model used compares very well to the observed data, as is seen from the relatively low magnetic R_{wp} values. Both compounds have very similar magnetic structures. The value of $\mu_{exp} = 9.9\mu_B$ for HoAgGe is very close to the expected value for Ho^{3+} of $g_J \cdot J = 10$.

7.4.3 Discussion

From the results of the magnetic structure refinements of DyAgGe and HoAgGe in the previous section, it is found that both compounds exhibit closely related magnetic structures despite their greatly differing magnetic properties. In the susceptibility measurements detailed in chapter 4, DyAgGe is observed to order ferromagnetically, whereas HoAgGe is an antiferromagnet below T_N. This is explained by the magnetic moment contribution within DyAgGe along the c-axis, leading to a net ferromagnetism along the c-axis. This is not observed in the case of HoAgGe, as the magnetic moments lie entirely in the ab-plane.
In addition to the neutron diffraction patterns taken at $T = 1.5$K and $T > T_N$ described in

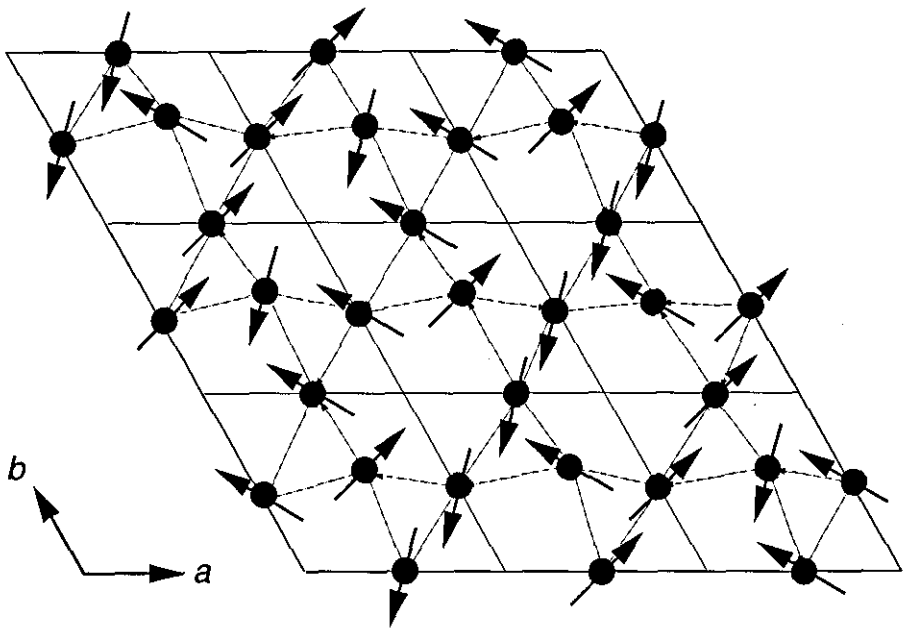

Figure 7.12: Arrangement of magnetic moments for DyAgGe as projected onto the *ab*-plane. Only the Dy atoms within the magnetic unit cell are shown.

this chapter, diffraction patterns are measured at several additional temperatures below T_N for both DyAgGe and HoAgGe. These are not presented here as the diffraction patterns at all temperatures below T_N are identical for the respective compounds, with only a gradual increase in the magnetic peak intensities towards a saturated value as $T \rightarrow 0$K. Therefore, unlike their REAuGe counterparts, no phase changes to incommensurate magnetic structures are observed for DyAgGe and HoAgGe, which is consistent with the absence of anomalies below T_N in their susceptibility and heat capacity measurements.

Chapter 8

Summary and Conclusions

The chemical and physical properties of the two ternary intermetallic rare-earth series of compounds, REAuGe and REAgGe, are investigated within this thesis.

Previous investigations by other groups on REAuGe and REAgGe compounds have concentrated mainly on the determination of their crystal structures [9, 10, 11], and have also provided preliminary information about the magnetic properties of a few of the compounds [12]. However, very little was known about their physical properties in general, and much of the motivation for this work is generated from the possibly of discovering new and interesting physical properties within these compounds.

A wide variety of experimental techniques are employed for this purpose. The structures of all of the compounds are determined, several for the first time, by both powder and single crystal X-Ray diffraction. The magnetic and transport properties are investigated by means of susceptibility, heat capacity, resistivity, and both elastic and inelastic neutron scattering in conjunction with band structure calculations. The high quality of the sample preparation and the precision of the measurements prove to to be essential for the correct evaluation of the measured properties.

The REAuGe and REAgGe compounds crystallise in three distinct structure types depending on the size and oxidation state of the rare-earth and transition ions, and also on the specific temperature and pressure conditions. For the REAuGe compounds a ternary

ordered derivative of the well known $CaIn_2$ structure type is found. The size of the RE atoms strongly affect the amount of puckering within the $[AuGe]_x$ polyanion layers, changing gradually from a 2D layered arrangement of the $[AuGe]_x$ polyanions for the larger RE atoms to a 3D arrangement for the smallest RE atoms. A similar change in structure from a 2D to a 3D polyanion arrangement is observed for CeAuGe under applied pressure. At $P = 8$GPa there is an abrupt phase change to an orthorhombic $CeCu_2$-type structure.

For the REAgGe series of compounds a ternary ordered derivative of the Fe_2P structure type is more thermodynamically stable with the change in structure type possibly a consequence of the smaller Ag atoms. However, for the larger RE atoms, La and Ce, and possibly Pr and Nd, the structure type of REAgGe reverts to the $CaIn_2$ type. Both EuAuGe and EuAgGe crystallise in the tetragonal $CeCu_2$ structure type as consequence of the divalency of the Eu ions.

Investigations on the transport and electronic properties of the non-magnetic REAuGe and REAgGe show the compounds to exhibit metallic behaviour. However, the room temperature electrical resistivities are much higher than typically found in metals, and arises from the quasi-band gap that opens up at E_F as a consequence of the crystal structures. This is particularly pronounced for LaAuGe, but is observed in the band structures of all the REAuGe and (to a lesser extent) REAgGe compounds. The phonon properties of the non-magnetic compounds are analysed in terms of the Debye model, and these values are found invaluable for the determination of the magnetic contributions to the heat capacities of other isostructural compounds.

Despite the broad differences in crystal structure between the REAuGe and REAgGe series, close similarities exist within their magnetic properties. Most of the compounds containing a magnetic RE atomic species order either ferro- or antiferromagnetically at low temperatures. Exceptions are TmAuGe and the unannealed preparation of PrAgGe which do not show magnetic ordering down to $T = 2$K, although they are expected to order below this temperature. YbAuGe exhibits strongly mixed-valent characteristics. No correlation is evident between the measured $T_{N/C}$ and a DeGennes scaling. This suggests that the CEF effects are so pronounced that they change $T_{N/C}$ significantly from the expected values.

This assumption is evidenced by the very large Schottky contributions to the heat capacities, and is analysed in the case of CeAuGe and CeAgGe by inelastic neutron scattering and magnetisation experiments.

As part of this work, the magnetic structures of several of the compounds are determined by elastic neutron diffraction on polycrystalline samples. The results reveal a variety of magnetic structures

- CeAuGe has a ferromagnetic structure below $T_C \approx 10(1)$K as determined from susceptibility measurements on powders. The magnetic moments have a magnitude of $\approx 1\mu_B$ lying approximately along the a-axis. This result is substantiated within this thesis by the various bulk magnetic measurements (on polycrystals and single crystals) which prove the existence of an ab easy plane and a saturated magnetic moment of $1.09(5)\mu_B$/Ce atom.

- CeAgGe has an antiferromagnetic structure below $T_N = 5(1)$K. The magnetic structure is described by a propagation vector, $\tau = [1/3, 0, 0]$, with the magnetic moments of the Ce ions having a magnitude of $\approx 1.6\mu_B$ and oriented within the ab-plane. The magnetic moment is somewhat larger than the saturated magnetic moment derived from the magnetisation measurements of $1.02(5)\mu_B$/Ce atom, although the large inaccuracies in the neutron diffraction results due to the exceptionally small magnetic peaks makes this result acceptable.

- The heavy REAuGe compounds (RE=Tb,Dy,Ho,Er) order antiferromagnetically at various temperatures below $T = 8$K. They show a tendency towards a commensurate $\tau = [1/2, 0, 0]$ magnetic structure at lowest temperatures with the magnetic moments oriented within the bc-plane. Towards T_N the magnetic structures become incommensurate with the underlying crystal lattice, and are described by the sum of two propagation vectors, $\tau = [1/2, 0, 0] + [0, \tau_y, 0]$. Such structure changes are discussed in view of the theoretical predictions based on thermodynamical considerations. They predict a simple commensurate magnetic structure as $T \rightarrow 0$K in

all cases, and changes to incommensurability as the temperature and/or external magnetic field is increased towards T_N. The changes in structure are also evident in the susceptibility and heat capacity, and corresponding metamagnetic transitions are observed in the magnetisation measurements.

- The magnetic structures of two of the heavy REAgGe compounds, DyAgGe and HoAgGe are also determined within this thesis. DyAgGe shows spontaneous magnetisation below $T_C = 14(1)$K whereas HoAgGe is antiferromagnetic below $T_N = 11(1)$K. The magnetic structures of both compounds are nonetheless very similar and may be described by a $\tau = [1/3, 1/3, 0]$ propagation vector with the magnetic moments lying in a frustrated arrangement within the *ab*-plane. However, for DyAgGe, a component of the magnetic moment also lies ferromagnetically coupled along the *c*-axis which gives rise to the observed ferromagnetism. Unlike the heavy REAuGe compounds, no structure changes are evident towards T_N. If they do occur, then they probably only amount to a re-orientation of the frustrated moments within the *ab*-plane.
  While preparing this this Baran et al. [86] have also investigated several magnetic properties of the heavy REAgGe compounds. The results are in good agreement with the results presented within this thesis. Small discrepancies arise in the suggested magnetic structures, in which they propose different orientations of the magnetic moments. These discrepancies could be the result of the ambiguities inherent in powder diffraction measurements. The diffractometer resolution utilised for the measurements presented in this thesis is significantly improved, as is the observed sample purity. These conflicting results demonstrate the strong interest in these types of compounds and highlights the necessity for further measurements on single crystal samples.

Inelastic neutron scattering in conjunction with heat capacity measurements of the isostructural CeAuGe (FM) and CeAgGe (AFM) compounds reveal that the CEF splits the $2J+1$ multiplet into a doublet ground-state and two excited doublets. The energy transfer spectrums for both compounds are qualitatively very similar and show that one of the excited

doublets lies at an energy of $E \approx 25$meV. The second excited state is either very close to $E \approx 25$meV forming a quasi-quadruplet excited state, or lies at higher energies which cannot be determined from the experiments presented. Extension of the inelastic neutron diffraction experiments to a greater energy transfer range are planned to clarify the situation.

Several conclusions regarding the investigations on CeAuGe and CeAgGe are now made

- The CEF environments and excitations in CeAuGe and CeAgGe are observed to be very similar. However the small difference in CEF environments arising from the degrees of puckering in the $[TGe]_x$ polyanion layers is sufficient to align the magnetic moments ferromagnetically for CeAuGe, and re-orient them slightly in CeAgGe to a 'semi-long period' antiferromagnetic arrangement.

- From the heat capacity (and other measurements), no indication of heavy fermion behaviour is observed in either CeAuGe or CeAgGe.

- The behaviour of CeAuGe within the critical region analysed in this thesis suggests that the compound is highly (magnetically) anisotropic, and that the magnetic interactions can be best described using the 3D-Heisenberg model. Furthermore, the Curie temperature is accurately determined to be $T_C = 9.72(3)$K.

In addition, further detailed investigations on CeAuGe are presented within this thesis. Magnetisation measurements on large single crystals performed for the first time show the compound to be highly anisotropic in agreement with the analysis of the measurements performed on polycrystals. Two particular interesting features are observed. The first is an indication of a second possible magnetic transition around $T = 5$K, possibly resulting from a rearrangement of the ferromagnetic domains. The second is the observation of a somewhat reduced $T_C = 9.0(1)$K compared to the the results of the measurements on polycrystals. The anisotropic susceptibilities are fitted to CEF theory. The best fits predict a CEF splitting of the $2J+1$ multiplet into three doublets, at $E_1 = 0$meV, $E_2 = 25$meV and $E_3 = 31$meV which corresponds closely to the previously hypothesised energy level scheme

obtained from the inelastic neutron scattering measurements. Finally, first susceptibility measurements of CeAuGe under applied pressure show an increase of T_C with pressure of $0.11 \cdot 10^{-2}$K/kbar. This increase is associated with a strengthening of the exchange interactions and can be related to the changes of the crystal structure parameters under pressure.

The work to be performed on these series of compounds is by no means complete. Several investigations are currently planned, or could be envisaged for future studies as a result of the findings within this thesis

- *Pressure experiments on CeAuGe and CeAgGe.* It would be extremely interesting to observe whether T_N of CeAgGe increases or decreases under pressure. In addition this could form the basis of elastic neutron scattering experiments under pressure to determine any structural (both nuclear and magnetic) changes.

- *Mixed $CeAu_{1-x}Ag_xGe$ experiments.* These could be performed in order to determine the crossover point between the AFM - FM transition, and to determine which of the exchange interactions is the strongest.

- *Magnetisation density determination of CeAuGe by polarised neutrons.*

- *Magnetic structure determination of the light REAuGe and REAgGe compounds.*

- *Magnetic structure determination of the heavy REAuGe compounds under applied pressure and in external fields.* The theoretical considerations predicting the change from commensurate to incommensurate magnetic structures under increasing pressure or external field should be tested, preferably on single crystal samples.

- *Hall effect of non-magnetic RETGe.* Hall effect measurements should be made to gain a better understanding of the transport properties. In particular it would be interesting to determine the concentration of charge carriers and their mobility as a function of temperature.

Appendix A

Crystallographic Data

A.1 HoAuGe

The X-Ray powder diffraction diagram of HoAuGe, taken using the modified Guinier technique [21], is compared with the theoretically calculated Lazy-Puverix [22] pattern in figure A.1 below.

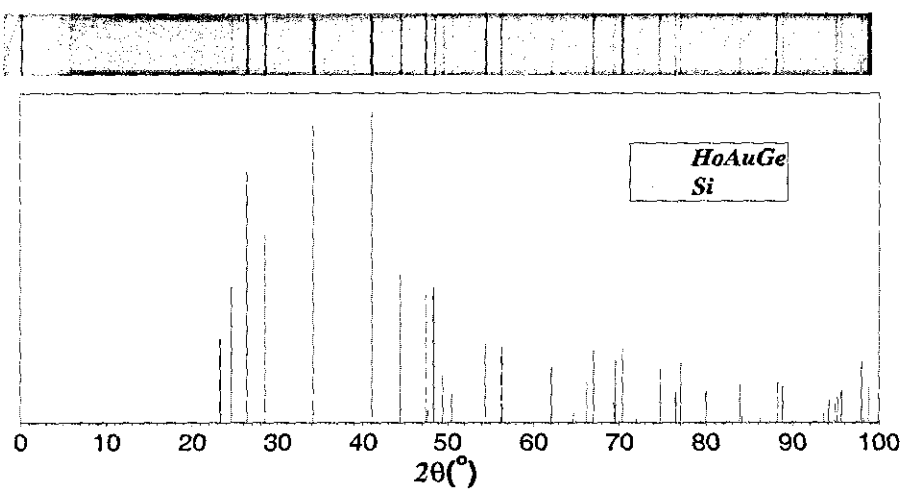

Figure A.1: Comparison of the measured (top) and calculated (bottom) X-Ray powder diffraction diagrams of HoAuGe. In the calculated diagram, Silicon peaks are denoted by the dashed lines.

Details of the structure refinement from single crystal X-Ray diffraction are given in table

A.1. The atomic positions and nearest neighbour distances are presented in table A.1.

A.2 DyAgGe

The X-Ray powder diffraction diagram of DyAgGe, taken using the modified Guinier technique, is compared with the theoretically calculated Lazy-Puverix pattern in figure A.2 below.

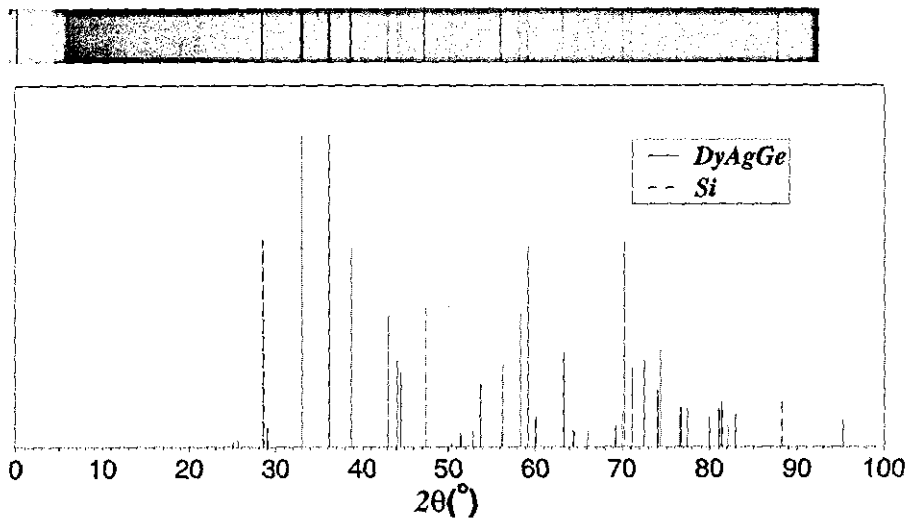

Figure A.2: Comparison of the measured (top) and calculated (bottom) X-Ray diffraction diagrams of DyAgGe. In the calculated diagram, silicon peaks are denoted by the dashed lines.

Details of the structure refinement from single crystal X-Ray diffraction are given in table A.1. The atomic positions and nearest neighbour distances are presented in table A.2.

Table A.1: Crystal data and structure refinement for HoAuGe and DyAgGe [24].

Empirical Formula	HoAuGe	DyAgGe
Formula Weight	434.49 g/mol	342.96 g/mol
Temperature	293(2) K	293(2) K
Wavelength	71.073 pm	56.086 pm
Crystal System	hexagonal	hexagonal
Space group	$P6_3mc$	$P\bar{6}2m$
Unit cell dimensions	a = 440.10(5) pm	a = 710.67(7) pm
(Guinier powder data)	c = 723.26(9) pm	c = 419.73(5) pm
	V = 0.1213(1) nm^3	V = 0.1836(1) nm^3
Formula units per cell	Z = 2	Z = 3
Calculated density	11.89 g/cm^3	9.31 g/cm^3
Crystal size	40 x 30 x 225	35 x 35 x 200
Absorption correction	from Ψ-scan data	from Ψ-scan data
Transmission ratio	1:4.07	1:1.41
Absorption coefficient	104.5 mm^{-1}	26.52 mm^{-1}
F(000)	356	435
Θ range for data collection	5° to 30°	2° to 24°
Scan type	ω / 2Θ	ω / 2Θ
Range in hkl	± 7, ± 7, ± 13	± 10, ± 10, ± 6
Total no. reflections	973	1720
Independent reflections	234(R_{int}) = 0.0879	245(R_{int}) = 0.0439
Refinement method	Full-matrix l-s on F^2	Full-matrix l-s on F^2
Data/restraints/parameters	225/ 0/ 10	245/ 0/ 14
Goodness of fit on F^2	1.111	1.567
Final R indices [I> 2σ(I)]	R1 = 0.0316, wR2 = 0.0610	R1 = 0.0203, wR2 = 0.0463
R indices (all data)	R1 = 0.0366, wR2 = 0.0640	R1 = 0.0203, wR2 = 0.0463
Extinction coefficient	0.016(2)	0.112(6)

Table A.2: Atomic coordinates and isotropic displacement parameters (pm^2) for HoAuGe. U_{eq} is defined as one third of the trace of the orthogonalised U_{ij} tensor.

Atom	Wyckoff site	x	y	z	U_{eq}
X-Ray single crystal data					
Ho	2a	0	0	0.9628(3)	69(2)
Au	2b	1/3	2/3	0.2500[b]	91(3)
Ge	2b	1/3	2/3	0.6705(5)	72(5)

[b] Fixed parameter

Table A.3: Interatomic distances (pm) calculated with the powder lattice constants and the positional parameters of the single crystal data in the structure of HoAuGe. All distances shorter than 565 pm (Ho-Ho), 525 pm (Ho-Au, Ho-Ge), and 415 pm (Au-Au, Au-Ge, Ge-Ge) are listed. Standard deviations are all equal or smaller than 0.3 pm.

Ho : 3 Ge 295.2	Au : 3 Ge 260.5	Ge: 3 Au 260.5
3 Au 297.1	3 Ho 297.1	3 Ho 295.2
3 Au 328.2	1 Ge 304.1	1 Au 304.1
3 Ge 330.6	3 Ho 328.2	3 Ho 330.2
2 Ho 361.6		
6 Ho 440.1		

Table A.4: Atomic coordinates and isotropic displacement parameters (pm^2) for DyAgGe [24]. U_{eq} is defined as one third of the trace of the orthogonalised U_{ij} tensor.

Atom	Wyckoff site	x	y	z	U_{eq}
X-Ray single crystal data					
Dy	3f	0.58268(7)	0	0	73(2)
Ag	3g	0.24925(11)	0	1/2	102(2)
Ge1	2d	1/3	2/3	1/2	71(3)
Ge2	1a	0	0	0	91(3)

Table A.5: Interatomic distances (pm) calculated with the powder lattice constants and the positional parameters of the single crystal data in the structure of DyAgGe [24]. Standard deviations are all equal or smaller than 0.1 pm.

Dy : 1 Ge2 296.6	Ag : 2 Ge1 271.1	Ge1: 3 Ag 271.7	Ge2: 6 Ag 274.6
4 Ge1 299.3	2 Ge2 274.6	6 Dy 299.3	3 Dy 296.6
2 Ag 316.5	2 Ag 306.8		
4 Ag 332.9	2 Dy 316.5		
4 Dy 369.6	4 Dy 332.9		
2 Dy 419.7			

Appendix B

Superconductivity in ScAgGe

In addition to the susceptibility measurements described in chapter 5 using the MPMS SQUID magnetometer, the susceptibilities of the compounds RETGe, where RE = Sc, Y, La, and Lu, and X = Au, Ag, have been measured down to temperatures of $\approx$ 0.3K using a single shot ^{3}He cryostat.

The susceptibility of ScAgGe, m = 177.6mg as a function of temperature between 0.3K and 4K is shown in figure B.1. The abscissa is measured in arbitrary units. From the graph two superconducting transitions are observed; at 3.7(1)K, and at 1.1(1)K. The transition at 3.7(1)K is a result of the experimental setup and arises from small amounts of solder within sample holder. This solder signal provides a good method of calibrating the instrument and a cross calibration of an Al standard sample and the solder signal proves that the diamagnetic shielding of the ScAgGe sample is complete. The isostructural compounds, YAgGe, LaAgGe and LuAgGe show no superconducting transition down to 0.3K, as do Sc-, Y-, La-, and LuAuGe.

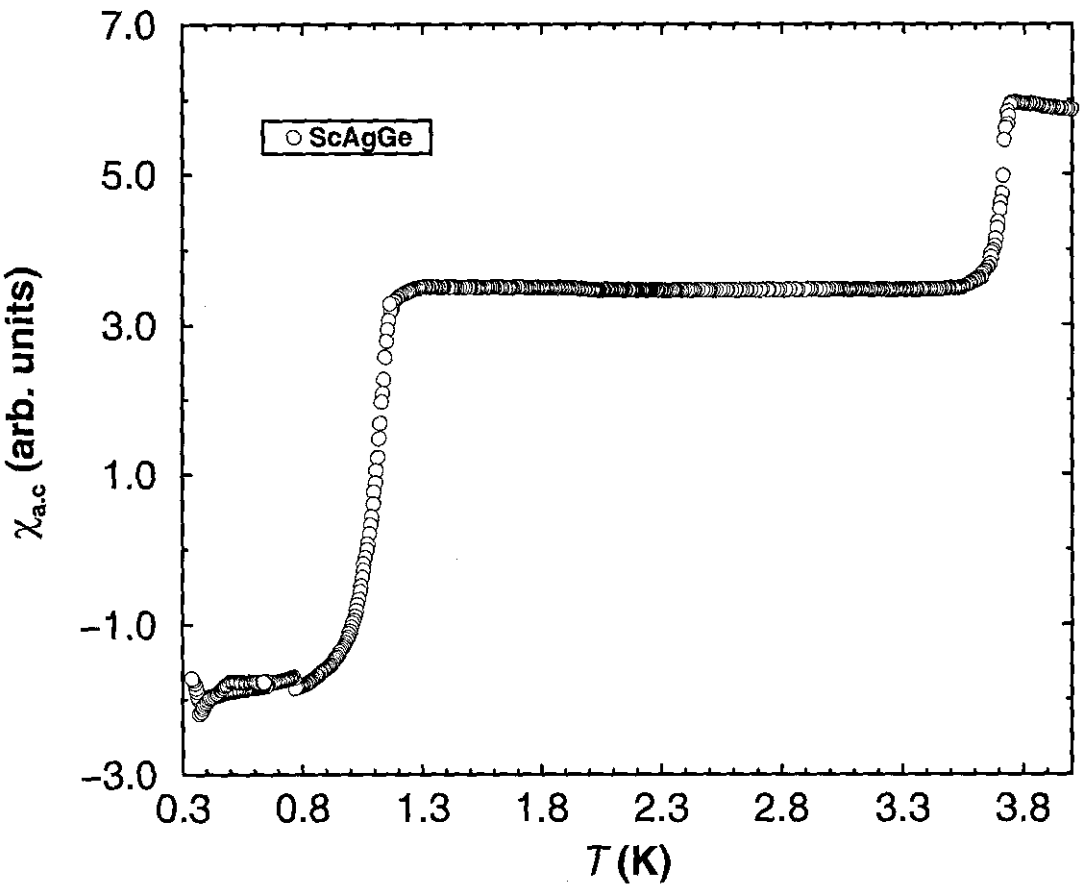

Figure B.1: Low temperature a.c. susceptibility of ScAgGe. The step at 3.7K arises from small amounts of solder in the sample holder, and the step at 1.1K is the superconductivity transition of ScAgGe.

Appendix C

Representation Analysis

In this appendix the representation analysis method that is used for determining all the possible magnetic couplings that are consistent with a given crystallographic space group and propagation vector is examined [81]. The crystal structure and propagation vector observed in the two compounds, HoAuGe and ErAuGe, which are studied in chapter 7 of this thesis, are used as a real example.

The complete determination of any magnetic structure requires (1) a knowledge of the propagation vector, and (2) the coupling, orientation, and magnitude of the Fourier components of the magnetic moments, $\mathbf{m}_{k,j}$. The first step must usually be determined by empirical methods. However, for the second step, group theory can be of enormous help if both the space group and the positions of atomic sites are known, as is demonstrated here. HoAuGe and ErAuGe both crystallise with hexagonal structures described by the space group symmetry $P6_3mc$ (no. 186). This space group consists of 12 elements;

$$G_P = (E, 3^+, 3^-, 2, 6^-, 6^+, m_{x\bar{x}}, m_{x2x}, m_{2xx}, c_{xx}, c_{xz}, c_{yz}) \tag{C.1}$$

The magnetic RE (Ho or Er) atoms are situated on the two Wykcoff $2a$ crystallographic sites (see chapter 3 for a detailed discussion of the crystal structures);

- RE1 - (0,0,z)
- RE2 - (0,0,z+1/2)

At $T = 1.5$K, the magnetic diffraction peaks of HoAuGe and ErAuGe can be indexed using the propagation vector, $\tau = [1/2, 0, 0]$, as is demonstrated in the neutron diffraction patterns of figures 7.5 and 7.6.

Using the methods of representation analysis [81] to determine the magnetic coupling between the RE atoms, the first task is to find out which of the elements of G_P remain invariant under the action of the propagation vector, τ, i.e

$$\beta\tau = \tau + K \tag{C.2}$$

where β is a symmetry element of G_P and K is the reciprocal lattice vector. This is easily calculated using the matrix representations of the symmetry elements, bearing in mind that the propagation vector is described in k-space, which requires transposing the matrix of the symmetry element. The action of the symmetry element 2 is shown as an example:

$$2^T\tau = \begin{pmatrix} \bar{1} & 0 & 0 \\ 0 & \bar{1} & 0 \\ 0 & 0 & 1 \end{pmatrix} \begin{pmatrix} \frac{1}{2} \\ 0 \\ 0 \end{pmatrix} = \begin{pmatrix} \bar{\frac{1}{2}} \\ 0 \\ 0 \end{pmatrix} \equiv [\frac{1}{2}, 0, 0] + [\bar{1}, 0, 0] \Rightarrow 2 \in G_k \tag{C.3}$$

Using the same method for all elements of the space group in turn it is seen that only 4 of the symmetry elements of G_P are consistent with equation C.2. These form a group, $G_k = (E, 2, m_{2xx}, c_{yz})$, which has 4 one-dimensional irreducible representations. The representations are generated from the general equation

$$\sum_{C_g \in G_k} \chi^{\nu}(C_g)\chi^{\nu'}(C_g) = n(G_k)\delta_{\nu\nu'} \tag{C.4}$$

where C_g is an element of G_k, $\chi^{\nu}(C_g)$ is the corresponding trace of the character of C_g, and $n(G_k)$ is the order of G_k. The results are obtained by solving a set of, in this case 9, simultaneous equations and are listed in the *character table* below (table C.1).

Since there are two distinct sites for the RE atoms within the crystallographic unit cell; RE1=[0,0,z] and RE2=[0,0,z+$\frac{1}{2}$], the next step is to consider the transformation properties

Table C.1: Character table showing the irreducible representations of G_k.

	E	2	m_{2xx}	c_{yz}
Γ_1	1	1	1	1
Γ_2	1	1	$\bar{1}$	$\bar{1}$
Γ_3	1	$\bar{1}$	1	$\bar{1}$
Γ_4	1	$\bar{1}$	$\bar{1}$	1

of the symmetry elements on the two sites:

$$E; \begin{pmatrix} 1 & 0 & 0 \\ 0 & 1 & 0 \\ 0 & 0 & 1 \end{pmatrix} \begin{pmatrix} 0 \\ 0 \\ z \end{pmatrix} = \begin{pmatrix} 0 \\ 0 \\ z \end{pmatrix} \Rightarrow RE1 \rightarrow RE1 \ (RE2 \rightarrow RE2) \tag{C.5}$$

$$2; \begin{pmatrix} \bar{1} & 0 & 0 \\ 0 & \bar{1} & 0 \\ 0 & 0 & 1+\frac{1}{2} \end{pmatrix} \begin{pmatrix} 0 \\ 0 \\ z \end{pmatrix} = \begin{pmatrix} 0 \\ 0 \\ z+\frac{1}{2} \end{pmatrix} \Rightarrow RE1 \rightarrow RE2 \ (RE2 \rightarrow RE1) \tag{C.6}$$

$$m_{2xx}; \begin{pmatrix} 1 & 0 & 0 \\ 1 & \bar{1} & 0 \\ 0 & 0 & 1 \end{pmatrix} \begin{pmatrix} 0 \\ 0 \\ z \end{pmatrix} = \begin{pmatrix} 0 \\ 0 \\ z \end{pmatrix} \Rightarrow RE1 \rightarrow RE1 \ (RE2 \rightarrow RE2) \tag{C.7}$$

$$c_{yz}; \begin{pmatrix} \bar{1} & 0 & 0 \\ \bar{1} & 1 & 0 \\ 0 & 0 & 1+\frac{1}{2} \end{pmatrix} \begin{pmatrix} 0 \\ 0 \\ z \end{pmatrix} = \begin{pmatrix} 0 \\ 0 \\ z+\frac{1}{2} \end{pmatrix} \Rightarrow RE1 \rightarrow RE2 \ (RE2 \rightarrow RE1) \tag{C.8}$$

That is, E and m_{2xx} always transform the RE atom into the same site, whereas 2 and c_{yz} always transform RE1 into RE2 and vice versa. Therefore, by taking this knowledge into account, the transformation of each spin component can be calculated from the four symmetry elements:

$$E(x,y,z) \rightarrow (x,y,z) \tag{C.9}$$

$$2(x,y,z) \rightarrow (\bar{x},\bar{y},z+\frac{1}{2}) \tag{C.10}$$

$$c_{yz}(x,y,z) \rightarrow (\bar{x},\bar{x}+y,z+\frac{1}{2}) \tag{C.11}$$

$$m_{2xx}(x,y,z) \rightarrow (x,x-y,z) \tag{C.12}$$

bearing in mind the change of spin direction under certain symmetry operations (see e.g. [82] for a list of spin transformations under various symmetry operations). The final results as obtained from equations C.5 to C.12 are presented in table C.2 below for S_1, the magnetic moment of RE1.

Table C.2: Transformation properties of the individual spin components.

	E	2	m_{2xx}	c_{yz}
S_{1x}	$+S_{1x}$	$-S_{2x}$	$-S_{1x}$	$-S_{2x}$
S_{1y}	$+S_{1y}$	$-S_{2y}$	$-S_{1x}+S_{1y}$	$+S_{2x}-S_{2y}$
S_{1z}	$+S_{1z}$	$-S_{2z}$	$+S_{1z}$	$-S_{2z}$

The basis functions can now be calculated in a straight forward manner from the general equation

$$V_{ij}^{\nu} = \sum_{C_g} D_{ij}^{\nu}(C_g) \cdot C_g V \tag{C.13}$$

where the summations are over all the g symmetry operations of the group. The V_{ij}^{ν} are a linear combination of spin components, and the $D_{ij}^{\nu}(C_g)$ are matrix components of C_g.

This is calculated in turn for each spin component, $S_{i\alpha}$, where the final magnetic couplings as determined from the irreducible representations are

$$\Gamma_1 : -S_{1x} - S_{2x} + 2S_{1y} - 2S_{2y} + 2S_{1z} - 2S_{2z} \tag{C.14}$$

$$\Gamma_2 : +3S_{1x} + S_{2x} \tag{C.15}$$

$$\Gamma_3 : +S_{1x} - S_{2x} + 2S_{1y} + 2S_{2y} + 2S_{1z} + 2S_{2z} \tag{C.16}$$

$$\Gamma_4 : +3S_{1x} + S_{2x} \tag{C.17}$$

Γ_1 corresponds to an arrangement of magnetic ions that are coupled ferromagnetically along the a-axis, and antiferromagnetically along the b- and c-axes. Γ_2 and Γ_4 give identical solutions with the magnetic moments lying exclusively along the a-axis, with ferromagnetic coupling between the two atomic sites, and Γ_3 describes an antiferromagnetic arrangement along the a-axis, and ferromagnetic along b and c.

These are all the possible spin couplings which are allowed under the given crystal symmetry, space group $P6_3mc$, combined with the observed propagation vector, $\tau = [1/2, 0, 0]$.

Bibliography

[1] 'Conference on high performance permanent magnetic materials', *Mat. Res. Soc. Symp. Proc.*, **96** (1987) ed. S. G. Sankar, J. F. Herbst, N. C. Koon.

[2] M. A. Ruderman, C. Kittel, *Phys. Rev.*, **96** (1954) 99.
T. Kasuya, *Prog. Theor. Phys.*, **16** (1956) 45.
K. Yosida, *Phys. Rev.*, **106** (1957) 893.

[3] H. Bethe, *Annln. Phys.*, **3** (1929) 133.

[4] N. Grewe, F. Steglich, *Handbook on the Physics and Chemistry of Rare-Earths vol. 14 'Heavy Fermions'*, ed. K. A. Gschneider and L. Eyring (1991).

[5] A. Szytula and J. Leciejewicz, *Handbook of Crystal Structures and Magnetic Properties of Rare Earth Intermetallics*, CRC Press, Boca Raton, FL, 1994.

[6] F. Steglich, J. Aarts, C. D. Bredl, W. Lieke, D. Mesche, W. Franz, J. Schäfer, *Phys. Rev. Lett.*, **43** (1979) 1892.

[7] T. Takabatake and H. Fujii, *Jpn. Appl. Phys. Ser.*, **8** (1993) 254.

[8] P. Villars and L. D. Calvert, *Pearson's Handbook of Crystallographic Data for Intermetallic Phases.*, ASM International, Materials Park. OH. 2nd edn., 1991

[9] M. L. Fornasini and F. Merlo, *J. Alloys Compd.*, **219** (1995) 63.

[10] G. Zanicchi, D. Mazzone, V. Contardi, R. Marazza, G. Rambaldi, D. Rossi, *Gaz. Chim. Italiana*, **113** (1983) 257.

[11] D. Rossi, R. Marazza, R. Ferro, *J. Alloys Compd.*, **187** (1992) 267.

[12] V. K. Pecharsky, K. A. Gschneider, O. I. Bodak, A. S. Protsyk, *J. Less. Comm. Met.*, **168** (1991) 257.

[13] R. Pöttgen, H. Borrmann, C. Felser, O. Jepsen, R. Henn, R. K. Kremer, A. Simon, *J. Alloys Compd.*, **235** (1996) 170.

[14] R. Pöttgen, B. J. Gibson, R. K. Kremer, *Z. Kristallogr.* **58** (1997) 212.

[15] R. Pöttgen, *Z. Naturforsch.* **50b** (1995) 1071.

[16] W. Schnelle, R. Pöttgen, R. K. Kremer, E. Gmelin, O. Jepsen, *J. Phys. Conds. Mater.*, **9** (1997) 1435.

[17] R. Pöttgen, H. Borrmann, R. K. Kremer, *J. Mag. Magn. Mater.* **152** (1996) 196.

[18] H. L. Krauss, H. Stach, *Z. Anorg. Allg. Chem.*, **366** (1969) 34.

[19] J. Czochralski, *Z. Phys. Chemie*, **92** (1918) 219.

[20] M. Jankovicz, Kristallzüchtung und Charakterisierung von CeAuGe, Staatsexamensarbeit, Kristall Labor der Uni. Frankfurt (1998) unpublished.

[21] A. Simon, *J. Appl. Cryst.*, **3** (1970) 11.

[22] K. Yvon, W. Jeitschko, E. Partheé, *J. Appl. Crystallogr.*, **10** (1997) 73.

[23] B. J. Gibson, R. K. Kremer, W. Schnelle, R. Pöttgen, B. Ouladdiaf, K. R. A. Ziebeck, *to be published.*

[24] B. J. Gibson, R. Pöttgen, R. K. Kremer, A. Simon, K. R. A. Ziebeck, *J. Alloys Compds.*, **239** (1996) 34.

[25] R. Pöttgen, *J. Mater. Chem.*, **5** (1995) 505.

[26] F. Merlo, M. Pani, F. Canepa, M. L. Fornasini, *J. Alloys Compds.*, **264** (1998) 82.

[27] R. B. Goldfarb and J. V. Minervina, *Rev. Sci. Instrum.*, **55** (1984) 761.

[28] M. Couach, A. F. Khoder, F. Monnier, *Cryogenics*, **25** (1985) 695.

[29] Quantum Design, MPMS-Handbook (1986).

[30] M. Tinkham, *Introduction to Superconductivity*, McGraw-Hill Inc., New York (1996).

[31] W. Schnelle, *Specifische Wärme von Hoch-T_C-Supraleitern*, Diplomarbeit, Universität Köln (1989).

[32] W. Schnelle, *Specifische Wärme von Hoch-T_C-Supraleitern*, Dissertation, Universität Köln (1992).

[33] E. Gmelin, *Therm. Acta*, **29**, (1979) 1.

[34] E. Gmelin, *Them. Acta*, **110**, (1987) 183.

[35] H. W. de Wijn, A. M. van Diepen, K. H. Buschow, *Phys. Rev. B*, **161** (1967) 253.

[36] H. R. Kirchmayr, C. A. Poldy, *Magnetic Properties of Intermetallic Compounds of Rare-Earth Metals*, in K. A. Gschneider, Jr. and L. Eyrings (eds.), *Handbook on the Physics and Chemistry of Rare-Earths*, **2** (1979), North-Holland.

[37] G. F. Goya, R. C. Mercarder, M. T. Causa, M. Tovar, *J. Phys. Cond. Mater.* , **8** (1996) 8607.

[38] G. H. Dieke, *Spectra and Energy Levels of Rare-Earth Ions in Crystals*, Interscience publishers, 1968.

[39] P. Javorsky, *Magnetism in RCuAl and RNiAl Compounds*, Doctoral Thesis, Prague University (1997).

[40] O. K. Andersen, *Phys. Rev. B* **12** (1975) 3060.
O. K. Andersen and O. Jepsen, *Phys. Rev. Lett.* **53** (1984) 2571.

[41] O. K. Andersen, O. Jepsen, D. Glötzel, *Highlights of Condensed-Matter Theory*, ed. F. Bassini, F. Fumi, and M. P. Tosi, New York:North Holland (1985).

[42] U. von Barth, L. Hedin, *J. Phys. C:Solid State Phys.*, **4** (1971) 2064.

[43] G. Krier, O. Jepsen, O. K. Andersen, (1997) to be published.

[44] L. J. van der Pauw, *Philips Res. Rep.*, **13** (1958) 1.

[45] E. Gratz, M. J. Zuckermann, *Handbook of the Physics and Chemistry of Rare-Earth*, ed. K. A. Gschneidner and L. Eyring, Amsterdam:North Holland, 1982.

[46] C. Kittel, *Introduction to Solid State Physics, 4^{th} Ed.*, John Wiley & Sons, New York, 1971.

[47] E. S. R. Gopal, *Specific Heat at Low Temperatures*, London:Plenum 1966.

[48] P. W. Selwood, *Magnetochemistry*, Interscience Publishers, New York, (1956)

[49] N. W. Ashcrof and D. Mermin, *Solid State Physics*, New York:Holt, 1976.

[50] G. J. Nieuwenhuys, *Handbook of Magnetic Materials vol. 9*, ed. K. H. J. Buschow, North Holland (1995).

[51] S. K. Dhar, S. K. Malik, J. Vijayaraghaven, *J. Phys. C*, **14** (1981) L321.

[52] A. Böhm, R. Caspary, U. Habel, L. Pawlak, A. Zuber, F. Steglich, A. Loidl, *J. Magn. Magn. Mater.*, **150** (1988) 76.

[53] S. K. Dhar, S. M. Pattelwar, J. Vijayaraghaven, *Physica B*, **491** (1993) 186.

[54] D. T. Adroja, B. D. Rainford, S. K. Malik, *Physica B*, **566** (1993) 186.

[55] C. Domb, A. R. Miedema, *Progr. Low Temp. Phys.*, **4** (1964) 296.

[56] E. Ising, *Z. für Physik*, **31** (1925) 253.

[57] S.N.Kaul, *J. Magn. Magn. Mater.*, **53** (1985) 5.

[58] R. Reisser, M. Seeger, M.Fähnle, H. Kronmüller, *J. Mag. Magn. Mater.*, **110** (1992) 32.

[59] R. Reisser, Thesis, University of Stuttgart (1990).

[60] B. Widom, *J. Chem. Phys.*, **43** (1965) 3892.

[61] A. Arrott, J. E. Noakes, *Phys. Rev. Lett.*, **19** (1967) 786.

[62] M. Seeger, H. Kronmüller, *J. Magn. Magn. Mater.*, **78** (1989) 393.

[63] R. Reisser, M. Fähnle, H. Kronmüller, *J. Magn. Magn. Mater.*, **97** (1991) 83.

[64] J. S. Kouvel, M. E. Fisher, *Phys. Rev.*, **136A** (1964) 1626.

[65] M. Haug, M. Fähnle, H. Kronmüller, *J. Magn. Magn. Mater.*, **69** (1987) 163; *Phys. Stat. Sol. B*, **144** (1987) 411.

[66] M. Seeger, Thesis, University of Stuttgart (1991).

[67] E. Brück, M. van Sprang, J. C. P. Klasse, F. R. de Boer, *J. Appl. Phys.*, **63** (1988) 3417.

[68] K. Satoh, Y. Maeno, T. Fujita, Y. Uwatoka, H. Fujii, *J. Phys. Colloq.*, **49** (1988) 779.

[69] B. K. Cho, B. N. Harmon, D. C. Johnston, P. C. Canfield, *Phys. Rev. B*, **53** (1996) 2217.

[70] K. W. H. Stevens, *Proc. Phys. Soc. Lond.*, **A65** (1952) 209.

[71] Program *Simult* written and developed by R. K. Kremer, and used by kind permission.

[72] A. Abragram and B, Bleaney, *Electron Paramagnetic Resonance of Transition Ions*, Oxford University Press, 1970.

[73] Manufactured by F. Razavi, Brock University St. Catherines, Ontario, Canada.

[74] U. Schwarz, Habilitationsschrift, T. U. Darmstadt, Germany 1998.

[75] A. Eiling, J. S. Schilling, *J. Phys. F: Metal Phys.*, **11** (1981) 623.

[76] http://www.ill.fr/YellowBook/D20/ (1998).

[77] http://www.ill.fr/YellowBook/IN3/ (1998).

[78] http://www.ill.fr/YellowBook/D1B/ (1998).

[79] Rodrequez-Carvajal, *Fullprof: a program for Rietveld refinement and profile matching analysis of complex powder diffraction patterns.*, I.L.L, unpublished.

[80] H. M. Rietveld, *J. Appl. Crystallogr.* **2** (1969) 65.

[81] E. Bertaut, *Acta. Cryst.*, **A24** (1968) 217.

[82] E. Bertaut, *Magnetism III*, ed. G. T. Rado and H. Shull, Academic Press, (1963)

[83] G. Donnay, L. M. Corliss, J. D. H. Donnay, N. Elliot, J. M. Hastings, *Phys Rev.*, **112** (1958) 1917.

[84] G. L. Squires, *Introduction to the Theory of Neutron Scattering*, Cambridge University Press, 1978.

[85] D. Gignoux, D. Schmitt, *Phys. Rev. B* **48** (1993) 12682.

[86] S. Baran, M. Hofmann, J. Leciejewicz, B. Penc, M. Slaski, A. Szytula, *J. Alloys. Compd.*, **281** (1998) 92.

Acknowledgements

I am indebted to the following people for their help and support during the research and writing of this thesis

- *Dr. R. K. Kremer*, for his many valuable ideas and especially for his constant encouragement and enthusiasm.
- *Dr. R. Pöttgen*, for his help during the stressful first few months, and also for the many beneficial discussions on crystallography.
- *Prof. A. Simon* and *Prof. K. R. A. Ziebeck*, for giving me the possibility to prepare my thesis within the 'Simon' group at the Max-Planck-Institut fr Festkörperforschung and for their steady interest in my work.
- *Dr. W. Schnelle*, for performing the specific heat capacity measurements, and for his help in analysing the results.
- *Dr. B. Ouladdiaf*, for his help performing the neutron scattering experiments at the I.L.L, and for his many insights about magnetic structures.
- *Dr. E. Suard* and *Dr. M. Zolliker*, for their help performing the neutron diffraction experiments on D2B and IN3, respectively.
- *Dr. O. Jepsen*, for performing the band structure calculations.
- *E. Brücher*, *N. Rollbüller*, and *G. Siegle*, of the Chemie Service, for the many magnetisation and resistivity measurements.

- *W. Röttenbach*, for taking the Guinier diffraction patterns.

- *M. Jankovicz*, for preparing several large crystals of CeAuGe.

- Finally, I would like to thank my remaining colleagues at the Max-Planck-Institut for the stimulating, relaxed and friendly working atmosphere.